^{20}MG β DECAY AND THE ^{15}O$(\alpha, \gamma)^{19}$Ne$(p, \gamma)^{20}$Na REACTION SEQUENCE IN TYPE I X-RAY BURSTS

By

Brent Glassman

A DISSERTATION

Submitted to
Michigan State University
in partial fulfillment of the requirements
for the degree of

Physics - Doctor of Philosophy

2020

ProQuest Number: 27543326

ProQuest 27543326

ProQuest LLC
789 East Eisenhower Parkway
P.O. Box 1346
Ann Arbor, MI 48106 - 1346

ABSTRACT

^{20}MG β DECAY AND THE ^{15}O$(\alpha, \gamma)^{19}$Ne$(p, \gamma)^{20}$Na REACTION SEQUENCE IN TYPE I X-RAY BURSTS

By

Brent Glassman

Constraining the ^{15}O$(\alpha, \gamma)^{19}$Ne$(p, \gamma)^{20}$Na reaction rate is critically important for accurately simulating x-ray burst light curves, our only x-ray burst observable from Earth. Both the ^{15}O$(\alpha, \gamma)^{19}$Ne and ^{19}Ne$(p, \gamma)^{20}$Na reaction rates have been studied using a multitude of experimental techniques, yet only upper limits had been determined at the outset of the present work. The ^{15}O$(\alpha, \gamma)^{19}$Ne reaction in particular has been singled out as the most important reaction rate of all currently unknown rates to measure.

Utilizing the β decay of ^{20}Mg to populate ^{20}Na excited states, we further constrain the ^{19}Ne$(p, \gamma)^{20}$Na reaction rate by searching for γ decays from the most important resonance at E_x=2647 keV. Additionally, by populating ^{20}Na excited states high above the proton threshold, we populate the most important ^{19}Ne resonance for measuring the ^{15}O$(\alpha, \gamma)^{19}$Ne reaction rate at E_x=4.03 MeV. Herein, the results of this study are reported including: The full ^{20}Mg β-delayed γ ray spectrum and decay scheme; the upper limit on the β decay feeding of the ^{20}Na 2647 keV state; the Doppler broadening analysis of nine γ ray peaks from six excited states in ^{19}Ne; the intensity of ^{20}Mg$(\beta p \gamma)$ to the 4.03 MeV state in ^{19}Ne; the measurement of the ^{20}Na excitation energy at $7.44^{+0.25}_{-0.22}$ MeV feeding the 4.03 MeV state in ^{19}Ne; and the measurement of the center of mass proton energy for the feeding of the important 4.03 MeV state in ^{19}Ne at $1.23^{+0.25}_{-0.22}$ MeV.

This dissertation is dedicated to my mother Mary Kay and my father Howard for instilling in me my love for math and problem solving, and to Glenn LaFerriere for always providing me challenging problems to struggle over.

ACKNOWLEDGMENTS

This work would not be possible without the help and guidance of my advisor Chris Wrede. Chris's mentorship has been invaluable in all aspects of the scientific process even going beyond by assisting me through my biggest challenge in writing scientific papers and of course my dissertation. It has been a pleasure to work alongside Chris during the many large projects undertaken by his research group and the skills I am able to take from this experience are incalculable. Thank you for all of the work that you've put in and for all of the opportunities I've been afforded just by working alongside such a talented research group.

It takes a great deal of work to run a successful experiment with only the minimum amount of heart-attacks and all the credit has to go to the members of my research group. In particular, David Pérez-Loureiro provided a frankly offensive amount of help during the setup of the experiment and coding expertise for the data analysis, which I began to suspect amounted to billable hours rivaling a sizeable law-firm. Mike Bennett, Cathleen Fry, and Sarah Schwartz also contributed a tremendous effort during and after the experiment, and I'm thankful for their support throughout my graduate tenure. As postdocs joining the research group for brief periods of time, Moshe Friedman and Lijie Sun have been incredibly helpful with the most challenging aspects of my data analysis. Finally I'd like to thank all of the members of the collaboration who came to assist during the experiment and for their continued support during the writing process.

In addition to my advisor Chris, I also have to thank the members of my PhD committee; Heiko Hergert, Hironori Iwasaki, Jim Linnemann, and Artemis Spyrou. Their insights have provided me with useful avenues of analysis which had previously gone unconsidered and

expertise which was incredibly helpful during my analysis. A special thanks has to go to Hironori Iwasaki for filling a role on my committee when another member was unavailable.

It would be impossible to make it through graduate school without all of my friends to help me keep my sanity. A shout out to the first-year all-nighter crew who, after working through a weeks worth of problem sets in a night, definitely promised to never ever do that again. Twas always great to see your bright and shining faces that very next week. What else can be said about The Killers other than we definitely won that one softball game, and I can't really recall how the other ones went but probably really good. To my workout crew, we got absolutely diced. Congrats on the sick new bods! Thank you to everyone who made the tough times go by quicker, I could not have accomplished this without you. Note: In the event of future arbitration, let this document hereby certify that I Brent Glassman ~~Frank Reynolds~~ do not have *Donkey Brains*.

My sister Alyssa and mother Mary Kay can not be thanked enough for their support over the past six years. The many late night calls providing a calm voice to counter all of my doubts of success and their patience throughout graduate school has been incredibly meaningful to me.

TABLE OF CONTENTS

LIST OF TABLES

LIST OF FIGURES

xiii

xiv

KEY TO ABBREVIATIONS

- NSCL - National Superconducting Cyclotron Laboratory (East Lansing MI, USA)

- CoM - Center of Mass

- DDAS - Digital Data Acquisition System

- SeGA - Segmented Germanium Array

- PDF - Probability Density Function

- CDF - Cumulative Distribution Function

Chapter 1

Overview of Pertinent Nuclear Physics

1.1 Introduction to Nuclei

An important discovery about the makeup of the atom was made in 1911. The prevailing model of the atom at the time was that it consisted of positive and negative charge particles clumped together like a plum pudding [1]. Experiments to test this hypothesis were conducted by Ernest Rutherford and involved bombarding a thin gold foil with helium atoms (α-particles). If the pudding model were true, they expected all of the α particles to simply pass through the foil. However, over many trials the experimenters were surprised to find that some of these α particles were being deflected by the foil at angles as though they were balls bouncing off a wall [2]. This discovery meant that all of the positive charge and most of the mass must be contained at the center of the atom. The discovery of the neutron in 1932 [3] built a more complete picture of the atom where protons and neutrons were clumped together in the nucleus, bound by the strong force, and were surrounded by orbiting electrons.

A nucleus is conventionally identified by its element name and total number of protons and neutrons (A) in the nucleus, referred to as the *mass number*. The names of elements are determined by the number of protons (Z) in the nucleus, each of which is displayed on
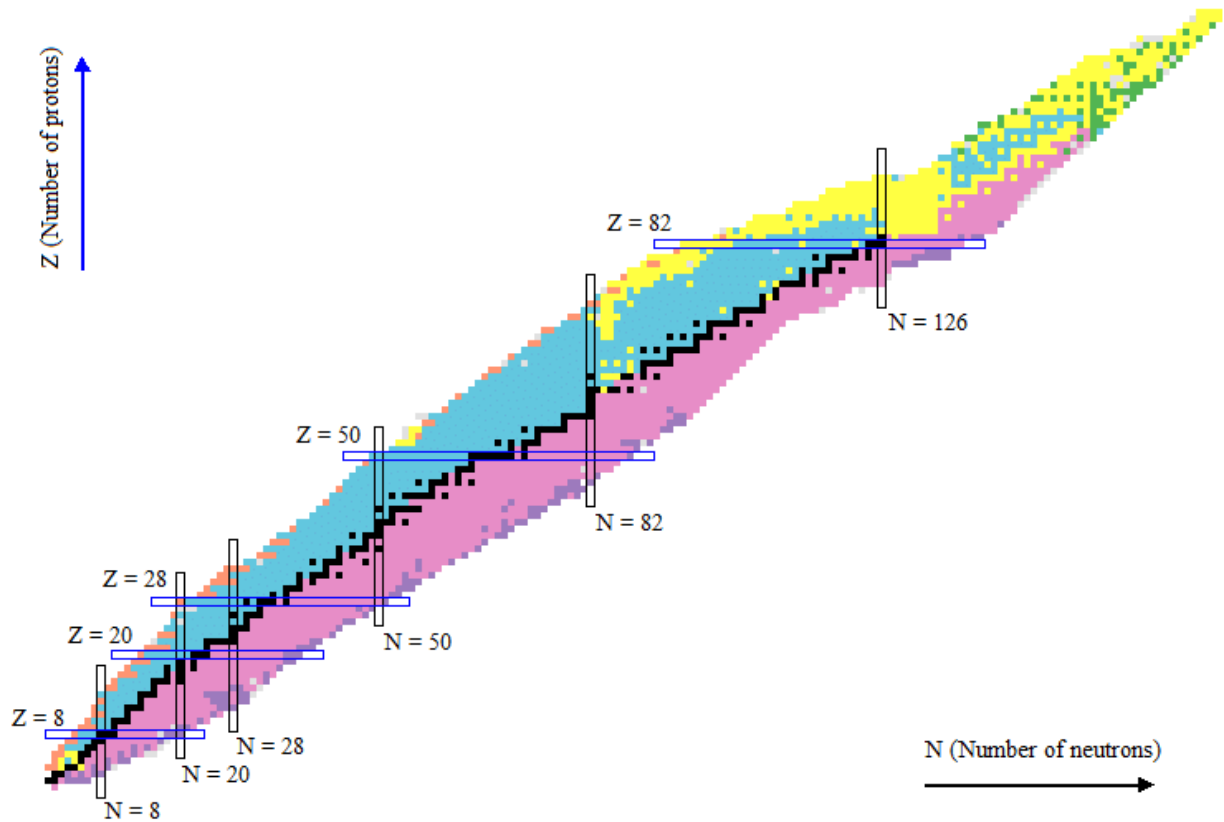
Figure 1.1: Chart of nuclides. The y-axis represents the number of protons Z in the nucleus and the x-axis represents the number of neutrons N. Boxes in black denote stable nuclei whereas colored boxes denote unstable nuclei. [4]

the periodic table of elements. For example, a nucleus of oxygen having 8 neutrons and 8 protons is denoted by ^{16}O.

Nuclei with the same number of protons and different numbers of neutrons (N) are referred to as isotopes. Similarly, nuclei with the same number of neutrons and different numbers of protons are referred to as isotones. All of the assorted nuclei that have been studied and many that have yet to be studied are displayed on the chart of nuclides in Figure 1.1.

The discovery of the nucleus led to many questions about the origin of the elements and produced the field of nuclear astrophysics in the 1950s through the work of Burbidge, Burbidge, Fowler, and Hoyle [5] which sought to tackle this question. As the field of nuclear

astrophysics has developed many questions have arisen such as: how do stars generate their energy, what is the life cycle of a star, where are the elements created in nucleosynthesis, and what are the corresponding stellar events that occur to synthesize these isotopes?

In order to tackle these questions it is important to understand the properties of both stable and unstable nuclei (nuclear structure) and how they interact with other nuclei (nuclear reactions).

1.2   Nuclear Shell Model

Like atoms whose electrons orbit the nucleus in a number of shells, similar to the planets orbiting the sun, nuclei can exist in a number of quantized energy states. Protons and neutrons separately fill the lowest energy shells to produce a nucleus in a configuration called the ground state. If proton(s) or neutron(s) occupy orbitals of higher energy than other available orbitals, these are referred to as nuclear excited states. The mass M_{exc} of a nucleus can be found by summing the mass of the nucleus in its ground state, $M_{g.s.}$ with the excitation energy E_{exc} (Eq. 1.1), where BE is the binding energy of a nucleus with N neutrons and Z protons and c represents the speed of light.

$$M_{exc} = M_{g.s.} + E_{exc}/c^2 \tag{1.1}$$

$$M_{g.s.} = Zm_p + Nm_n - BE(Z,N)/c^2 \tag{1.2}$$

In the atomic shell model each shell is filled with a specific number of electrons, in accordance with the Pauli Exclusion principle. The filled shells are considered to be inert and

the valence electrons determine the atomic properties in nuclei [6]. Both protons and neutrons independently fill orbitals with so-called *magic numbers* that correspond to quantum properties such as total angular momentum j, orbital angular momentum l, and number of nodes n in the wave function (Fig. 1.3), which can be well-described using a harmonic oscillator potential or Woods-Saxon potential (Fig. 1.2). Because protons and neutrons are fermions (spin 1/2 particles) these particles must abide by the Pauli Exclusion Principle, meaning that no 2 protons or neutrons in a nucleus can have the same quantum numbers. This property effectively restricts the size of each shell since each nucleon requires a different set quantum numbers.

The first shell, called the 1s-orbital is defined to have $l = 0$ angular momentum and protons are spin $s = 1/2$ particles which have total angular momentum $j = 1/2$. In general, there are 2j+1 projections of the total angular momentum or $j_z = \pm 1/2$ for the 1s-orbital and this defines the number of protons or neutrons allowed in the shell. The 1s-orbital can contain 2 such nucleons and this defines the first so-called magic number. Magic numbers denote the amount of nucleons to completely fill a nuclear shell. The p-shell is defined by $l = 1$ orbital angular momentum and can contain up to 6 protons or neutrons.

The magic numbers, derived from these quantum numbers, define shells which can hold 2, 8, 20, 28, 50, 82, 126 nucleons (Fig. 1.3). Since the the nuclear shells are determined from quantum numbers nlj, the shell model is often used to determine the spin-parity (J^{π}) of a nucleus in its ground state, where J describes the total coupled angular momentum and π describes the parity defined to be $(-1)^l$. For example, ^{20}Mg has 12 protons and 8 neutrons. The first 8 protons and neutrons fill up the *p-shell* and can be thought of as an inert ^{16}O core with $j = 0$ angular momentum and the remaining 4 protons form two spin-up and spin-down pairs which sit in the first $d_{5/2}$-*shell* and each of these pairs couple together

4
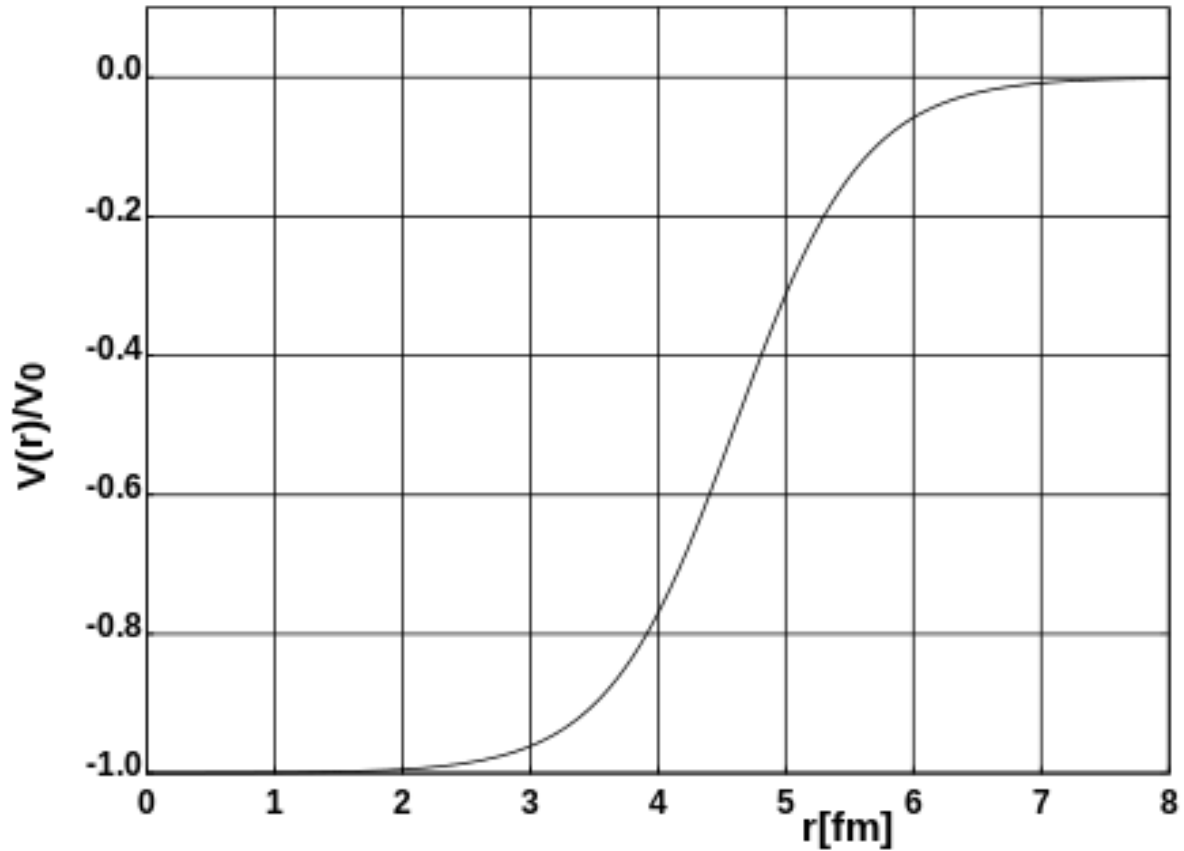
Figure 1.2: A Woods Saxon Potential, $V(r) = \frac{-V_o}{1+exp(\frac{r-R}{a})}$, is often used as input into the nuclear wave function and describes the forces on each nucleon, where $V_o \approx 50$ MeV describes the depth of the potential, $a \approx 0.5$ fm describes the so-called *surface thickness* of the nucleus, and $R \approx 1.25A^{1/3}$ fm approximates the radius of the nucleus.
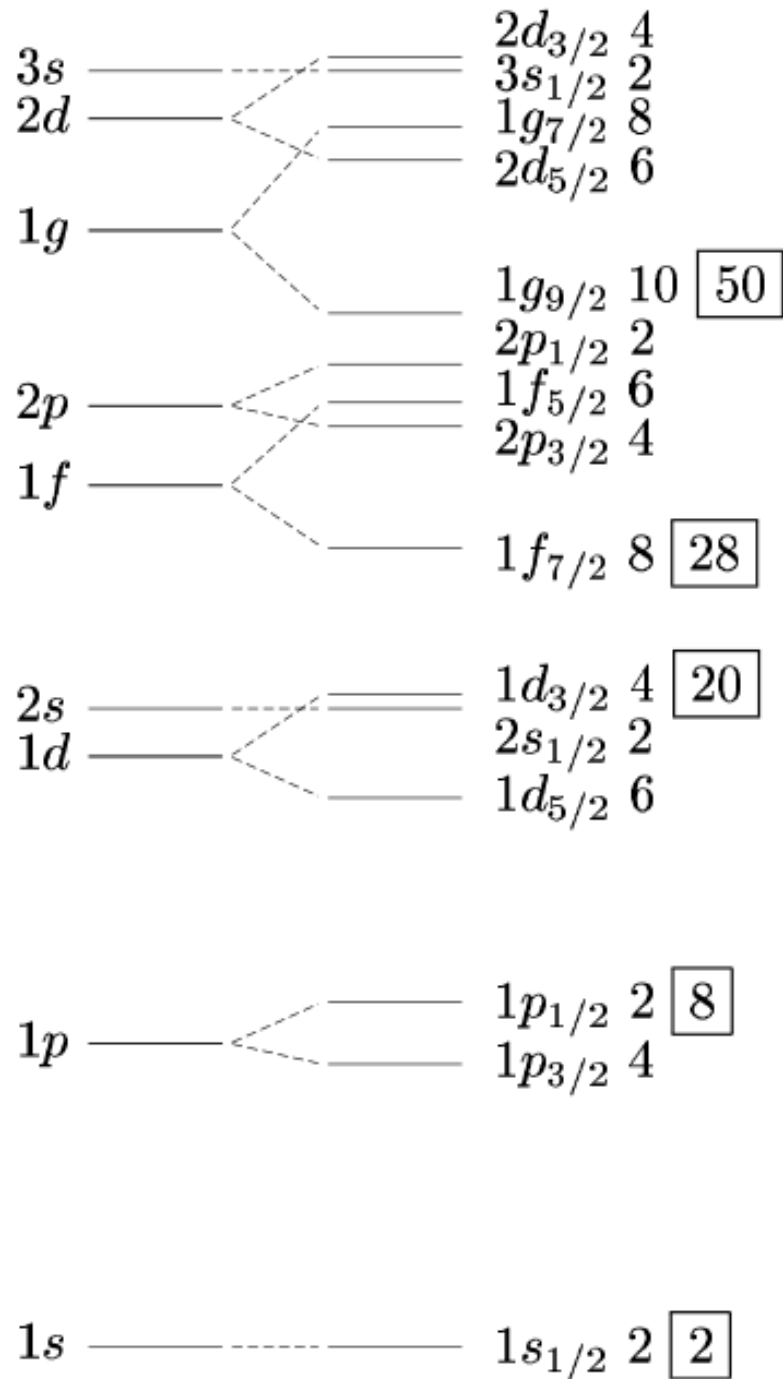
Figure 1.3: The energy levels on the left define shells via the principal quantum number $N = n + 1$, given by a nuclear wave function derived from a harmonic oscillator potential. The addition of a spin-orbit term to the nuclear potential yields the splitting of these levels and approximates shell closures which give rise to the magic numbers. Figure Credit: Bakken (GPL)

to give a total of $J = 0$ angular momentum. Since the protons in the unfilled shell sit in the sd-shell, the parity will be positive giving the ground state of ^{20}Mg a $J^\pi = 0^+$.

While this model does not provide accurate predictions in every case, it does have relatively good predictive power. Evidence for nuclear shells can be seen in nuclei with magic numbers of N or Z or both tend to be more stable than similar other isotopes or isotones.

In principle, the shell model can be used to predict many important nuclear properties, such as excited state energies, spin-parity assignments and, probabilities of transitioning to lower energy states. However, unlike the atomic shell model, the nuclear shell model's states are not ordered simply by the quantum number n since spin-orbit interactions and orbital angular momentum cause the splitting of states. This makes calculating the different many-body as opposed to single-particle excited states difficult since taking into account all possible interactions between nucleons scales factorially with the number of nucleons! Different effective interactions such as USD, USDA, and USDB [7] can be used in shell models to simplify the problem by reducing the interactions between nucleons to just the valence nucleons in the *sd-shell* and an inert core. More about these models will be discussed in subsequent chapters where the results from these models are compared to experimentally obtained values.

1.3 Nuclear Decay

It can be seen from the chart of nuclides (Fig. 1.1) that most nuclei are not stable. These unstable nuclei will undergo some form of decay until the nucleus becomes stable. In general, the further a nucleus is from the stable nuclei on the chart of nuclides, the more unstable it becomes, but what does it mean to be more unstable?

It is impossible to predict when an unstable nucleus will decay, however, a large sample of the same nucleus will follow the exponential law of radioactive decay (Eq. 1.3):

$$N(t) = N_0 e^{-\lambda t} \tag{1.3}$$

where N is the number of nuclei in the sample left after time t and $\tau = 1/\lambda$ represents the statistical lifetime (the average time for a nucleus to decay) of the nucleus [6]. The decay-constant (λ) for very unstable or *rare* nuclei will be large compared with nuclei that are close to stability.

There are a few different ways a nucleus can decay in order to become more stable. Light nuclei decay primarily via β-decay (pronounced *beta-decay*), γ-decay (pronounced *gamma-decay*), and particle emission (p, n, α). Heavier nuclei also decay by these same modes, but additionally have the possibility to spontaneously fission, where the nucleus breaks apart into two roughly similar sized lighter nuclei (Fig. 2.2). This mainly happens in much heavier nuclei with mass $A > 232$ because the binding energy per nucleon of heavy nuclei tends to be smaller than their lighter products, and this process can release energy whereas this process would require an energy input for light nuclei.

In principle a nucleus can decay to more than one different state (each transition is referred to as a decay branch) and the total lifetime of the parent nucleus will be:

$$\tau_{\text{total}} = \frac{1}{\sum_i \lambda_i} \tag{1.4}$$

However, it is often more important to know the individual λ_i as these can be used to represent the branching ratios.

1.3.1 β-Decay

β-decay occurs via the weak interaction and is responsible for converting protons to neutrons or neutrons to protons inside the nucleus, moving the nucleus closer to the valley of stability [8]. This process conserves mass number A, as well as total charge, and lepton number.

One type of β-decay involves nuclei *below* the stable nuclei on the chart of nuclides which are considered neutron-rich. This form of decay is called β^--decay (pronounced *beta-minus*) and involves converting a neutron to a proton and emitting an electron e^- and electron anti-neutrino from the nucleus (Eq. 1.5), where $^A X$ is referred to as the parent nucleus and $^A Y$ is referred to as the daughter nucleus. The state of the final nucleus in β-decay will be more tightly bound than the initial state or in other words have slightly less overall mass. This small difference in mass is converted into kinetic energy which is carried off mainly by the β particle and neutrino and is referred to as the Q-value.

$$ {}^A_Z X \longrightarrow {}^A_{Z+1} Y + e^- + \overline{\nu_e} $$
$$ Q_{\beta^-} = [m({}^A_Z X) - m({}^A_{Z+1} Y)]c^2 $$
(1.5)

Another form of decay, β^+-decay (pronounced *beta-plus* or *positron*), occurs for proton-rich nuclei above the stable nuclei on the chart of nuclides, and involves the conversion of a proton in the nucleus to a neutron and the emission of a positron e^+ and an electron neutrino (Eq. 1.6). The atom will emit an electron e^- in addition to the positron to conserve charge, and therefore β^+ decay can only proceed if the Q-value is greater than 1.022 MeV, the mass of two electrons.

$$ {}^A_Z X \longrightarrow {}^A_{Z-1} Y + e^+ + \nu_e $$
$$ Q_{\beta^+} = [m({}^A_Z X) - m({}^A_{Z-1} Y) - 2m_e]c^2 $$
(1.6)

A third type of decay, called electron capture, also occurs for the proton-rich nuclei. Instead of creating an electron or positron like in the first two processes, electron capture absorbs an electron from one of the atom's inner electronic shells in order to convert a proton in the nucleus into a neutron while conserving charge (Eq. 1.7).

$$\begin{gathered} {}^{A}_{Z}X + e^{-} \longrightarrow {}^{A}_{Z-1}Y + \nu_{e} \\ Q_{EC} = [m({}^{A}_{Z}X) - m({}^{A}_{Z-1}Y)]c^{2} - BE(e^{-}) \end{gathered}$$

(1.7)

Because β-decay proceeds via the weak interaction, there are rules that dictate the transitions which are allowed to occur to states in the daughter nucleus. These rules are discussed in more detail in section 1.3.1.2.

1.3.1.1 Introduction to Isospin

The theory of isospin was developed following the discovery of the neutron [9]. Isospin was able to describe the approximate symmetry between proton and neutron, in that they felt approximately the same force with regard to the strong interaction and they had very nearly the same mass. By this symmetry the proton could be thought of as the same particle as a neutron but in a different state (isospin-up and isospin-down).

Nucleons are fermions which have intrinsic spin $\frac{1}{2}$ and isospin $t = \frac{1}{2}$, a vector that obeys the same rules as angular momentum. Therefore, the number of isospin projections for a given isospin is defined by $-T < T_z < T$, yielding $2T + 1$ projections. By convention the isospin projection of a proton is $T_z = -\frac{1}{2}$ and the neutron has an isospin projection of

$T_z = +\frac{1}{2}$, and the total isospin projection of a ground state nucleus is:

$$T_z = \frac{1}{2}(N - Z) \tag{1.8}$$

A ^{20}Mg nucleus with 12 protons and 8 neutrons will have an isospin projection for the ground state of $T_z = -2$. If the degeneracy of the proton and neutron was not broken by the electromagnetic force, we would expect the ground states and excited states to approximate the level scheme in Figure 1.4. However because the degeneracy is broken by the electromagnetic force, a more realistic picture of the level scheme will cause a splitting of these states (Fig. 1.5).

This has consequences for β-decay since the vector (V) and axial vector (A) components of the weak interaction operate on the isospin projection by raising or lowering it. Certain selection rules will therefore govern which states in the daughter nucleus are *allowed* to be populated in β-decay.

1.3.1.2 β decay selection rules

Both the Vector and Axial Vector components of the weak interaction contribute to the β-decay rate R given by Equation 1.9 where K_o is a constant, f depends on the β-decay Q-value, g_V and g_A are the vector and axial vector coupling constants, and $B(F)$ and $B(GT)$ are the Fermi and Gamow-Teller transition strengths.

$$R_{i,f} = \frac{f}{K_o}[g_V^2 B_{i,f}(F\pm) + g_A^2 B_{i,f}(GT\pm)] \tag{1.9}$$

The Fermi and Gamow-Teller transitions describe different ways in which β-decay can proceed. For so-called *allowed transitions* the emitted β-decay particles carry $L = 0$ angu-

11
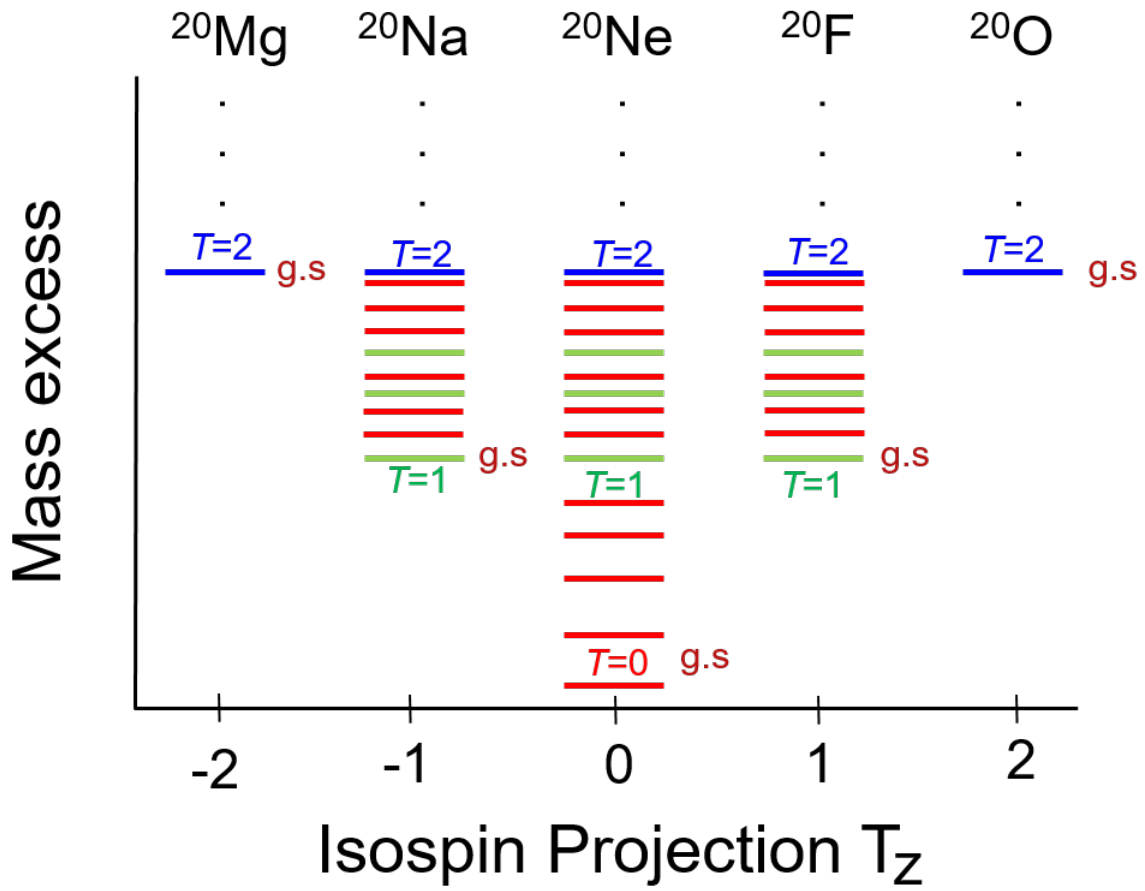
Figure 1.4: An approximate level scheme for the different Isospin projections in the $A = 20$, $T = 2$ multiplet, where neutrons and protons are degenerate.
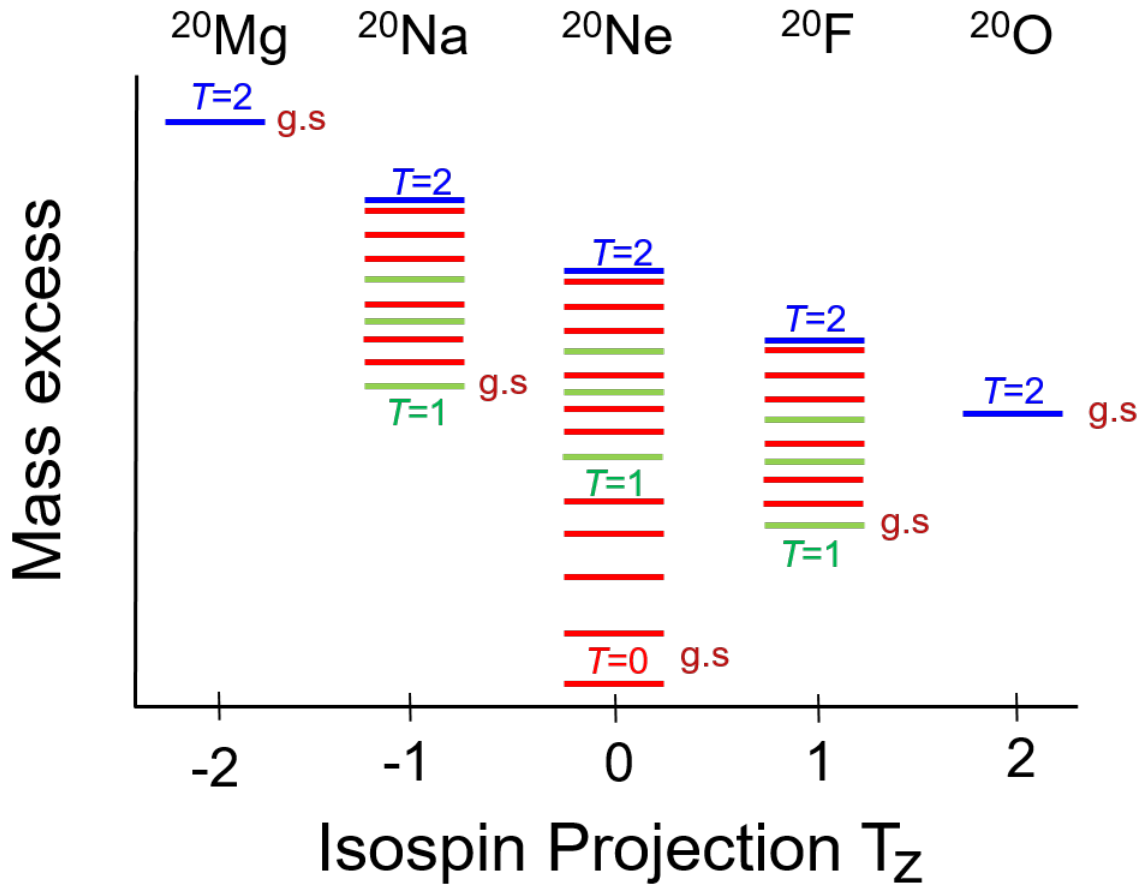
Figure 1.5: An approximate level scheme for the different Isospin projections in the $A = 20$, $T = 2$ multiplet where the degeneracy of the proton and neutron is broken by the electromagnetic force.

lar momentum. β-decays where $L > 0$ is carried by the emitted particles are considered *forbidden* and are not truly impossible but proceed at a much slower rate than allowed decays.

The operator for a Fermi transition is given by $O_F = \sum_a \hat{\tau}_{a\pm}$ and this operates over all nucleons (a) in the nucleus and $\hat{\tau}_{a\pm}$ serves as the raising/lowering operator for the isospin projection T_z. For allowed Fermi transitions the spins of the emitted leptons couple together for a total spin of $S = 0$, and it follows that the initial and final angular momentum of the nucleus will not change since no angular momentum is carried off, $\Delta J = 0$ and also isospin $\Delta T = 0$.

The operator for a Gamow-Teller transition is given by $O_{GT} = \sum_a \vec{\sigma}_a \hat{\tau}_{a\pm}$ and also operates over all nucleons (a), where $\vec{\sigma}_a$ is the vector the Pauli-spin matrix which operates on angular momentum J such that $\Delta J = 0, 1$. Allowed Gamow-Teller transitions occur for β-decays where the spin of the emitted particles couple together such that $S = 1$. In this form of decay the isospin projection is raised/lowered by 1, $\Delta T_z = \pm 1$, like in Fermi decay but also has the properties $\vec{T}_f = \vec{T}_i + \vec{1}$ and $\vec{J}_f = \vec{J}_i + \vec{1}$, since is a vector operator. From the addition of angular momentum this produces the rules for allowed Gamow-Teller decay, $\Delta J = 0, 1$ and $\Delta T = 0, 1$ (Table 1.1).

Table 1.1: Selection rules governing β-decay. Columns 1-5 refer to the type of transition, orbital angular momentum carried off by β-decay particles, change in isospin between initial and final states of the nucleus, the change in total angular momentum between initial and final state of the nucleus, and the change in parity respectively.

Transition Type	L	ΔT	ΔJ	$\Delta \pi$
Fermi	0	0	0	no
Gamow-Teller	0	0,1	0,1	no
First-forbidden	1	0,1,2	0,1,2	yes
Second-forbidden	2	2,3	1,2,3	no
Third-forbidden	3	3,4	2,3,4	yes

The consequences of the selection rules become clear for most β-decay processes. The constraints on the Fermi transition only allow for decay to a single isobaric analog state, and the decay rate will tend to be much higher for this specific transition. This type of transition is also referred to as *super-allowed* because of its high transition rate. The constraints on Gamow-Teller decay are not as stringent as for Fermi decay and Gamow-Teller decays will be split between many *allowed* transitions.

First forbidden transitions are not considered impossible, but rather far less likely than the allowed type of decays previously discussed. This is because it is very unlikely for the β particle and neutrino to be emitted in states with $l > 0$. Typically, first-forbidden decays are four orders of magnitude (10^{-4}) less likely than allowed β-decay and each higher order of forbiddenness is suppressed by another four orders of magnitude due to conservation of angular momentum.

Because the rate of decay occurs at vastly different rates for allowed and forbidden transitions, the selection rules can be applied to determine the J^π of states experimentally by measuring the partial decay rate R. Reorganizing equation 1.9 and taking the decay rate $R \sim \frac{1}{t_{1/2}}$, where $t_{1/2}$ is the partial half-life, we get:

$$ft_{1/2} = \frac{K_o}{[g_V^2 B_{i,f}(F_\pm) + g_A^2 B_{i,f}(GT_\pm)]} \tag{1.10}$$

The value $\log_{10} ft_{1/2}$ is used to compare transitions of different energy to each other. Super-allowed fermi transitions tend to have $\log_{10} ft_{1/2}$ values between 3-4, allowed transitions 4-6, first-forbidden transitions 6-10, and second forbidden transitions 10-13.

1.3.2 γ decay

Following β-decay or particle emission, such as particle emission of protons, neutrons, or α particles, the resulting nucleus is often left in a nuclear excited state and can de-excite to other excited states or the ground state by emission of γ-rays. Gamma-rays are photons emitted by the nucleus at energies typically 100 keV to 10 MeV.

During the γ decay process, the energy ΔE is released in the form of a γ-ray carrying energy E_γ, as well as a small amount of recoil energy KE_{rec} imparted on the nucleus of mass M_f. This is because photons carry momentum $p_\gamma = E_\gamma/c$ and the total momentum of the system must be conserved (Eq. 1.11):

$$\vec{p}_\gamma = -\vec{p}_{rec}$$

$$\Delta E = E_i - E_f = E_\gamma + KE_{\mathrm{rec}} \tag{1.11}$$

$$\Delta E = E_\gamma + \frac{E_\gamma^2}{2M_f c^2}$$

Measuring γ-ray energies in the lab is an extremely useful tool for scientists to build a picture of the excited state energies of a nucleus because of the ability to measure their energies with very high precision.

Like β-decay, γ decay also has its own set of selection rules for angular momentum and parity. γ-ray transitions emit via electric or magnetic type radiation, and this is determined by the multipole order given by the quantum number l of the photon. The type of transition is electric when the change in parity between initial and final nuclear states follows $\pi_f = \pi_i(-1)^l$ and magnetic when $\pi_f = \pi_i(-1)^{l+1}$. The angular momentum of the initial and final states is given by $\vec{J}_f = \vec{J}_i + \vec{l}$ and since the intrinsic spin of a photon is 1, there are no transitions of type $0 \to 0$. From the parity selection rules above and the conservation of

angular momentum the parity selection rules can be written as 5.7, where $\Delta\pi$ is the change in parity between initial and final state:

$$|J_i - J_f| \leq l \leq J_i + J_f$$

$$\Delta\pi = \text{no: even electric, odd magnetic} \tag{1.12}$$

$$\Delta\pi = \text{yes: odd electric, even magnetic}$$

Approximations for the electric multipole transition probabilities can be calculated from equation 1.13 and magnetic multipole transition probabilities can be calculated from equation 1.14.

$$\lambda(EL) \approx \frac{8\pi(L+1)}{L[(2L+1)!!]^2}\frac{e^2}{4\pi\epsilon_o\hbar c}\left(\frac{E}{\hbar c}\right)^{2L+1}\left(\frac{3}{L+3}\right)^2 cR^{2L} \tag{1.13}$$

$$\lambda(ML) \approx \frac{8\pi(L+1)}{L[(2L+1)!!]^2}\left(\mu_p - \frac{1}{L+1}\right)^2\left(\frac{\hbar}{m_p c}\right)^2\frac{e^2}{4\pi\epsilon_o\hbar c}\left(\frac{E}{\hbar c}\right)^{2L+1}\left(\frac{3}{L+2}\right)^2 cR^{2L-2} \tag{1.14}$$

These equations are known as the Weisskopf estimates [6] and help to determine which type of radiation should be more likely in a transition. From an examination of these estimates, the γ-ray transition rates are dominated by the lower order multipole transitions E1 (electric dipole), M1 (magnetic dipole), and E2 (electric quadrupole).

1.3.3   Nucleon Emission

Similar to β-decay, the Q-value for nucleon emission must be positive for this type of decay to occur 1.15.

$$S_n = -Q_n = BE(N, Z) - BE(N - 1, Z)$$
$$S_p = -Q_p = BE(N, Z) - BE(N, Z - 1)$$

(1.15)

These are referred to as the neutron separation energy S_n and proton separation energy S_p. Moving away from the valley of stable nuclei on the chart of nuclides we end up at what is called the drip-line, where nuclei are very proton-rich or neutron-rich, and the boundaries of S_p and S_n go from positive to negative values. Any nucleon we try to add is not bound to the nucleus and simply *drips* off.

It is possible for nucleon emission to occur where the values of S_p and S_n are positive. If the nucleus is in an excited state where $E_{exc.} > S_n$ or $E_{exc.} > S_p$, then this opens up the possibility for nucleon emission which can occur following β-decay where the resulting nucleus is left in an excited state. This process is referred to as β-delayed nucleon emission. It is also possible for an α particle or other particles such as a deuteron (^{2}H) to be emitted if the particle separation energies are low enough.

The nucleus ^{20}Mg can β decay to excited states of ^{20}Na above the proton separation energy. In this work, we observed the process of ^{20}Mg β-delayed proton emission (denoted as ^{20}Mg$(\beta p)^{19}$Ne) to a number of excited states in ^{19}Ne via the γ-ray emission. Some of the ^{19}Ne excited states populated by β-delayed proton decay are expected to be above the α-particle separation energy and can emit an α particle following this decay chain. This decay sequence is of great interest to many nuclear astrophysicists studying Type I x-ray

bursts, which will be discussed in more detail in section 2.1.2.

We have seen that nuclei transition in many ways to become more stable and will continue to do so if unimpeded (Fig. 1.1). However, the situation becomes more complex in stars where nuclei regularly interact with one another in very hot environments. For highly energetic stellar events, the possibility of particle capture to produce more massive nuclei and the excitation of nuclei via nuclear reactions also occurs and this will be addressed in the next chapter.

Chapter 2

Motivations for studying the $^{15}\mathrm{O}(\alpha,\gamma)^{19}\mathrm{Ne}(p,\gamma)^{20}\mathrm{Na}$ Reaction Sequence

2.1 Nuclear Astrophysics

A host of observations and experiments conducted in the 1950s helped to definitively prove that nucleosynthesis occurs in stars. In 1952 an important discovery of technetium spectral lines from red giant stars helped solidify this notion [10]. Since there are no stable isotopes of technetium and the longest lived isotope is much shorter than the life of the universe, the element must have been created in the star itself!

These observations helped to solidify one of the fundamental principles of nuclear astrophysics that the Big Bang created the elements Hydrogen, Helium, and Lithium, and the rest of the elements are created in stars as well as a small amount via cosmic ray spallation [11].

Observations of the luminosity, or the amount of energy radiated over time, from thousands of stars has helped us to categorize the many different types of stars that exist and build a model of the life cycles that stars follow from birth to death. The luminosity can vary

widely from star to star. When the color (which is determined by the surface temperature) of a star is plotted against the luminosity a clear grouping emerges of the different categories of stars that exist (Fig. 2.1).

The question of where elements are created and how they are distributed throughout the universe is still open. An initial assumption was that our own solar system isotopic abundance would be similar to abundances in other stars in the universe. However, within our own solar system we see elemental abundances that differ quite substantially from other places in the universe. Our understanding of elemental abundance must therefore proceed by modeling stellar evolution and the extreme stellar events which synthesize and expel these elements. Additionally, modeling these extreme stellar events can also complement observational information about the properties of certain stars such as mass, radius, and elemental composition.

2.1.1 Nuclear Reactions in stars

To understand *nuclear reactions*, it is first important to understand what is meant by the term. In order for a nuclear reaction to occur, one or more of the nuclei involved in the initial collision must be converted into a different nucleus. A typical nuclear reaction with target nucleus X, projectile nucleus a, and reaction products b and Y is written like Equation 2.1, or $X(a,b)Y$ for shorthand. In the shorthand equation everything to the left of the comma defines the reactants and everything to the right are reaction products.

$$a + X \longrightarrow Y + b \tag{2.1}$$
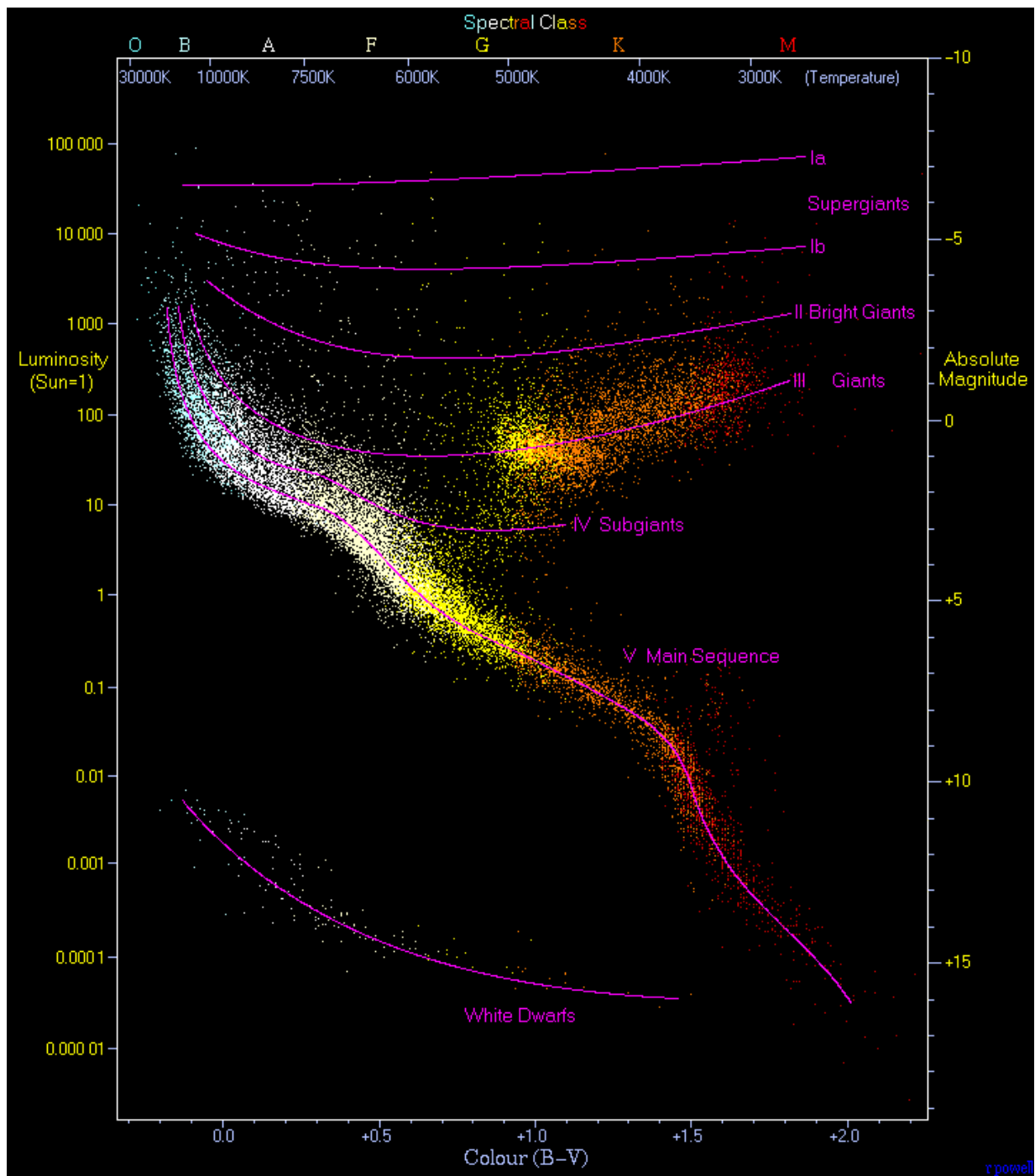
Figure 2.1: The Herzprung-Russel Diagram relates the luminosity and temperature of a star and classifies the star based on its position on the diagram. The largest portion of stars lays within the main sequence category as well as a few within various giant subgroups and white dwarfs which are remnants of main sequence stars. Only stars which have an observable luminosity are shown on the diagram and therefore stars like neutron stars do not appear in this figure. [figure credit - https://commons.wikimedia.org/wiki/File:HRDiagram.png]
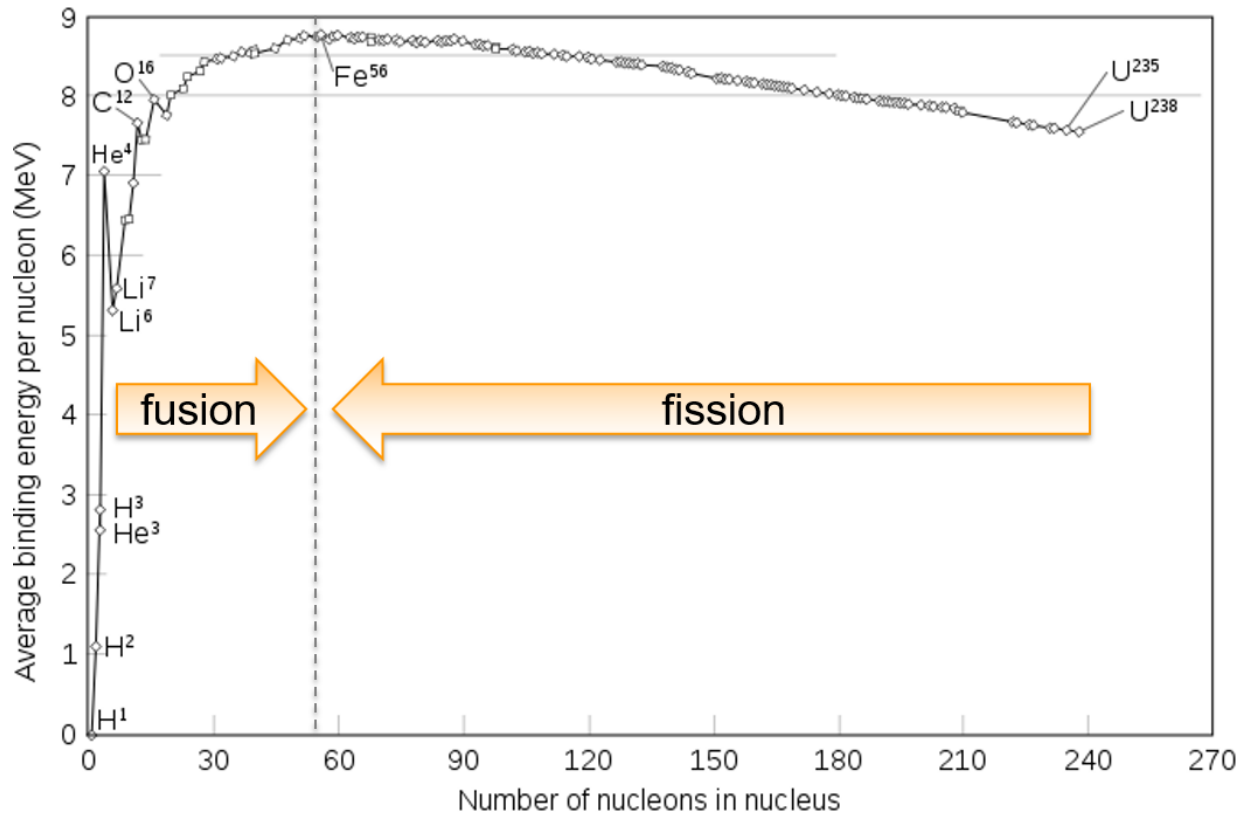
Figure 2.2: The graph displays the binding energy per nucleon for various mass number A nuclei. The product of nuclear fusions up to iron releases energy, and the fission of heavy elements whose fragments are more tightly bound are also exothermic. These processes give off energy by converting mass into energy since nuclei with higher binding energy have less mass per nucleon.

Some examples of nuclear reactions include fusion $X(a, \gamma)Y$, breakup $X(a, bc)Y$, and transfer reactions $X(a, b)Y$. If none of the nuclei are transformed in the collision, this is called nuclear scattering.

During the stellar burning phase of stars, fusion reactions fuel the output of energy by converting mass into thermal energy. Because the binding energy per nucleon for nuclei increases with mass all the way up to the iron mass region, nuclei can fuse and convert a small amount of their mass into kinetic energy in these nuclear reactions (Figure 2.2).

Stellar masses are described in solar mass terms relative to the sun, where the sun is described as having $1M_\odot$. The mass of a star strongly influences its lifespan and the evolution

23

of its composition. Stars tend to be grouped into four categories and include red dwarfs $0.08 M_\odot \leq M \leq 0.4 M_\odot$, low mass $0.4 M_\odot \leq M \leq 2 M_\odot$, intermediate mass $2 M_\odot \leq M \leq 11 M_\odot$, and massive $11 M_\odot \leq M$ [11] (Fig. 2.1). Stars with higher masses burn their nuclear fuel more quickly due to the intense gravitational pressure causing high temperatures which facilitate faster reaction rates.

The end stages of stars also depend strongly on their initial mass. Red dwarf to intermediate mass stars will collapse into white dwarfs with their composition depending on their initial mass (Helium, Carbon/Oxygen, Oxygen/Neon). However, cores of most massive stars will collapse into either neutron stars or black holes.

Following the collapse of a massive star, the resulting neutron stars which form have a mass of $\approx 1.5 M_\odot$, a radius of 10-15 km, and have a density of $\approx 10^{14}$ g/cm^3. The star is composed almost entirely of neutrons and is kept from collapsing by its neutron degeneracy pressure as well as the repulsive strong nuclear force. Once they are formed they no longer generate their own heat through fusion. However, they play an important role in binary systems which can generate outbursts called Type-I x-ray bursts under the right conditions.

Stellar events which synthesize elements in thermonuclear runaway reactions include classical novae and x-ray bursts which can synthesize isotopes up to mass $A \approx 40$ [12] and $A \approx 100$ [13] respectively as well as Type Ia SNe supernovae and neutron star mergers which are likely responsible for the creation of heavy elements beyond $A = 100$. These events are characterized by the rapid capture of neutrons followed by β^--decays and require an understanding of a host of different reaction rates and decay rates which contribute to the outbursts in order to accurately model these events.

The ^{15}O$(\alpha, \gamma)^{19}$Ne$(p, \gamma)^{20}$Na reaction sequence, studied in this work, is important for the understanding of Type-I X-ray burst energy generation, and the understanding of this

reaction rate has a large impact on the accuracy of x-ray burst models.

2.1.2   X-ray Bursts

Many stars are not like our own star in that $\approx$half of all stars tend to have a companion star and reside in a gravitationally bound binary system. A Type I x-ray burst can occur when a binary star system, consisting of a neutron star having mass $\approx 1.4 M_{\odot}$ and hydrogen-rich star with mass $\leq 1.5 M_{\odot}$, orbit close enough that matter from the hydrogen-rich star is accreted onto the surface of the neutron star [14].

The two stars in the binary system are surrounded by an imaginary surface called the Roche lobe which marks the point where each star's gravity is dominant. The point where the Roche lobe of each star meets is called the inner Lagrangian point and at this point the effects of gravity and rotations cancel. A star which evolves into a red giant star may expand beyond its Roche lobe allowing material to freely flow to its companion.

The surface of the neutron star is hot enough to fuse the hydrogen-rich fuel that falls onto its surface, donated by its companion star, into helium. The surface eventually becomes hot enough to fuse 3 helium atoms by resonant capture (see Fig. 2.7) into ^{12}C, known as the triple -α process (discussed in section 2.1.3.1). This first phase of Type-I x-ray bursts is know as the helium flash and ignites the surface of the neutron star in thermonuclear runaway. The final phase of this outburst is a likely site of the rapid proton capture process [15].

Following the triple-α reaction, the burning phase enters the hot CNO cycles or HCNO, followed by the $\alpha - p$ process and finally the rapid proton capture or rp-process where temperatures in this explosive environment can rise above 10^9 kelvin.

Type I X-ray bursts can be observed in the galaxy using space-based telescopes. The
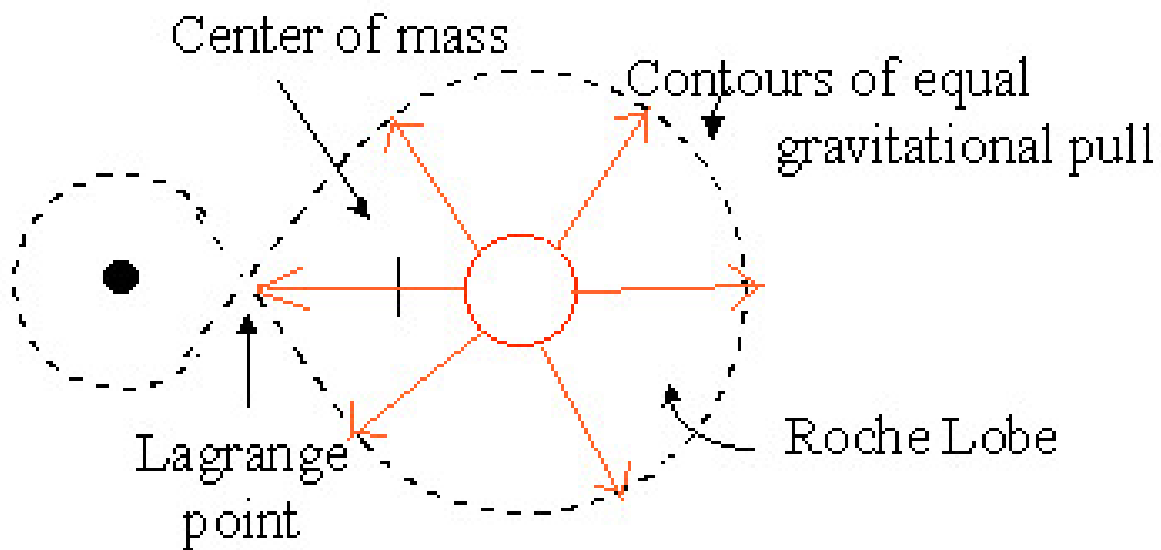
Figure 2.3: Simplified diagram of a compact star (black dot) with a hydrogen rich binary companion (red circle). Each star is surrounded by an imaginary surface called the Roche lobe, which indicates the point where each star's gravity dominates. The point where the Roche lobe of each star meets is called the inner Lagrangian point and at this point the effects of gravity and rotations cancel Credit: [Cornell, `http://hosting.astro.cornell.edu/academics/courses/astro201/roche_lobe.htm`]

burst of X-rays typically lasts for less than one minute and can recur at irregular time intervals of days to months depending on the masses of the stars, distance between the stars, accretion rate, and chemical composition of accreted matter. A typical X-ray burst will show rapid increase in x-rays over the first 10 seconds followed by exponential decrease over the next 100s of seconds. The so-called x-ray burst light-curve is the only observable quantity which can be detected from earth, and attempts to reproduce this light-curve accurately in computational models provide information about the neutron star and the explosion.

The deep gravitational potential well of the neutron star is great enough that the elements synthesized in the burst will fall back onto the neutron star, affecting the evolution of its crust. Therefore, it is unlikely that x-ray bursts contribute much to the chemical evolution of our galaxy. The bursts can, however, provide information about the properties of the neutron star, such as its mass, size, and elemental abundance.

2.1.2.1 Hot-CNO cycles and Breakout

During stellar burning in stars the CNO cycle, or carbon-nitrogen-oxygen cycle, is a catalytic cycle which effectively fuses 4 hydrogen atoms into a helium atom through a multi-step process of proton captures and β-decays on CNO isotopes. For stars with mass $M > 1.3 M_\odot$, this cycle dominates the production of energy. At these temperatures the proton capture reactions proceed at a much slower rate than β-decay lifetimes and the cycle is said to be reaction limited.

During a Type-I X-ray burst at thermonuclear temperatures the reactions begin to proceed at a much faster pace than the β-decays, which are independent of temperature, and the CNO process becomes β limited and this is referred to as the Hot CNO cycle.

There are multiple Hot-CNO cycles which can occur following the helium flash stage.

27

Figure 2.4 shows the different cycles which occur that effectively fuse four protons into a helium atom. During this cycle proton captures and (p, α) reactions compete with β-decays.

If we consider the HCNO1 cycle, for instance, the β-decay half-life of ^{14}O is 102 seconds and ^{15}O has a half-life of 176s whereas the reactions proceed almost instantaneously with respect to the β decays.

The bottleneck for proceeding to higher masses is caused by the long β-decay lifetimes of ^{14}O and ^{15}O which are considerably longer than a typical Type-I x-ray burst. However, if an x-ray burst achieves temperatures $T \geq 0.5$ GK, reaction sequences which break out of HCNO cycles into the $A > 20$ become more likely. The proposed breakout sequences ^{15}O$(\alpha, \gamma)^{19}$Ne, ^{14}O$(\alpha, p)^{17}$F$(p, \gamma)^{18}$Ne$(\alpha, p)^{21}$Na, and ^{14}O$(\alpha, p)^{17}$F$(\gamma, p)^{16}$O$(\alpha, \gamma)^{20}$Ne all involve capture of an α particle on these bottleneck oxygen isotopes. The first reaction of the first sequence ^{15}O$(\alpha, \gamma)^{19}$Ne is expected to be the most important reaction to study, kicking in to allow HCNO breakout first as the temperature rises, in order to more accurately model the x-ray burst light curve [16].

2.1.3   Mathematical Formalism

Nuclear reactions in relatively low temperature stellar environments, such as our sun, tend to occur between nuclei in their ground states. These reactions can be computed by using three variables. The first is the cross-section, σ which characterizes the probability for two nuclei to undergo a reaction. The second is the abundance of the reacting nuclei, and the third is the relative speed between the interacting particles. The cross section can be determined experimentally from the measured reaction rate R,

$$R = \sigma I_a N \tag{2.2}$$
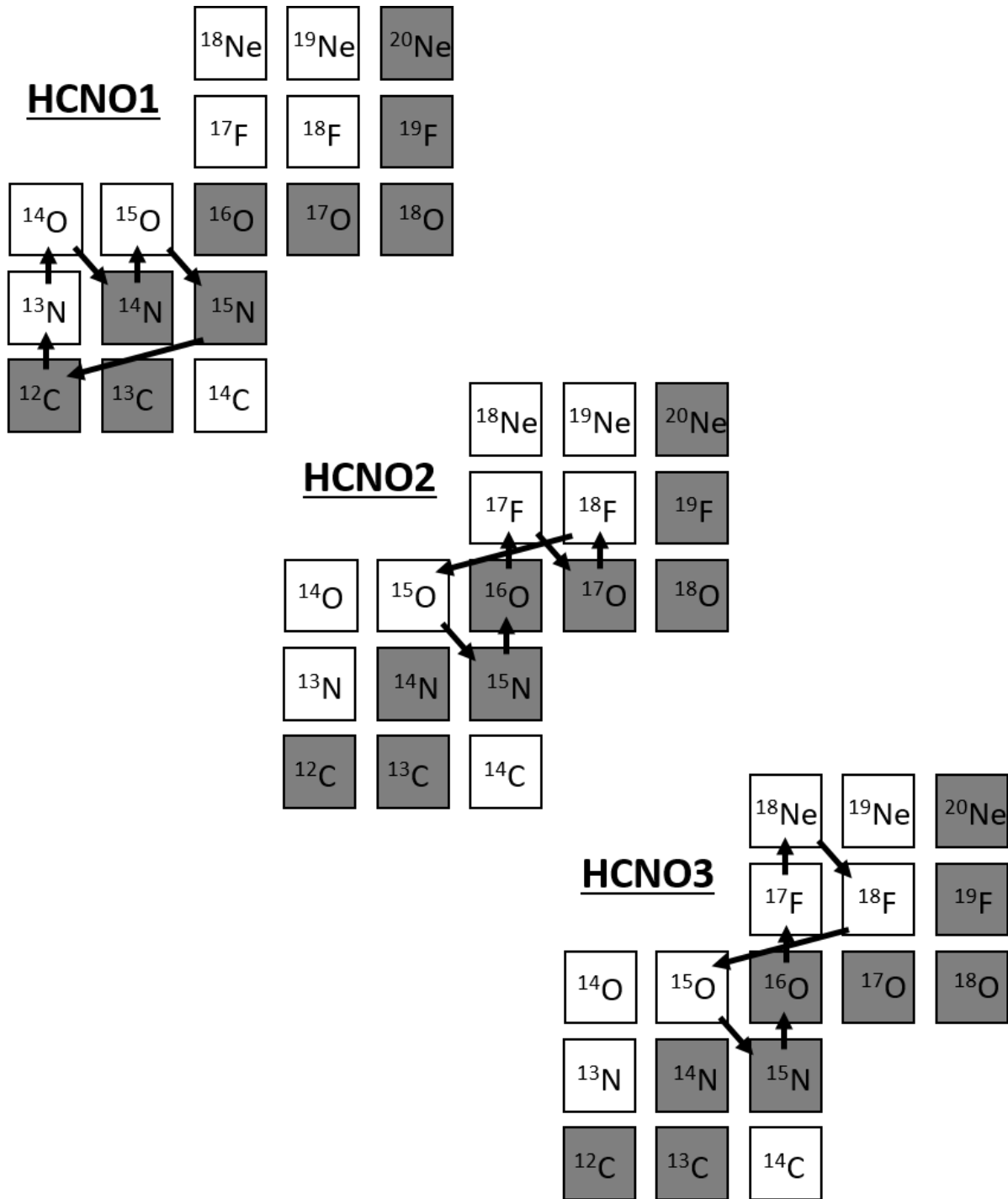
Figure 2.4: The three Hot CNO cycles shown here occur during the second phase of thermonuclear runaway in Type I x-ray bursts. The gray boxes represent the stable isotopes and the arrows show the reactions and β decays that proceed within the different cycles. [Figure adapted from [11]]

where I_a represents the flux of incoming particles and N the number of target nuclei per area.

In a thermonuclear environment where explosive burning occurs, nuclei can be excited from their ground state to excited states by absorbing γ-rays $X + \gamma \longrightarrow X^*$ or through inelastic scattering, i.e. $X(a, a')X^*$ where X^* denotes a nucleus in an excited state. This opens additional channels for nuclear reactions to occur and must be taken into account to model the astrophysical process accurately.

Below we will provide a short derivation of the thermonuclear reaction rate formalism used for Type-I x-ray burst environments and discuss both direct and resonant capture. Following that we will briefly discuss calculating the reaction rate by observing the reverse reaction.

From the description of the cross section in equation 2.2, we can obtain (Eq. 2.3,

$$R_{12} = N_1 N_2 < v\sigma > \tag{2.3}$$

where N_1 and N_2 are the interacting particles, v is the relative velocity between N_1 and N_2, and $\sigma(v)$ is the reaction cross section.

The bracket notation $< v\sigma >$ in equation 2.3 notes that this quantity is averaged since the relative velocity v is described by a continuous distribution in stellar environments.

In principle the cross section $\sigma(v)$ can be described by a geometric factor, the interaction matrix element, and a penetrability factor. Classically this geometric factor is related to the area of the projectile, but quantum mechanically the geometric factor is related to the deBroglie ($\lambda_p = \frac{h}{\sqrt{2mE}}$) wavelength of the projectile instead, and given by $\pi\lambda_p^2$. The interaction matrix element is given by $\mathcal{M} = < f|\mathcal{H}|i >$ where i describes the wave functions

30

of the initial projectiles N_1 and N_2 and f describes the wave functions of the reaction products. Finally, the penetrability $P_l(E)$ describes the likelihood for the projectile to reach the target nucleus. Two effects which strongly reduce the penetrability are the Coulomb barrier and the angular momentum barrier. For charged particles the nuclei must overcome a repulsive Coulomb force which peaks at the nuclear radius. Since angular momentum values must be discrete in quantum mechanics, $L = \sqrt{l(l+1)}\hbar$, any incoming projectile with nonzero impact parameter will have less radial kinetic energy available to overcome the central potential and this manifests itself as the angular momentum barrier. Using these three factors the cross section can be written as

$$\sigma \propto \pi \lambda_p^2 \cdot | < f|\mathcal{H}|i > |^2 \cdot P_l(E) \tag{2.4}$$

where E is the energy of the incoming projectile. At astrophysical temperatures, the penetrability factor $P_l(E)$ is dominated by the $l = 0$ term and can be expanded to be dependent only on the Sommerfeld parameter η:

$$P_l(E) \propto e^{-2\pi\eta}, \eta = \frac{Z_1 Z_2 e^2}{\hbar}\sqrt{\frac{\mu}{2E}} \tag{2.5}$$

Z_1 and Z_2 describe the charge of the target and projectile nuclei, e is the elementary charge carried by a single proton, and μ is the reduced mass of the two nuclei.

Because the velocities are non-relativistic and particles are in thermal equilibrium, the Maxwell-Boltzmann distribution can be used to represent the statistical velocities:

$$f(v) = 4\pi \left(\frac{\mu}{2\pi kT}\right)^{3/2} v^2 e^{\frac{-\mu v^2}{2kT}} \tag{2.6}$$

The variables represented in equation 2.6 are $\mu = \frac{m_1 m_2}{m_1 + m_2}$, denoting the reduced mass, k the Boltzmann constant, T the temperature of the explosive environment, and v the relative velocity between the reaction nuclei. By substituting in the Maxwell-Boltzmann distribution for the relative velocities of the particles in equation 2.3 we obtain the reaction rate:

$$R_{12} = 4\pi N_1 N_2 (\frac{\mu}{2\pi kT})^{3/2} \int_0^\infty v^3 \sigma(v) e^{\frac{-\mu v^2}{2kT}} dv \qquad (2.7)$$

The center of mass energy E, rather than their relative velocities, is often used to characterize the kinetic energy between two particles and it is helpful to transform equation 2.7 into the center-of-mass frame and is often written as the average rate per particle pair:

$$R_{12} = \sqrt{\frac{8}{\pi\mu}} \frac{N_1 N_2}{(kT)^{3/2}} \int_0^\infty E\sigma(E) e^{-E/kT} dE$$

$$< \sigma v >_{12} = \frac{R_{12}}{N_1 N_2} \sqrt{\frac{8}{\pi\mu}} \frac{1}{(kT)^{3/2}} \int_0^\infty E\sigma(E) e^{-E/kT} dE \qquad (2.8)$$

From the derivation of the reaction rate in equation 2.8, we can see that the cross section and the energy of the particles both contribute in different ways to the overall reaction rate. The cross-section of rapid proton capture in thermonuclear environments is proportional to $\sigma(E) \propto 1/e^{-\sqrt{E}}$. Graphing both the cross-section and Maxwell-Boltzman distributions as a function of energy shows that at very low energies, the particles cannot overcome the penetrability factor determined by the cross-section, but there is also a low probability for nuclei to have energies, given by the Maxwell-Boltzman distribution, which can overcome the penetrability. Figure 2.5 also shows the convolution of these two distributions which determines the probability as a function of energy for charged particle reactions to occur. The spike in probability is referred to as the Gamow-window and represents the energy at which most charged-particle reactions take place in thermonuclear burning.
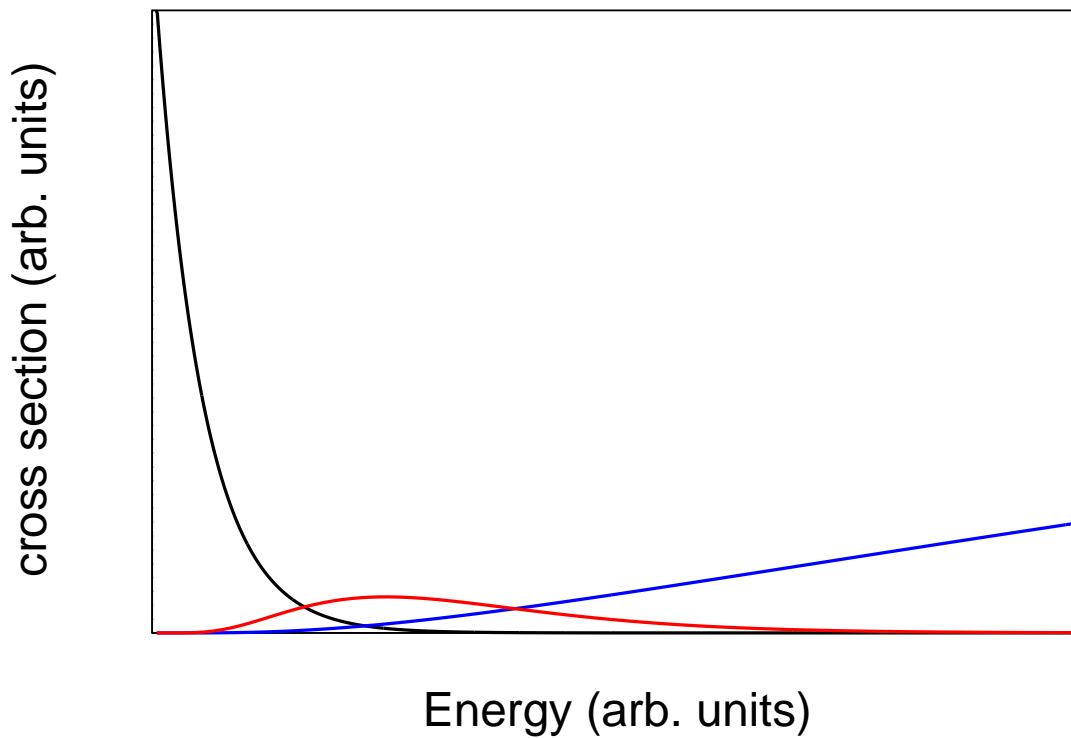
Figure 2.5: Example Gamow window (red) which is created from the convolution of the Maxwell-Boltzman distribution (black) with the penetration factor $P_l(E)$ (blue). The Gamow peak is enhanced by a factor of 100 to make the peak more visible.
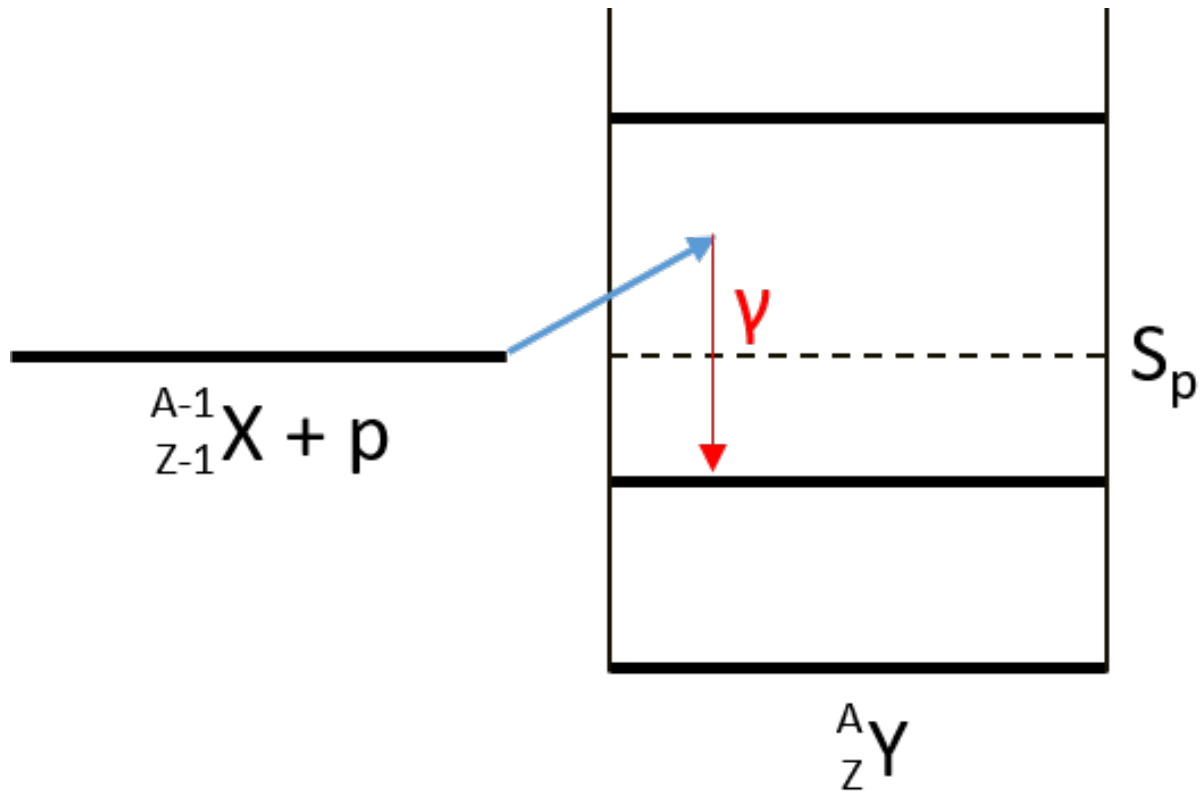
Figure 2.6: This simple figure illustrates a direct capture reaction of a nucleus X and a proton. The resulting nucleus Y emits a γ-ray and settles into a bound state. The dotted line denotes the separation energy of a proton S_p, or the energy required to remove a proton from the nucleus.

While this is one consideration experimentalists take into account when performing reaction experiments, another important consideration involves resonance reactions, which like the Gamow window can also dramatically increase the rate at which reactions proceed depending on the kinetic energies of the nuclei.

2.1.3.1   Direct and Resonant Capture Reactions

From equation 2.8 we have defined what is known as a direct thermonuclear reaction rate for charged particles. To understand what this means it is helpful to reference a diagram of the particle capture with respect to the excited states in the resulting nucleus.

In Figure 2.6 the total mass of the reactants will be slightly larger than the ground state mass of the final nucleus and this is how energy is generated in stars. The particle, in this case a proton, is captured to what is called a bound state which is defined to be below the separation energy S_p, or the energy it takes to remove that particle from the final nucleus. The excess energy is released via γ radiation. In principle a nucleus has a multitude of separation energies for different particles such as neutrons, protons, and α particles which are all relevant to nucleosynthesis.

In the case where the product nucleus has an excited state which is close to the center of mass energy of the reaction particles, the two particles can proceed via resonant capture. Perhaps one of the most famous resonant capture reactions is the triple-α process [5]. There are no stable nuclei with 5 or 8 nucleons, and this process is physically necessary in order to bypass this gap in stability in order for carbon to be produced in stars.

In Figure 2.7 we see that while ^{8}Be is unstable it can exist long enough to fuse with an α particle to create ^{12}C. Rather than capture a particle to a stable state of the product nucleus, resonant capture to the Hoyle state, an excited state in ^{12}C predicted by Hoyle at 7.7 MeV, will result in the capture of a particle to an unbound state. It is possible for this excited state to re-emit the particle or it can de-excite to a bound state of ^{12}C via γ-emission.

The probabilities that the α particle will be re-emitted by ^{12}C or de-excite via γ decay are related to the partial widths Γ_γ and Γ_α of the excited state, where the total width $\Gamma = \Gamma_\gamma + \Gamma_\alpha$. The width of a resonance is expressed in units of energy and the probabilities of each decay are determined by the branching ratios Γ_γ/Γ and Γ_α/Γ.

For resonant capture, the cross section $\sigma(E)$ in equation 2.8 is given by the Breit-Wigner
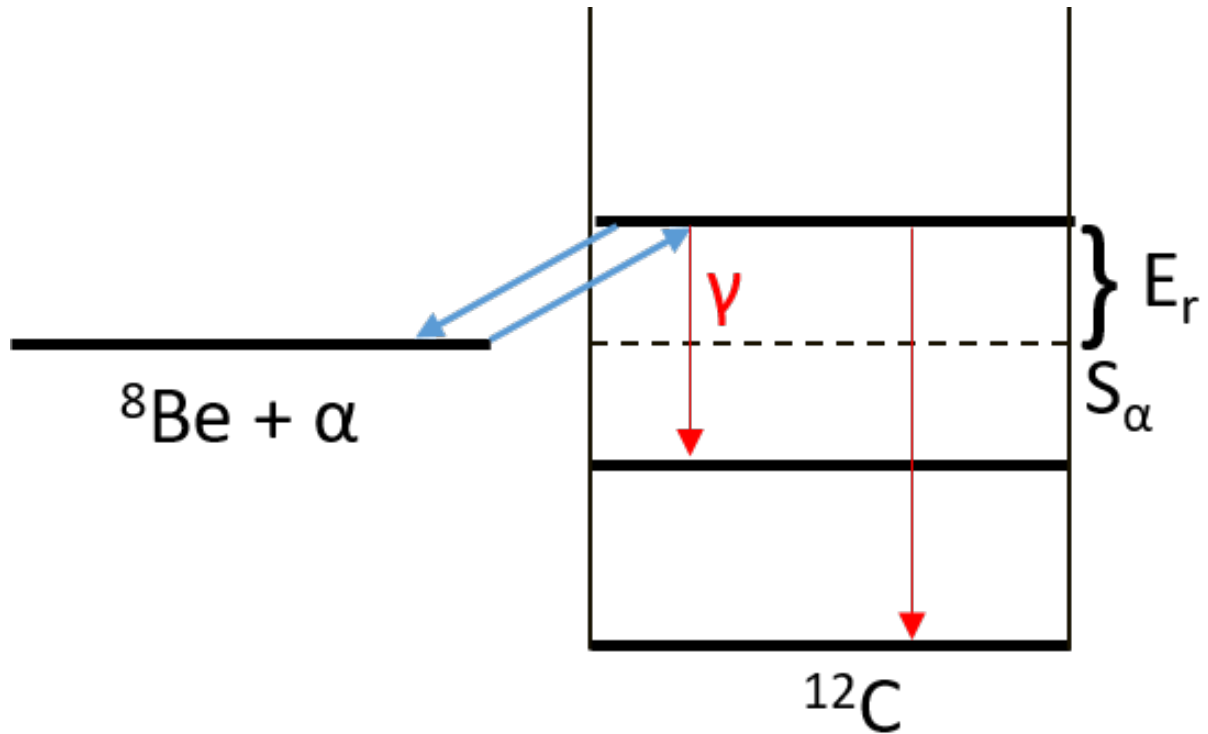
Figure 2.7: This simple figure illustrates the famous triple α resonant reaction. In this case the α particle is captured onto an excited state in ^{12}C where the nucleus can either decay via γ-rays to a bound state or the α particle could be re-emitted. The resonance energy E_r is the difference between the excitation energy in ^{12}C and the α particle separation energy S_α

formula:

$$\sigma(E) = \frac{\lambda^2}{4\pi} \omega \frac{\Gamma_1 \Gamma_2}{(E - E_r)^2 + (\Gamma/2)^2}, \quad \omega = \frac{2J_r + 1}{(2J_a + 1)(2J_b + 1)} \tag{2.9}$$

where λ lambda is the DeBroglie wavelength of the incoming projectile, Γ_1 and Γ_2 are the partial widths related to the two modes of decay, E and E_r are the center of mass energy and the resonance energy respectively, and J_a, J_b, and J_r are the spins of the reaction and product nuclei.

By making the assumption that the width of the resonance is narrow and isolated ($\Gamma \ll E_r$), which is the case for both the $^{15}O(\alpha, \gamma)^{19}Ne$ and $^{19}Ne(p, \gamma)^{20}Na$ reactions considered in the present work, the formula for the resonance reaction rate associated with a single resonance can be reduced to:

$$< \sigma v > = \left(\frac{2\pi}{kT\mu}\right)^{3/2} \hbar^2 e^{-E_r/kT} \omega\gamma, \quad \gamma = \frac{\Gamma_1 \Gamma_2}{\Gamma} \tag{2.10}$$

Assuming E_r is known, all factors in equation 2.10 are reduced to a constant except $\omega\gamma$ (not to be confused with gamma-ray, γ) and this is called the resonance strength. This means we can experimentally measure the branching ratios of specific decay channels (from an astrophysical resonance), in addition to the spins and lifetimes of the relevant states, my measuring the reaction rate, rather than trying to recreate the direct reaction! This is extremely important for experimentalists because it is sometimes very difficult or impossible to measure the cross section of a resonant reaction directly, especially when one of the reactants is unstable.

2.2   The ^{15}O$(\alpha, \gamma)^{19}$Ne Reaction Rate

In the study of Type I x-ray bursts there are a few reaction bottlenecks whose unknown or highly uncertain rates can have large effects on simulated burst profiles. The most important reaction rate to determine is the ^{15}O$(\alpha, \gamma)^{19}$Ne Hot CNO cycle breakout reaction which heavily affects the onset of the burst [16]. A single resonance is expected to dominate the reaction rate and corresponds to an excitation energy of $E_x(^{19}$Ne$) = 4.03$ MeV.

It is not possible with current facilities to directly measure the ^{15}O$(\alpha, \gamma)^{19}$Ne reaction rate because an ^{15}O rare isotope beam of sufficient intensity is not available. However, the resonance strength can be indirectly determined from measurements of the spin, lifetime, and branching ratio Γ_α/Γ of the 4.03 MeV state. Currently, the spin is known to be $3/2^+$ [17] and the lifetime has been measured [18, 19, 20] to sufficient precision leaving the α-decay branch the only quantity left to be measured.

2.2.1   Previous studies of ^{15}O$(\alpha, \gamma)^{19}$Ne

Many different transfer reaction methods have been utilized in order to populate the 4.03 MeV state in ^{19}Ne and subsequently search for the α branching ratio. The first transfer reaction $p(^{21}$Ne,^{3}H$)^{19}$Ne* utilized *inverse kinematics* (heavy beam and light target) to produce the ^{19}Ne* and tritons (^{3}H) [21]. The combination of tritons and low energy α particles provides a unique energy signature when searching for the α branch. The background in this experiment was small and well measured, but they were not sensitive to the α branch from the 4.03 MeV state due to insufficient statistics and only determined an upper limit of $\Gamma_\alpha/\Gamma < 4.3 \times 10^{-4}$. A second transfer reaction by Rehm *et al.* ^{3}He$(^{20}$Ne$, \alpha)^{19}$Ne* was used and produced no background in the search region for the α branch, but were also not sensi-

tive to the low energy α particles and also produced an upper limit of $\Gamma_\alpha/\Gamma < 6 \times 10^{-4}$ [22]. Finally, the $^{19}\text{F}(^3\text{He}, t)^{19}\text{Ne}^*$ transfer reaction was used by Tan *et al.* [23] which produced a much higher background than the other two experiments but with increased statistics. From this experiment an α branching ratio of $\Gamma_\alpha/\Gamma = 2.9 \pm 2.1 \times 10^{-4}$ was extracted. However, this value is controversial because it is nearly consistent with 0 and the modeling of the background is not well determined at the lowest energy α branches [24].

Other experiments also employed transfer reactions to populate $^{19}\text{Ne}^*$ states above the α separation energy, S_α [25, 26, 27] but were not sensitive the α branch from the 4.03 MeV state.

Using transfer reactions to populate the 4.03 MeV state in ^{19}Ne and subsequently measure Γ_α/Γ has thus far proved elusive [28, 29]. Transfer reactions produce a lot of different by-products and can create a significant amount of statistical noise, suppressing the ability to detect α particles above background. Additionally, α particles are emitted at very low energy from the 4.03 MeV state because the resonance $\approx$500 keV is very close to the α separation energy and the α particle will also lose $\approx 20\%$ of its kinetic energy via the recoiling ^{15}O due to conservation of momentum.

2.2.2 Purpose of This Work

Rather than relying on transfer reactions to populate the 4.03 MeV state in ^{19}Ne, a recently proposed technique for measuring Γ_α/Γ employs the decay sequence $^{20}\text{Mg}(\beta p \alpha)$ for which the last step is α-particle emission to ^{15}O, the inverse of α capture [30]. An important component to identifying $p - \alpha$ coincidence events of interest is the unknown energy of the proton(s) emitted from the excited states in ^{20}Na which feed the 4.03 MeV state in ^{19}Ne.

In the present work, we employ a γ-ray spectroscopy technique to measure the proton

energy. When a nucleon is emitted from a nucleus, following β decay, the momentum of the system must be conserved so the daughter nucleus will recoil with equal and opposite momentum as the ejected nucleon. If a γ ray is emitted before an excited daughter nucleus has time to stop the resulting γ ray will be Doppler shifted. The resulting γ ray line shape will be broadened. The broadened feature preserves information about the energies of the emitted nucleons, which is modeled using a computer simulation.

2.3 The $^{19}\text{Ne}(p,\gamma)^{20}\text{Na}$ Reaction Rate

The $^{19}\text{Ne}(p,\gamma)^{20}\text{Na}$ reaction (Q=2190 keV) [31, 32] is expected to be dominated by the only resonance in the Gamow window at 457 keV (E_x=2647 keV) above the proton threshold (Fig. 4.1) [33]. The matter of its spin and parity has been debated for nearly 30 years because these quantities are crucial to determining the resonance strength. The most likely values for a spin and parity assignment have been suggested to be 1^+ or 3^+ [34]. A J^π of 1^+ would result in a significantly slower reaction rate than a 3^+ assignment [33, 35] and would be more likely to cause the ^{19}Ne ($J^\pi = 1/2^+$) to return to the hot-CNO cycles rather than breaking out to higher mass nuclei.

2.3.1 Previous studies of $^{19}\text{Ne}(p,\gamma)^{20}\text{Na}$

Many different types of experiments have been carried out in the past to extract information about the 2647 keV state including stable beam reaction experiments, rare isotope beam experiments and β-decay experiments.

Early experiments focused mainly on stable beam transfer reactions in order to populate the state. Kubono *et al.* discovered the $\approx$2647 keV ^{20}Na state via the $^{20}\text{Ne}(^3\text{He,t})^{20}\text{Na}$ [36]

reaction and subsequently Lamm *et al.* remeasured the same reaction and argued for a 1^+ assigment based on a DWBA analysis [37]. Smith *et al.* also measured the ^{20}Ne(^{3}He,t)^{20}Na reaction and improved the precision of the ^{19}Ne(p,γ)^{20}Na resonance energies [38]. A theoretical study of the mirror energy levels in ^{20}F and ^{20}Na by Brown *et al.* determined from the available data that a 3^+ assignment of the 2647 keV state was more likely by pairing it with the 2966 keV mirror state in ^{20}F [33]. The state has also been observed via the ^{20}Ne(p,n)^{20}Na reaction through which a 3^+ assignment was made based on the angular distribution of the neutrons [39]. Concurrent with the present work, Belarge *et al.* used a rare-isotope beam of ^{19}Ne to measure the ^{19}Ne(d,n)^{20}Na proton transfer reaction and were able to populate the three lowest energy resonances and observe their proton emissions to both the ground state and excited states [40], arguing for a J^π of 3^+ for the 2647 keV state based on the analysis of the reconstructed neutron angular distribution.

The β-decay of ^{20}Mg ($J^\pi=0^+$) to ^{20}Na has been utilized because it constrains the J^π of the 2647 keV state experimentally. If the J^π of the state were 1^+ then its β-decay feeding by ^{20}Mg would be allowed by β-decay selection rules. However, if the state were 3^+ then the β transition would be second-forbidden and very weak. An early study of ^{20}Mg β-delayed proton decay by Görres *et al.* determined an upper limit on the feeding of the 2647 keV state to be 2×10^{-3} under the assumption that proton emission dominates over γ-ray emission [41]. Piechaczek *et al.* also conducted a ^{20}Mg β-decay study which yielded an upper limit on the β-decay feeding of 1×10^{-3} to the 2647 keV state in ^{20}Na [42]. The experiment by Piechaczek *et al.* searched for protons and also for selected γ-rays but did not find any evidence for the 2647 keV state being populated at their level of sensitivity. A recent study of ^{20}Mg β-delayed proton emission by Wallace *et al.* yielded the most stringent upper limit on the partial β-decay branch to the 2647 keV state of 2×10^{-4} leading to a partial log ft of

>6.9 [35], making a 1^+ assignment unlikely under the implicit assumption that the proton branching ratio is large. Recent experiments by Sun *et al.* [43] and Lund *et al.* [44] searched for both protons and γ-rays but did not have enough statistics to improve upon the previous constraints on J^π.

Rare isotope beams of ^{19}Ne have been used to search for the important resonance directly at astrophysical energies. Two experiments yielded upper limits on the resonance strength of 21 meV [45] and 15 meV [46] with 90% confidence. A recent experiment concurrent with the present work conducted at TRIUMF utilized a high intensity ^{19}Ne beam and was able to measure the resonance strength directly for the first time [47] to be 17^{+7}_{-5} meV.

2.3.2 Purpose of This Work

Previous analysis of ^{20}Mg β-decay to the 2647 keV state has relied heavily on the protons emitted from this state and has rarely addressed the γ-ray branch. In fact, a complete experimental upper limit on the β-decay feeding of this state has never been set. Either 1^+ or 3^+ assignments should yield a γ-decay branching ratio Γ_γ/Γ on the order of 10% [45]. This value is based on theoretical estimates and could be larger. Therefore, it is important to measure the β-delayed γ-decay branch or limit it experimentally. In the present work, we describe a search for these ^{20}Mg β delayed γ-rays to complement the previously measured upper limit [35] on the proton branch. This work was done concurrently with the direct reaction rate experiment at TRIUMF [47].

Chapter 3

Experiment E14066 at the National Superconducting Cyclotron Laboratory

Experiment E14066 was carried out at the National Superconducting Cyclotron Laboratory at Michigan State University in May 2015. The experiment lasted for five days beginning on May 8 and ending on May 13. Hour long data runs were taken during the experiment to ensure consistent measurements from our assortment of detectors. Additional runs were taken before and after the experiment for calibration purposes and to characterize the background (see section 5.1.1.6 for treatment γ-ray of background).

3.1 Purpose

We utilize ^{20}Mg β-decay in order to populate excited states in ^{20}Na and ^{19}Ne. As stated in the previous chapter, the purpose for this work is two fold.

First we search for γ-rays emitted from the excited state resonance in ^{20}Na at 2647 keV to determine $I_{\beta\gamma}$, the intensity of ^{20}Mg β decays which feed the 2647 keV state and de-excites followed by γ-ray de-excitation. This measurement can be used in conjunction with previous searches for the protons emitted from this state, which yielded an upper limit on $I_{\beta p}$

measured by Wallace et al. [35]. This combined upper limit can be used to help determine the J^π of this state and constrain the astrophysical reaction rate important in the breakout of the HCNO cycle in Type I x-ray bursts.

Secondly, we search for and characterize γ-rays emitted from the 4.03 MeV excited state in ^{19}Ne. By utilizing ^{20}Mg(βp), we can determine if this reaction sequence can populate the 4.03 MeV excited state sufficiently to search for the α-particles in a future experiment.

3.1.1 Beam Production

Stable Primary beam particles are stripped of their electrons and injected into the center of the first cyclotron where a transverse magnetic field causes these charged particles to move in a circular motion. A rapidly changing electric field is applied in the direction of the ions, causing them to accelerate. The radius of the charged particles in the cyclotron will continue to increase along with their speed until they reach the desired electrostatic channel used to extract ions, where they exit along the beam line before heading to the second cyclotron to pick up more energy.

The primary beam for this experiment was ^{24}Mg and was accelerated through the K500 and K1200 CCF at the NSCL to an energy of $\sim$170 MeV/u. The intensity of the primary beam was 60 pnA (particle nanoamperes). The ^{24}Mg beam was then impinged on a ^{9}Be target with a thickness of 987 mg/cm^2. This fragmentation procedure knocks out nucleons from the nuclei of some ions in the primary beam that hit the target and produces a cocktail beam of both stable and radioactive isotopes including the desired ^{20}Mg.

The fragmentation of the primary beam produces a lot of contaminants in the secondary beam, which we do not want to deliver to the target. The A1900 magnetic separator is used to remove the bulk of these unwanted particles. The A1900 includes 4 dipole magnets and a
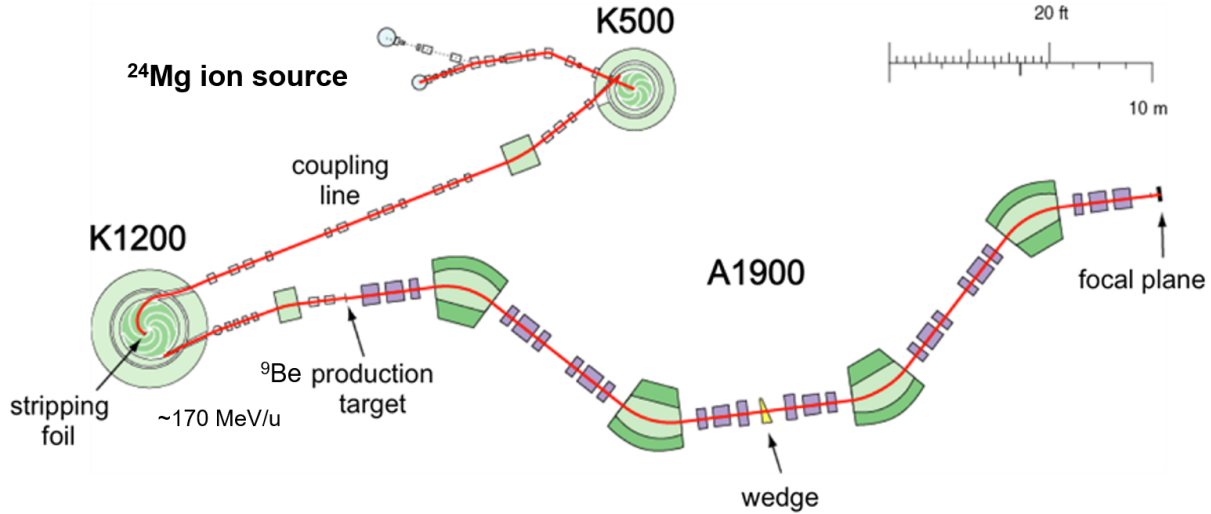
Figure 3.1: A schematic of the K500 and K1200 coupled cyclotron feeding into the A1900 magnetic separator. The ^{24}Mg stable primary beam is accelerated through the couple cyclotrons to $\sim 1/2$ the speed of light and impinged onto the ^{9}Be target. The fragments of the secondary beam are separated using 4 dipole magnets (green) and an aluminum degrading wedge (yellow). The secondary beam is then delivered to our experimental setup in the S2 vault.

wedge degrader. The dipole magnets separate out fragments according to the Lorentz force $mv/q = B\rho$ where m is the mass of the ion, v the velocity, q the charge of the nucleus, and $B\rho$ represents the *magnetic rigidity*. The magnets in the A1900 are tuned in order to keep the ^{20}Mg at the center of the beam-line and ions with differing magnetic rigidity will travel at different radii and become separated from the secondary beam. Ions with different masses may still share the same rigidity as the desired ^{20}Mg, so a wedge is placed after the first two dipole magnets which slows down ions proportionally with the square of their mass A^2 in order to change the unwanted ions' magnetic rigidity. The wedge degrader is made of aluminum and has an effective thickness of 594 mg/cm^2 for the ^{20}Mg path of travel. A diagram of the beam production can be seen in figure 3.1.

The secondary beam then exits the A1900 magnetic separator through the focal plane where collimating slits are used to block excess unwanted ions. A 1 mm thick scintillator is

Experiment 14066-Wrede

Existing Beamline w/ Thin Kapton Window

Beta SeGA w/ 2" ext. bars on each side to make room for GeDSSD

XYZ SeGA Stand Base
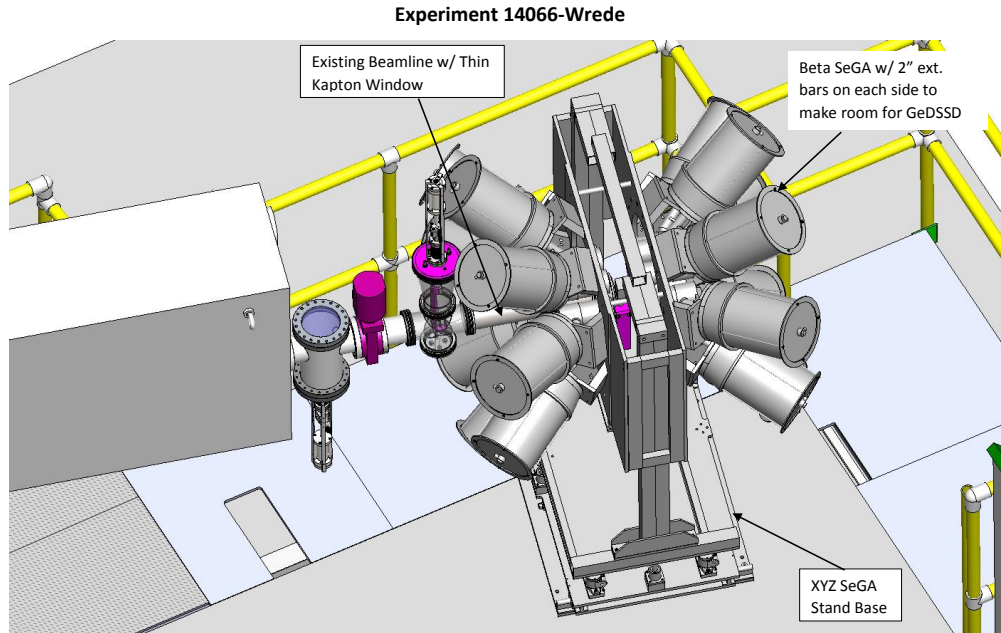
Figure 3.2: A birds-eye view of the experimental setup drawn using computer-aided design (CAD) software.

also placed at the focal plane of the A1900 which is used to identify particles and will be discussed in the next section. After passing this A1900 X-focal plane (XFP) scintillator the secondary beam is delivered to our experimental setup in the S2 vault of the NSCL.

3.1.2 Experimental Setup

There are three types of detectors included in our experimental setup. These detectors consist of a silicon PIN detector (Fig. 3.4), 16 high-purity germanium detectors (SeGA), and a plastic scintillator (Fig. 3.5).

The silicon PIN (positive-intrinsic-negative) detector was located $\sim$1 m upstream of the

46

plastic scintillator and germanium detectors. The PIN detector consists of a p-type semi-conductor (positive charge from electron hole), intrinsic-type semiconductor (neutral), and n-type semiconductor (negative charge) sandwiched together. A reverse bias (voltage) applied to the PIN detector will produce an electric field which outputs a signal when charged beam particles pass through and create charge carriers, where the signal strength is proportional to the square of the charge Z^2 of the ion. In our case a voltage of 22.0 V was applied to the 300-μm-thick Si PIN detector while under vacuum. This detector is used in conjunction with the A1900 XFP scintillator to produce a timing signal proportional to the time of flight between the scintillator and the PIN detector. The time-of-flight was measured over a path of 25 m using the Si detector and a scintillator at the focal plane of the A1900. Together, the signal from the PIN detector can be used with the timing signal to produce a particle identification plot (Fig. 3.3) using the ΔE-TOF method. The final beam consisted of 34% ^{20}Mg (Q_{EC}=10.7 MeV), 24% ^{18}Ne (Q_{EC}=4.4 MeV), 12% ^{17}F (Q_{EC}=2.8 MeV), 22% ^{16}O (stable) and 8% ^{15}N (stable).

While the PIN detector is important for general particle identification, the detector cannot be used when the full beam is being delivered to the setup since the high beam current can radiation damage the detector. Therefore, particle ID runs were done intermittently between full beam runs with 30x attenuated beam, and used to ensure the beam composition delivered to the experimental setup was consistent throughout the experiment. A pneumatic drive was used to lower the PIN detector into the beam-line during particle ID runs and removed during production runs. A computer aided design drawing of this drive system is shown in figure 3.4

The beam then travels through a thin kapton window (Fig. 3.5), after which it continues through 20 cm in air before implanting into the EJ200 plastic scintillator. The plastic

47
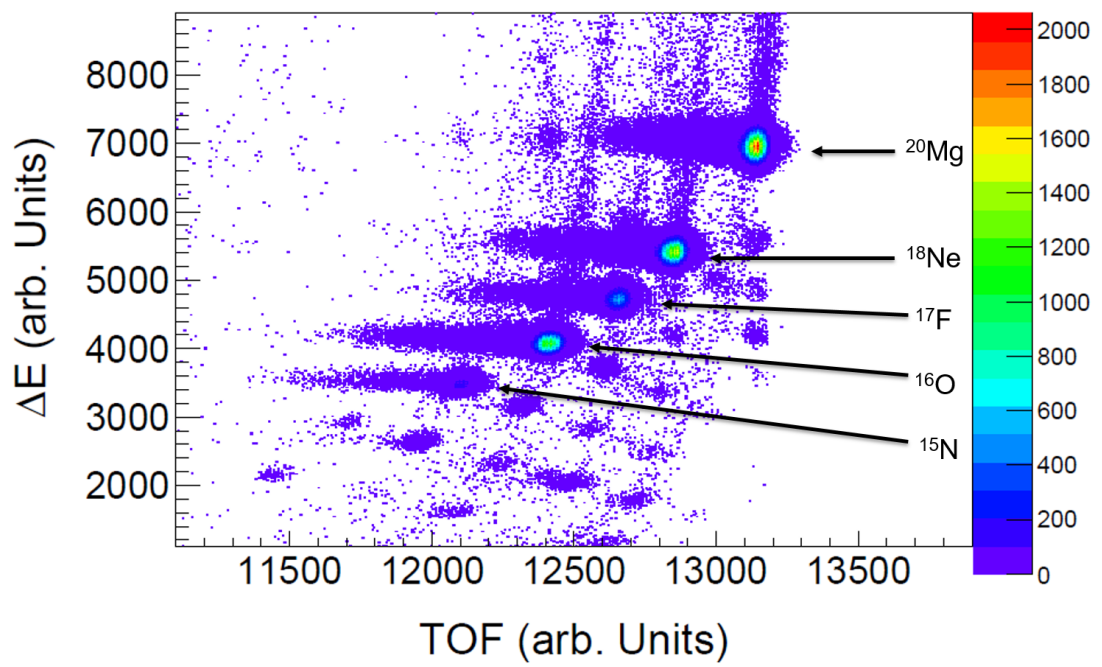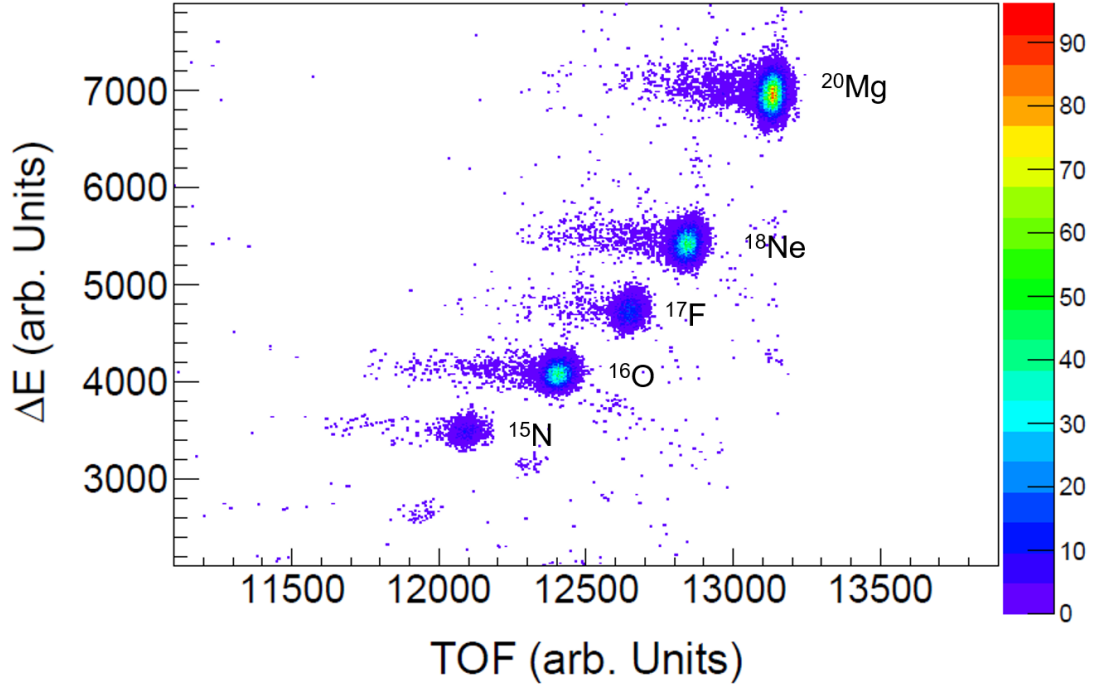
Figure 3.3: TOP: An example particle ID spectrum taken in between full beam runs. The energy lost to the Si PIN detector is plotted against the time of flight (TOF) between the XFP scintillator and the Si PIN detector. The large blob in the top right is the ^{20}Mg and represents $\sim 40\%$ of the secondary beam implanted in the plastic scintillator.

Bottom: The total beam rate was increased in later runs which sacrificed ^{20}Mg purity ($\sim 34\%$) for an increase in ^{20}Mg pps implanted into the plastic scintillator.
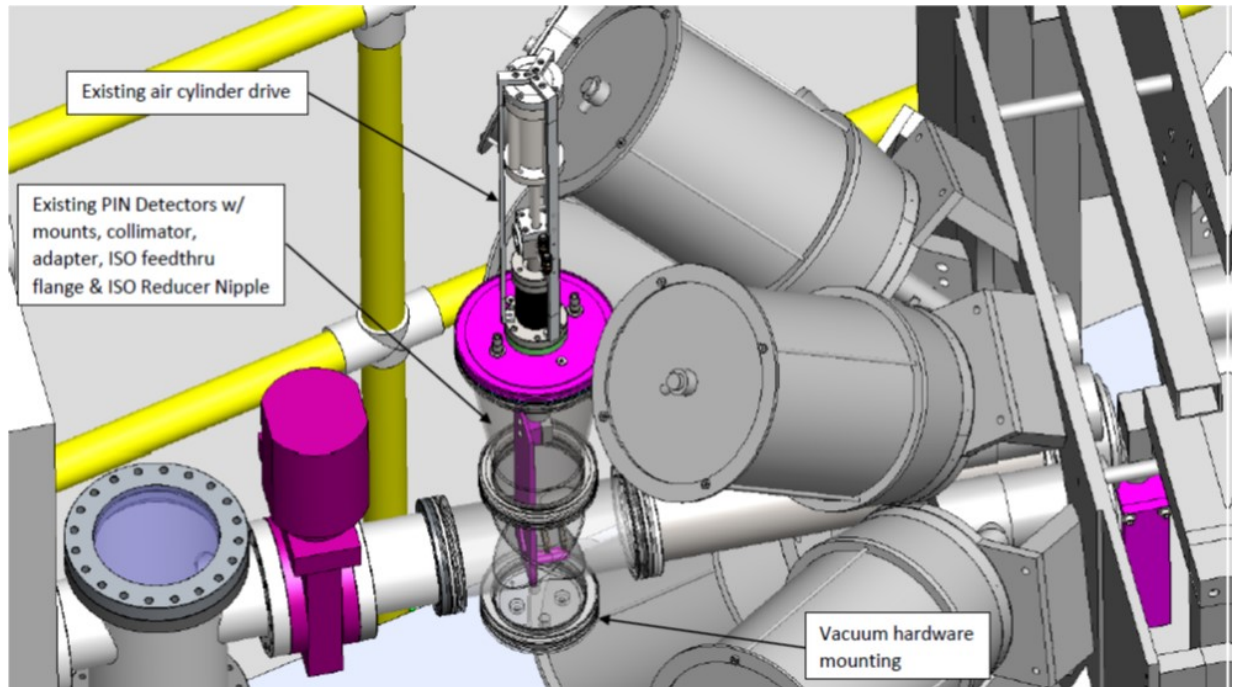
Figure 3.4: The pneumatic drive utilizes a gas cylinder to retract the PIN detector from the beam-line when full beam is on and releases the PIN detector into the beam-line during particle ID runs.

scintillator is a 5.0 x 5.0 by 2.5 cm block and has a photomultiplier tube mounted onto the back. The scintillator was supported mechanically by clamping the phototube onto a long piece of aluminum mounted onto the top of the SeGA frame (Fig. 3.6) so that the face of the scintillator is situated 20 cm front of the kapton window, centered on the beam axis.

The photomultiplier tube mounted on the plastic scintillator was biased to 1000 V during the experiment. A scintillator will produce light when the radiation interacts with it. The photomultiplier tube then amplifies the light signal which is sent to the data acquisition system. The energy resolution of the scintillator is not useful except to distinguish between an implant and a decay since the energies of these events are vastly different. A spectrum of the scintillator energy is shown in figure 3.7 where the energies below 10,000 ADC channels are related to β decays and above 20,000 ADC channels are due to implantation events.

The plastic scintillator is surrounded by 16 high purity segmented germanium detectors

Figure 3.5: The secondary beam exits through a thin kapton window after which it travels 20 cm in air before implanting into the EJ200 plastic scintillator.
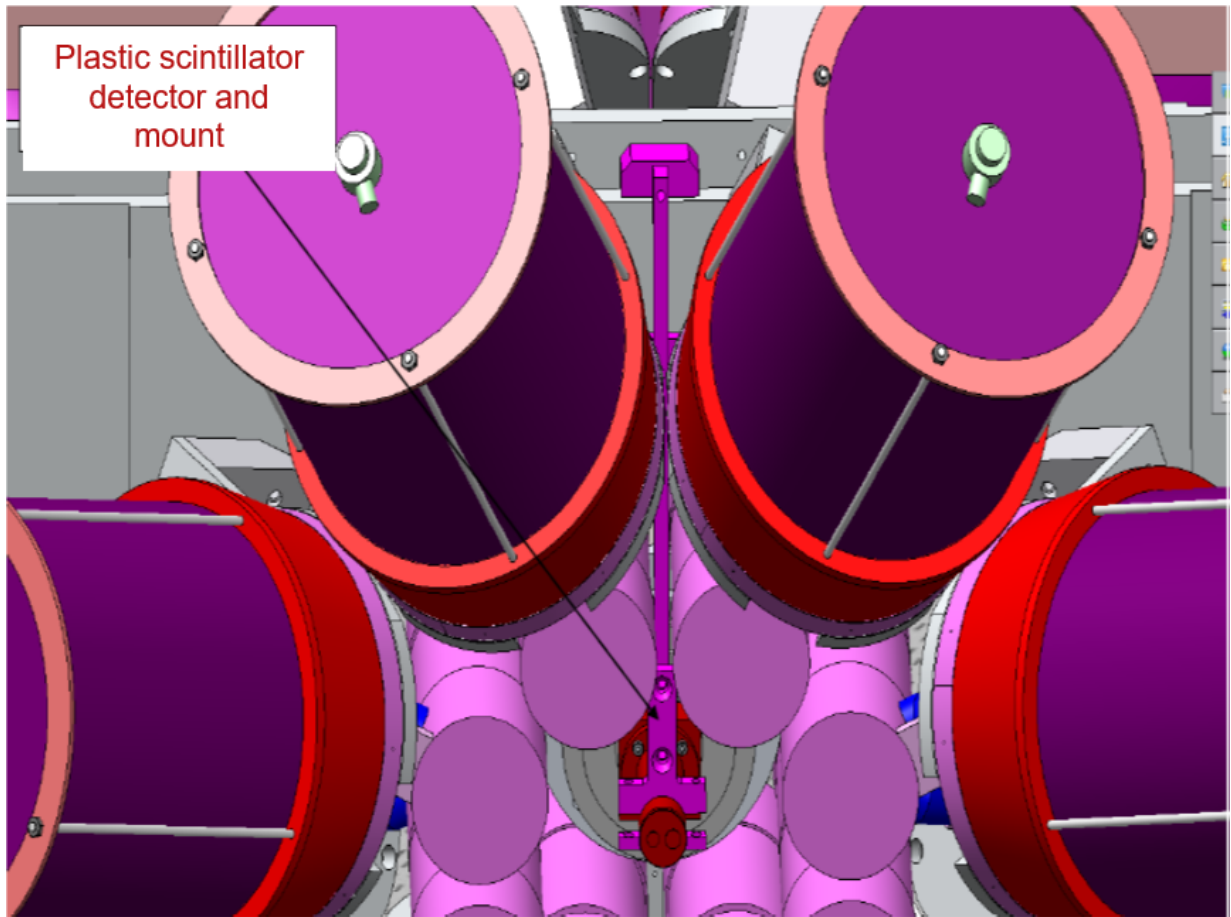
Figure 3.6: To hold the plastic scintillator in front of the thin kapton window an aluminum mount was used which connected to the top of the SeGA support structure and clamped onto the end of the scintillator's photomultiplier tube.
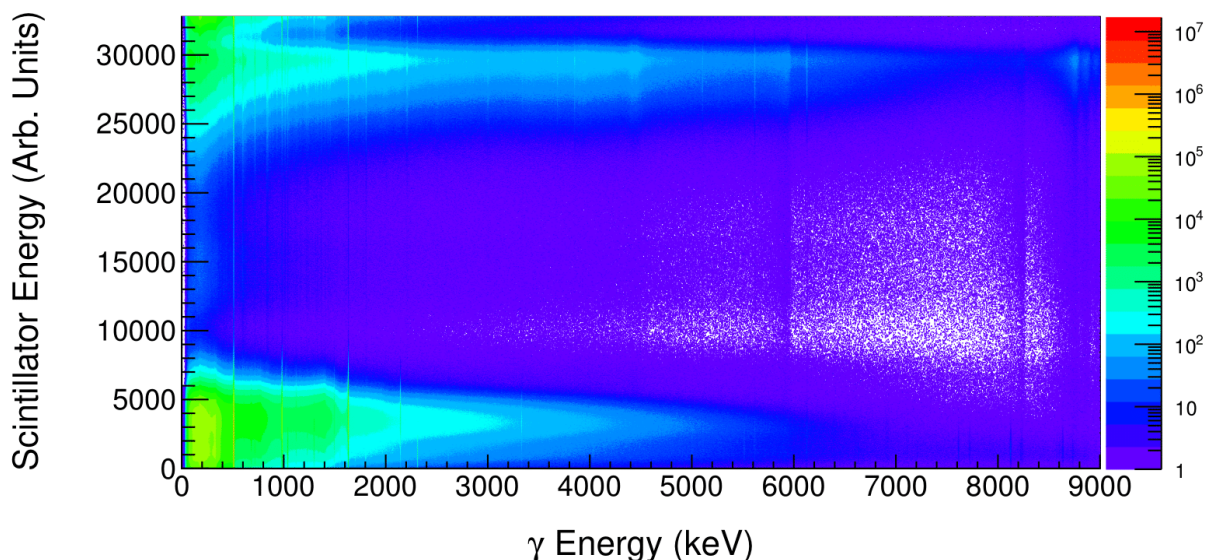
Figure 3.7: A total spectrum of EJ200 scintillator energies detected during E14066 plotted vs γ-ray energies detected in SeGA. The region below 10000 channels is comprised of β-decay events and the γ-ray lines above 20000 channels are related to implant events which we want to remove by placing a *gate* (only looking at specific events) on the β-decay energy region.

(SeGA) in two rings of 8 detectors, one ring downstream and one upstream. Germanium detectors are also positive-intrinsic-negative type detectors and can detect ionizing radiation such as γ-rays between 100 keV and 10 MeV with high resolution. The germanium detectors must be kept cool, due to a lower band gap than in Si, to obtain a consistent energy resolution and avoid damage to the detectors so liquid nitrogen (77° K) is pumped into dewars attached to each segmented germanium detector. These detectors were used to search for γ-ray transitions in ^{20}Na and ^{19}Ne.

Three distinct processes can occur when γ-rays interact with matter. The first is the photoelectric effect where an incident γ-ray is fully absorbed and transfers all of its energy to electrons (called photoelectrons). The photoelectrons are collected at the edge of the semiconductor and produce a signal proportional to the γ-ray energy. The second process is called Compton scattering where the incident γ-ray imparts some of its energy onto an

electron and scatters away. In principle a scattered γ-ray can also produce photoelectrons or it can escape the detector volume without being detected. This interaction causes a characteristic Compton background for a single γ-ray energy. The third type of interaction is called pair production. If a γ-ray has energy greater than 1.022 MeV (the mass energy of two electrons) in the presence of nuclei, then the photon's energy can be converted to particle mass by producing an electron positron pair $(e^+ - e^-)$ [48]. The e^+ will then annihilate with another e^- to produce to 511 keV gamma rays. The probability of pair production occurring increases as a function of the incident γ-ray energy. This process produces a characteristic escape and double escape peak where the energy detected is 511 keV and 1022 keV less than the full photopeak energy.

During the experiment we noticed a much higher rate of γ-ray background at high energies than was expected and it was proposed that some β particles from the β-decays in the scintillator were entering the germanium detectors which can also produce ionizing radiation. To test this hypothesis the plastic scintillator was surrounded with a thick piece of steel to shield the germanium detectors from any escaping βs. There was no reduction in noise, however this helped confirm another process which produced γ-rays in the scintillator. When electrons or positrons are deflected by a charged particle, they will lose energy which is converted into a photon. This process is known as *bremsstrahlung*, or braking radiation, and produces a continuous background in the γ-ray spectrum up to higher energies. The background contribution due to bremsstrahlung was borne out by MCNP simulations using a set of β endpoint energies produced by the β-decays in the scintillator [49, 50]. The total γ-ray background at high energies does not affect our ability to search for γ-ray peaks of interest.

3.1.3 Data Acquisition

The digital data acquisition system (DDAS) is supported by the NSCL and is built around the Pixie-16 digitizer which has the ability to quickly process signals from a variety of different detectors . Each module has 16 channels and is placed in a computing crate where multiple modules can be connected. Prior to running the experiment different parameters for processing signals can be input into the software such as a threshold trigger to filter out low energies as well as a rise time and decay time of signal. Pulse processing is then applied to a trace (Fig. 3.8) and outputs the area of the pulse as a binary number which is stored along with a time-stamp for the signal in an event file. A more detailed application of the NSCL digital data acquisition system (DDAS) can be found in reference [51].

During the experiment all signals detected within a certain time frame are stored in a bucket called an event. The event window defines the length of time where signals are recorded and placed in a single event. During the experiment an event window of 1 μs was used for events with full beam with $\sim$ 12000 particles per second implanted into the scintillator comprised of particles proportionate with the PID runs in figure 3.3. This event length was chosen to avoid pile-up events where multiple signals are detected in the same detector. Particle ID runs required an extended event window of 10 μs.

Events processed by the NSCL digital data acquisition are managed by the Readout program. Each signal processed by DDAS is placed into a buffer where Readout buckets these signals into events defined by the event window. Each of these events are stored in event (*.evt*) files managed by Readout which is also responsible for stopping and starting runs and producing scalers related to the event frequency in each detector for each event file.

The energy signals from the germanium detectors as well as the scintillator and PIN
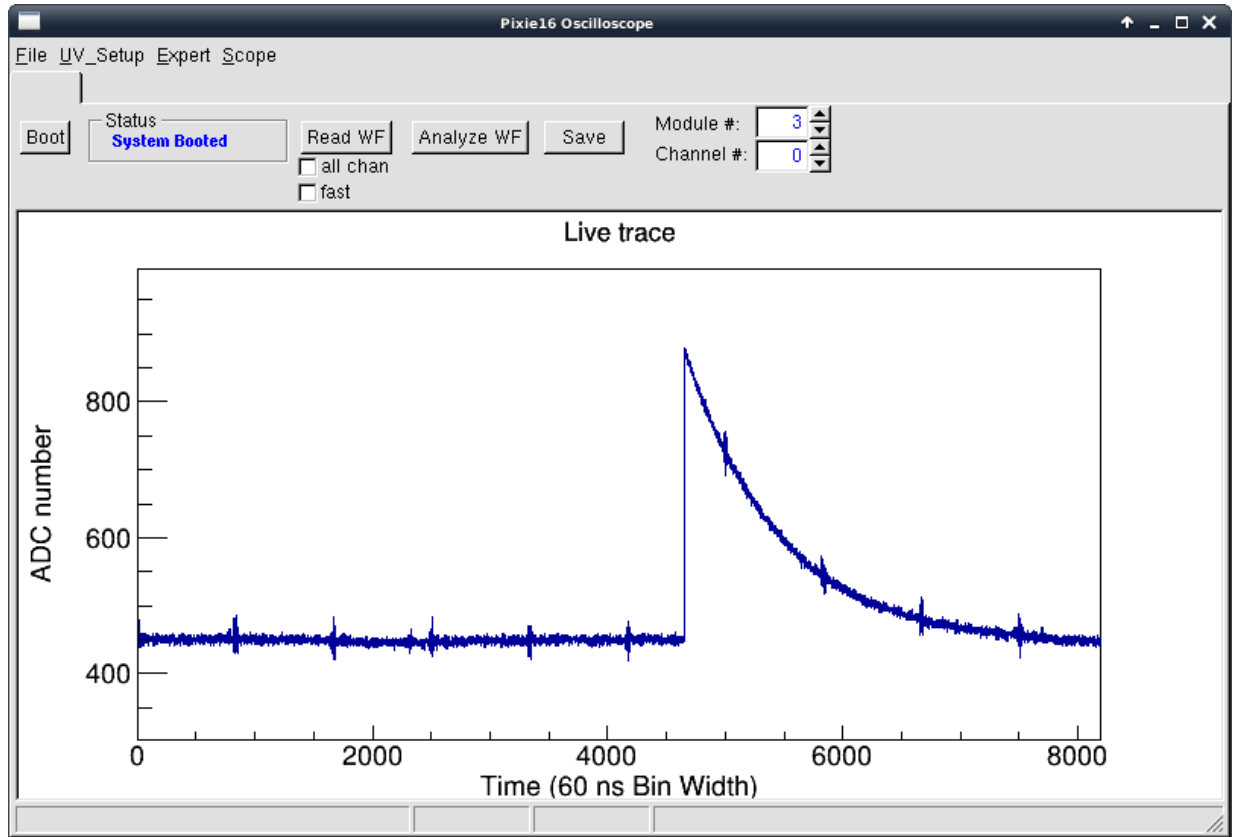
Figure 3.8: An example trace from the silicon PIN detector. The decay time of signals from the Si PIN detector is similar to the SeGA detectors (∼45 μs) and EJ200 plastic scintillator traces decay much faster (∼1 μs). The program used to view the trace as well as test different signal parameters is called NScope.
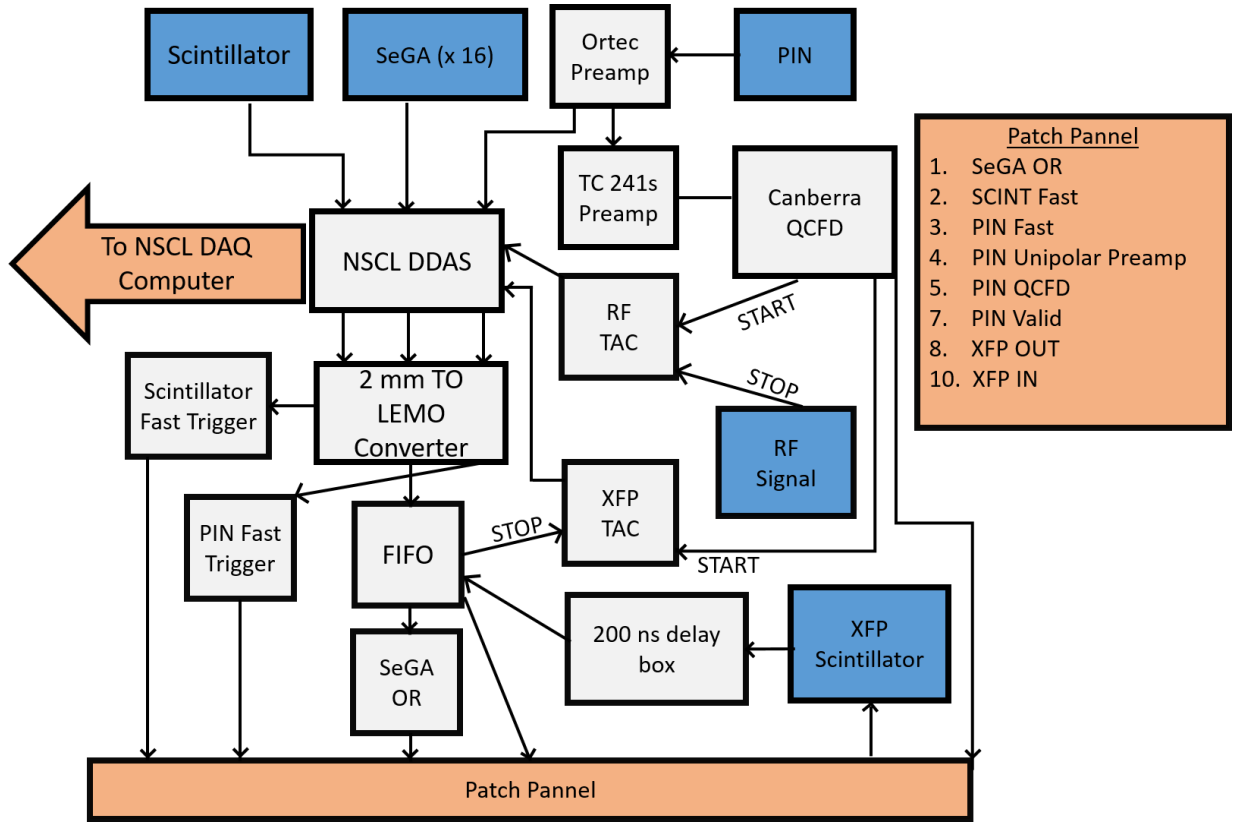
Figure 3.9: Simplified schematic of E14066 electronics. The blue boxes denote the raw input signals taken from the experimental setup as well as the RF signal and XFP scintillator signal taken from the beam operators. The white boxes denote the NIM modules which shape the signals and produce timing signals which are input into DDAS. The orange denotes the output of data to either the NSCL DAQ computer or the patch panel which ports signals to the NSCL Data-U.

detector can be directly sent to the DDAS module for processing, however, the timing signals need to be filtered before being processed by DDAS which is optimized to process preamplifier pulses. The electronics used in this experiment were relatively simple and are displayed in the electronics diagram (Fig. 3.9).

A description of the modules used in E14066 are as follows:

1. Ortec 142 Preamplifier - Amplifies singal from Si PIN detector.

2. TC 241s Amplifier - The amplifier takes the preamplified signal from the Si PIN detector and shapes it into a unipolar gaussian-like waveform.

56

3. Canberra QCFD - The Quad Constant Fraction Discriminator (QCFD) is used to extract time information from a detector. In the case of E14066 the input signal comes from the TC 241s preamp with input from the Si PIN detector. The signal is split into two signals where one is then inverted, attenuated, and delayed. The two signals are then recombined to create a bipolar wave and the point where the signals sum to zero is taken as the pulse time.

4. Time Amplitude Converter (TAC) - The TAC takes two input signals, which are considered the start and stop timing signal. The difference in the start and stop times of the signals are converted into a voltage pulse with amplitude proportional to the start-stop time.

5. Delay Box - The delay box is a box with a very long length of wire which serves to delay the time for a signal to reach its destination.

6. 2mm To LEMO Converter - The standard 2mm cables used for the NSCL DDAS are not compatible with the output to the patch panel and require a converter to LEMO cables.

7. Fast Trigger - A module which produces a logic signal when a threshold is met by the input signal.

8. Fan In Fan Out FIFO - This module is capable of taking in many signal inputs and outputting to many sources.

9. TTL to NIM - The module translates the TTL logic signal (positive square wave) from the fast triggers and SeGA OR into NIM signals (negative fast pulse).

3.1.4 Data Procedure

In principle each detector channel in the SeGA array will output the same value for a given energy input. However, over time the output values may *drift* slightly and this is known as gain drift. In order to protect against gain drifts, a new run is started every hour so that each run can account for these drifts over time in the energy calibration procedure. It is also practical to start new data runs regularly, minimizing the amount of data lost due to crashes of Readout, which stores DDAS signals in a buffer.

A majority of the analysis was done offline by converting the evt files output by Readout into ROOT files which store the time and area of each signal within an event in a tree structure. These trees can be efficiently looped over to sort the data into different spectra that are used for analysis.

3.1.4.1 Data Reduction

For experiment E14066 we have two methods to reduce the amount of background in our data. Each signal stored in an event might be detected in coincidence with the other signals. Since we are looking to detect γ-rays following β-decays we may only want to look at γ-rays which correlate with β-decay energies in the scintillator. By gating on events with these low β-decay energies in the scintillator we can produce a β-delayed γ-ray spectrum. From figure 3.7 a reasonable gate can be placed below 10000 ADC channels to encompass a majority of low-energy scintillator events. By doing this we reduce γ-ray signals unrelated to β-decay events by a factor of 2 in the γ-ray spectrum and eliminate peaks which are produced by natural sources of γ radiation (Fig. 3.10).

In addition to gating on β decays in the scintillator, we can also gate on the time difference between a signal in the scintillator and a signal in a germanium detector. In a β-delayed
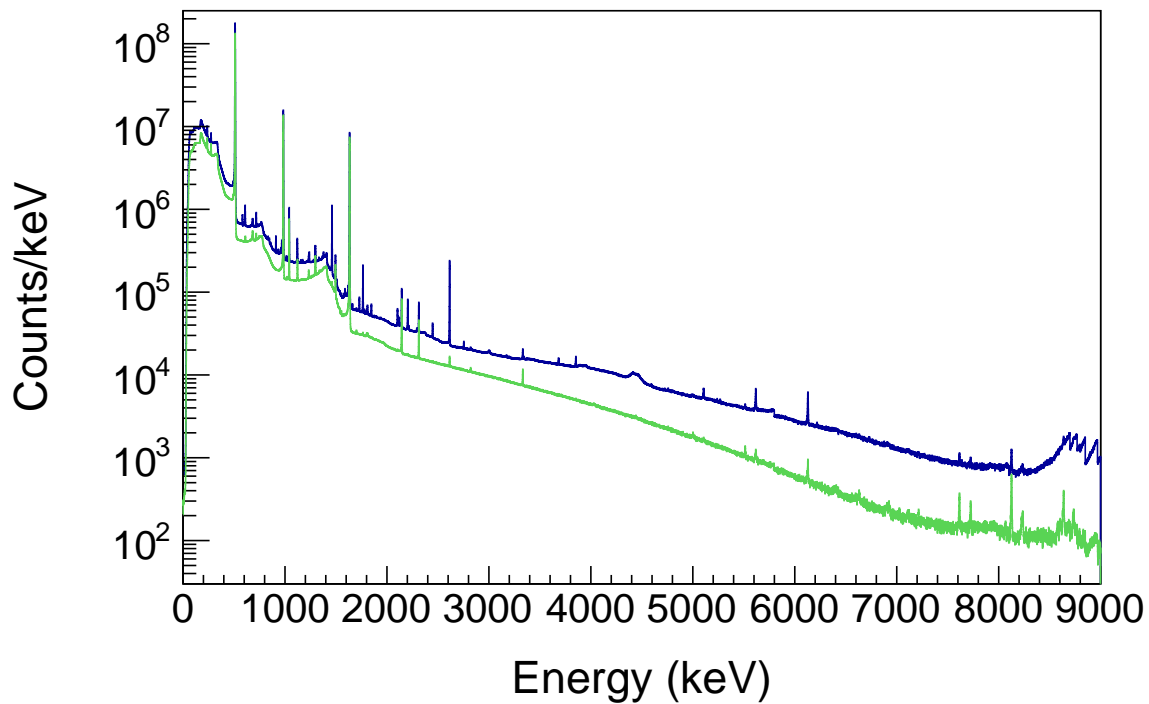
Figure 3.10: The blue line shows a total γ-ray spectrum without gating on the low energy portion of the scintillator. By gating on the β decay energies we reduce the noise in our γ spectrum (green) by a factor of 2 and remove many of the background γ-ray peaks caused by nuclear reactions as well as natural sources of radiation.
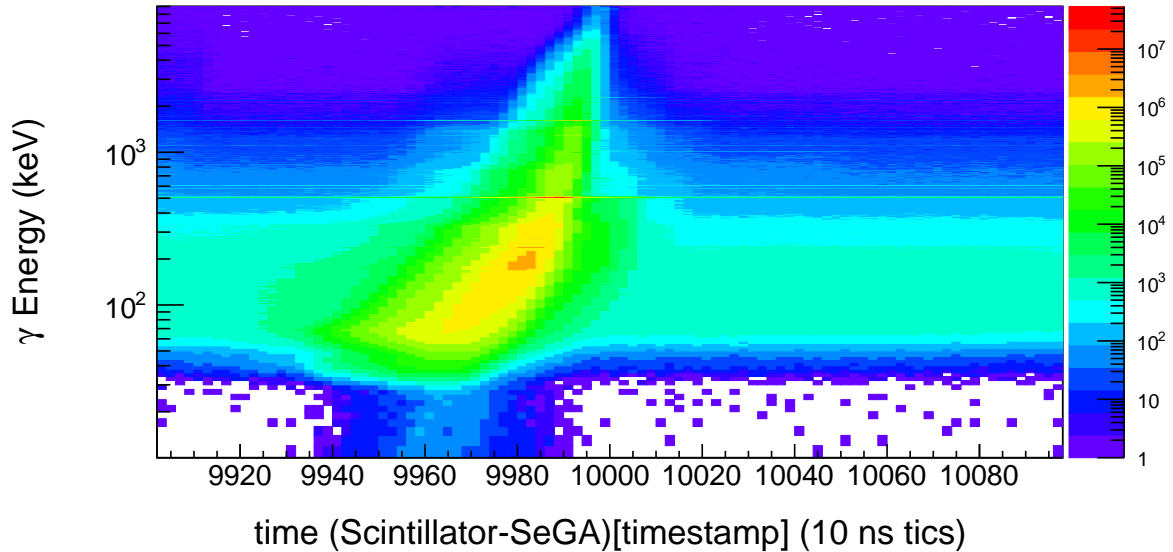
Figure 3.11: SeGA γ-ray energies vs time produced by subtracting the timestamp of a germanium detector signal from the timestamp of the scintillator signal. The X axis values are offset by adding 10000. Each clock tic on the DDAS crate represents 10 ns and is the smallest increment of time which can be used.

γ-ray event the signal from the scintillator will be produced before the signal in a germanium detector. By only accepting events where these signals are detected by DDAS in the correct order we can also reduce the random noise produced by an accidental coincidence in the plastic scintillator concurrent with γ-rays. A timing spectrum produced by subtracting these two quantities shows a very clear peak on β-delayed γ events (Fig. 3.11). A timing gate is placed on channels 9940 to 10010. This reduces a small amount of background, however, most of the background is reduced by gating on the low energy portion of the scintillator. The peak is asymmetric due to a phenomenon called *time-walk* which causes the time signals between the scintillator and SeGA detectors to increase for low energy γ-rays. The pulse shape from the detection of γ-rays is filtered by the digital CFD in DDAS. The lower energy γ-ray pulses result in the timing signal, picked off by the digital filter, to be detected later and follows an exponential trend as a function of energy.

60
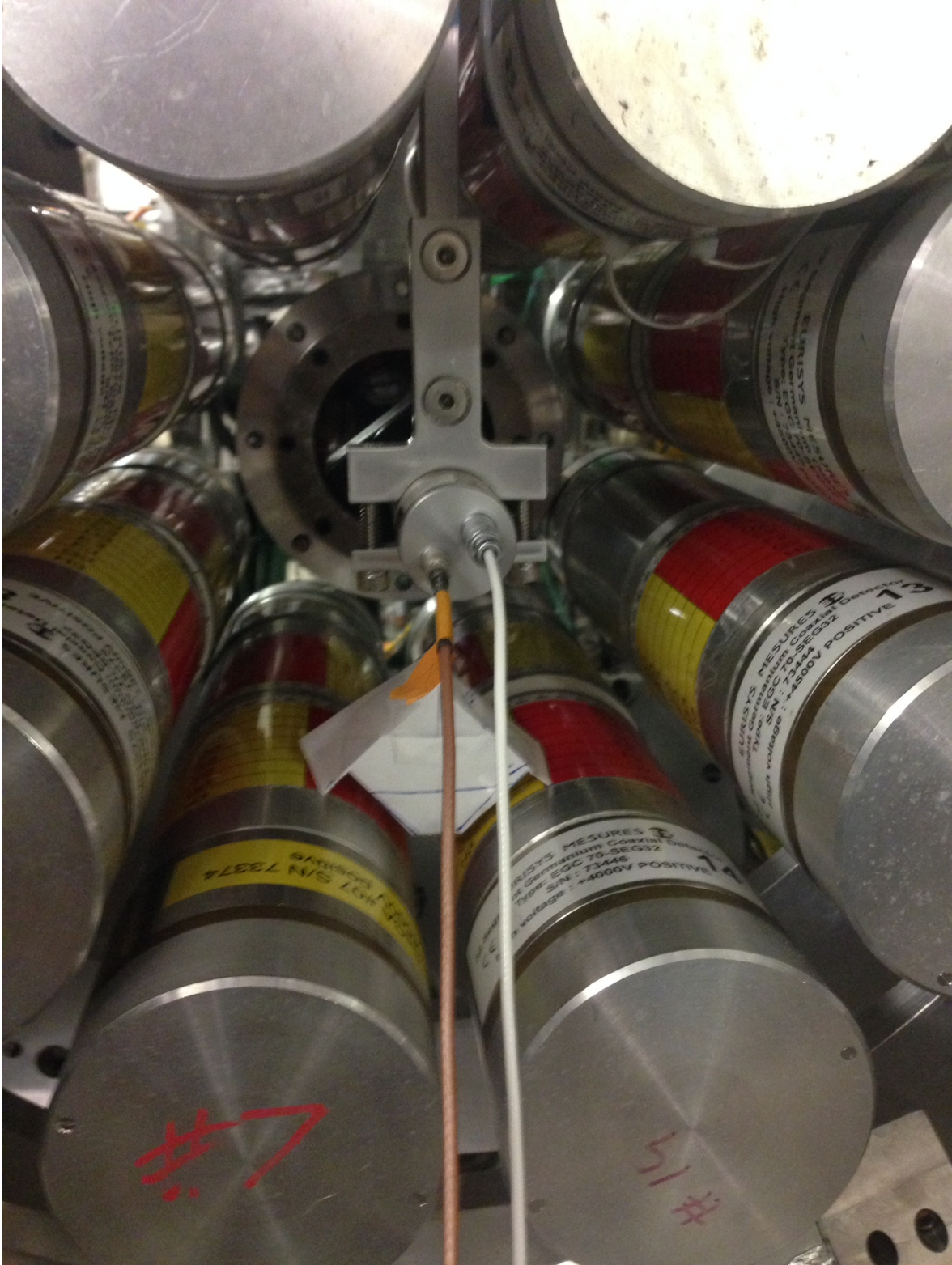
Figure 3.12: A paper holder was made with a small pocket for the ^{125}Sb calibration source and the holder fit over the face of the plastic scintillator to mimic as closely as possible the efficiency from beam particles implanted into the plastic scintillator. During calibration runs the holder was placed on the face of the scintillator.

Following the experiment, data runs were taken with the beam off to measure background from long lived beam contaminants as well as natural background γ-ray sources. An absolutely calibrated mixed source of ^{125}Sb ($T_{1/2} = 1008(2)$ days), ^{154}Eu ($T_{1/2} = 3141(12)$ days), and ^{155}Eu ($T_{1/2} = 1738(4)$ days) was used following the background runs to measure the efficiency of SeGA for our experimental setup. The source was created in 1988 and the shorter half-life ^{125}Sb and ^{155}Eu have nearly all decayed away leaving only ^{154}Eu β-delayed γ-rays from 100 - 1600 keV. A paper holder was made with a small pocket for the calibration source which fits over the face of the plastic scintillator to mimic as closely as possible the efficiency from beam particles implanted into the plastic scintillator (Fig. 3.12). The calibration of γ-ray energies and efficiencies are discussed in the next chapter alongside the analysis.

Chapter 4

Indirect study of the $^{19}\text{Ne}(p, \gamma)^{20}\text{Na}$ reaction using $^{20}\text{Mg}(\beta\gamma)^{20}\text{Na}$

4.1 Introduction

As discussed in section 2.3.2, the search for a γ-decay branch from the 2647 keV is required to complement the upper limit which has been placed on the proton branch [35, 40].

4.2 Analysis and Results

A first order γ-ray energy calibration of the SeGA detectors was applied to the pulse area spectra in each run by performing a gain matching using strong room-background lines from the β-decays of ^{40}K and ^{208}Tl which produced γ-ray energies of 1460.851$\pm$0.006 keV [54] and 2614.511$\pm$0.010 keV [55], respectively. Peaks were fit using an exponentially modified gaussian function (Eq. 4.2) added to a local background model (usually a linear function) to determine the centroids. A cumulative spectrum incorporating all 16 SeGA detectors was generated by applying a coincidence gate in the timing spectrum between SeGA and scintillator events in order to select the γ-rays originating from a β-decay event (Fig. 4.2). By applying this timing gate we were able to compare the ratio of photopeak counts in the ungated spectrum to the counts in the gated spectrum. This yielded a consistant ungated
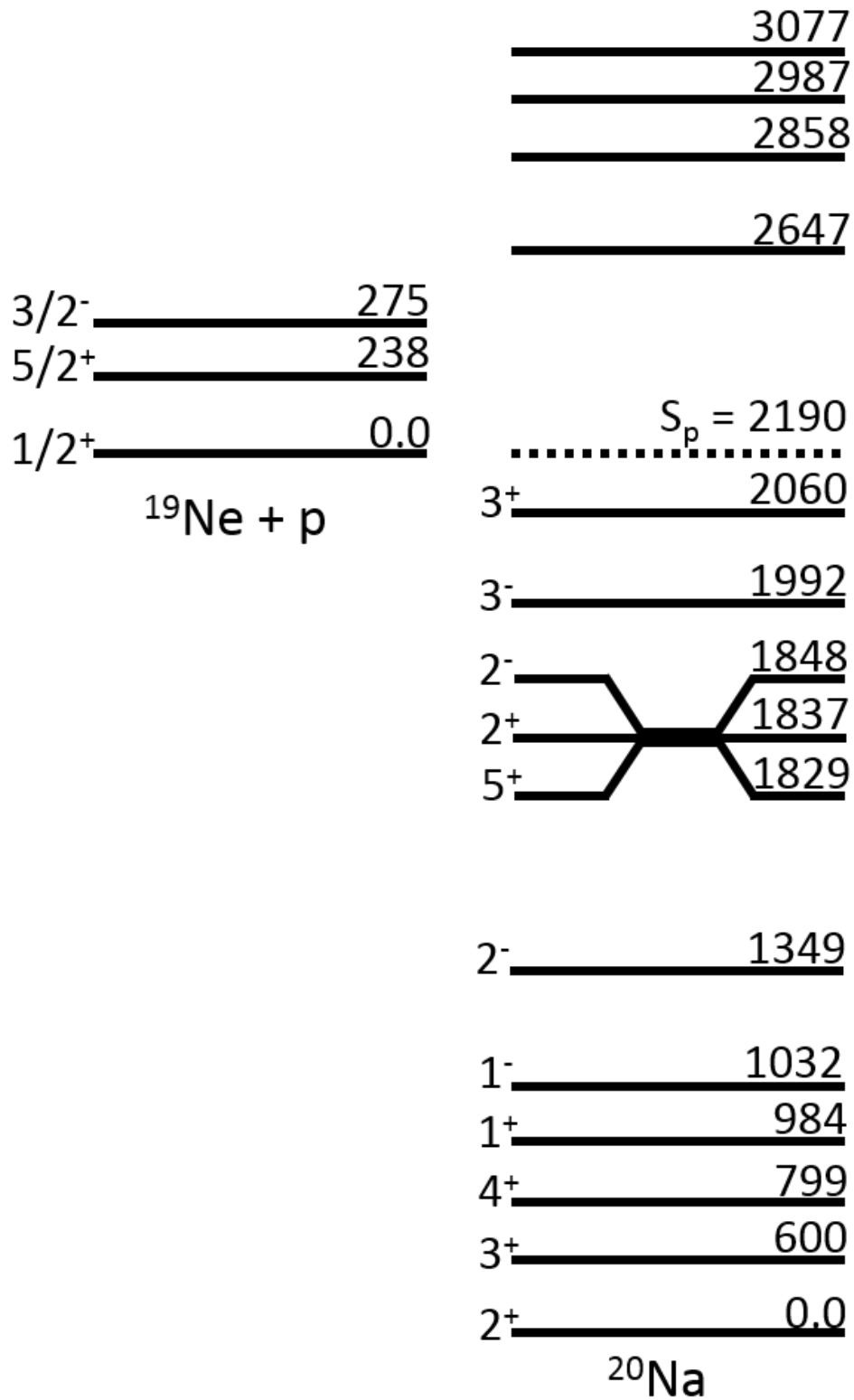
Figure 4.1: Relevant low-lying states in ^{19}Ne and ^{20}Na labeled with J^{π} and energy in keV. Energies below the proton threshold in ^{20}Na as well as J^{π} are adopted from Seweryniak *et al.* [52] and energies above the proton threshold are from Wallace *et al.* [53].
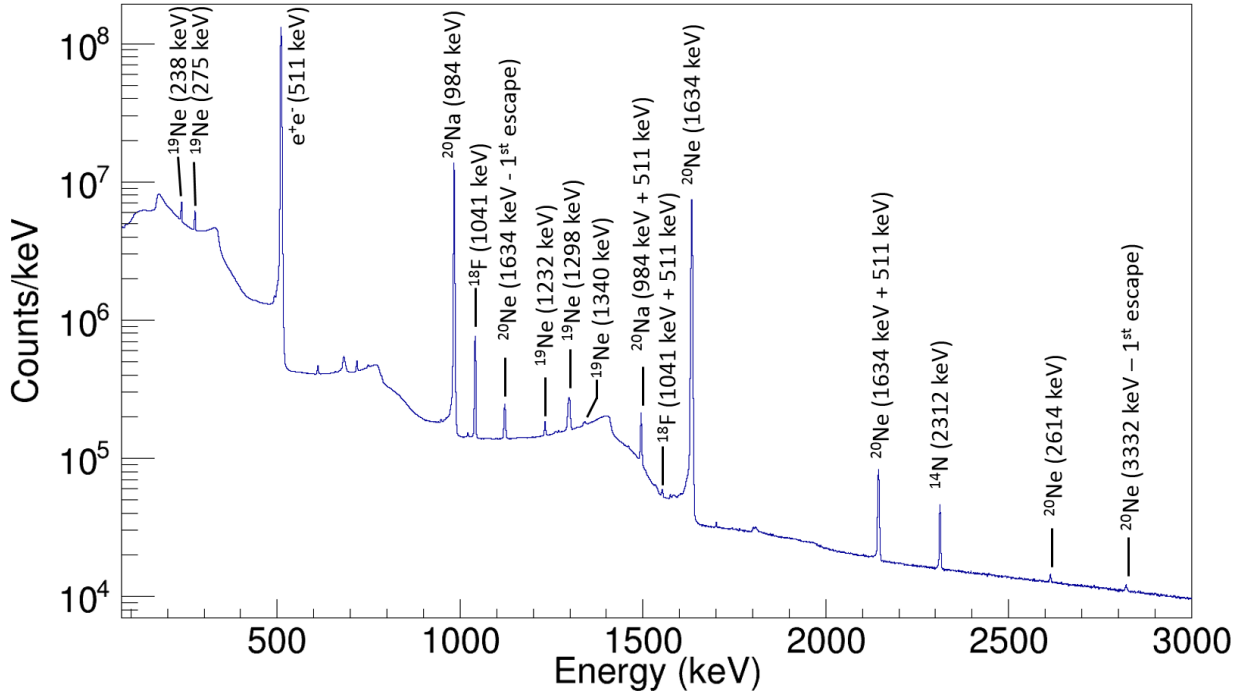
Figure 4.2: Cumulative spectrum of ^{20}Mg β-delayed γ-rays acquired by SeGA, in coincidence with β-decay events in the plastic scintillator.

to gated ratio of 0.90(1) for ^{20}Na and ^{20}Ne peaks over a broad energy range representing the constant efficiency of the scintillator to detect β particles from ^{20}Mg β-decay. Further energy calibration was applied to the cumulative spectrum [56] to account for second order effects, which refined the calibration by less than 1 keV.

The photopeak γ-ray detection efficiency of SeGA, up to 1596 keV, was measured using an absolutely calibrated ^{154}Eu source placed in the center of the front face of the plastic scintillator (Fig. 4.4). The total number of ^{20}Mg ions implanted into the scintillator ($N_{^{20}Mg}$) was calculated indirectly using the number of counts in the 984 keV transition peak, the known ^{20}Mg β-delayed γ-decay intensity of the 984 keV transition in ^{20}Na of 0.697$\pm$0.012 [42] (recently confirmed in [44]) and the efficiency at this energy, which was determined to be $\mathcal{E}_{984}$= 0.0653$\pm$0.0025 by interpolating the efficiency data from the calibration source.

A GEANT4 Monte Carlo simulation was used to model the experimental setup and sim-
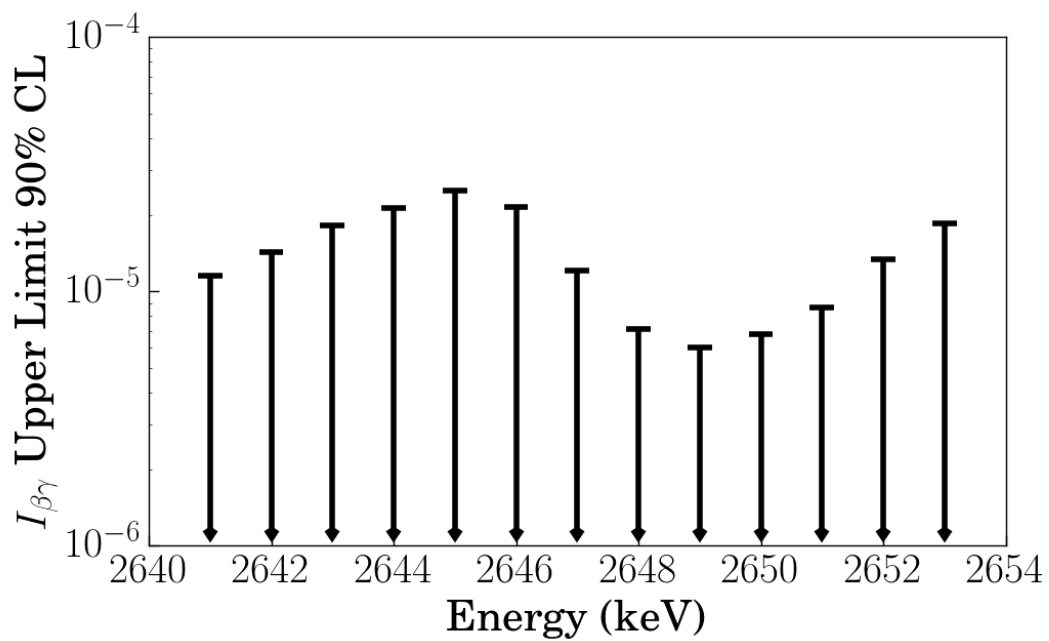
Figure 4.3: Measured 90% C.L. upper limits on the intensity of ^{20}Mg β delayed γ-rays as a function of energy in the 2647 keV search region. The most conservative limit is at 2645 keV.

ulate an independent efficiency curve [57]. In order to match our experimental conditions, monoenergetic γ-rays were emitted isotropically from the center of the scintillator and interacted with the surrounding SeGA array to produce a gamma ray spectrum. The photopeak efficiency was extracted from the generated spectrum and this procedure was repeated over a wide range of energies from 0 to 8 MeV for comparison with the experimental data. Comparison of GEANT4 simulations of γ-rays emitted from the center of the scintillator versus the front face of the scintillator showed a negligible difference in total photopeak efficiency due to the $\approx$1 cm difference in calibration source position and online source position, allowing us to treat our calibration source data without any correction for source position.

The discrete GEANT4 efficiency curve was interpolated with a continuous function of the form (Eq. 4.1)

$$\ln(\mathcal{E}) = \sum_{i=0}^{i=5} C_i (\ln(E))^i \tag{4.1}$$

and compared to the calibration data (Fig. 4.4). The ratio of the GEANT4 simulation efficiencies to the efficiencies from calibration data show that we can scale the GEANT4 simulation by a constant normalization factor of 0.975 to fall in line with the data. We therefore used the scaled functional form representing the GEANT4 simulation to interpolate and extrapolate the efficiency continuously as a function of energy. The systematic uncertainty associated with extrapolating was estimated to be $\leq$5% for γ-ray energies < 2.7 MeV [58]. Statistical uncertainties associated with the calibration data were obtained from the exponentially modified Gaussian fits. Systematic uncertainties associated with the source were calculated from uncertainties in the branching ratios and were determined to be $\leq$1%. A simulation was run in GEANT4 to account for the loss of photopeak counts due to γ-γ summing effects which resulted in a 2% systematic uncertainty at all energies. All uncertainties were combined in
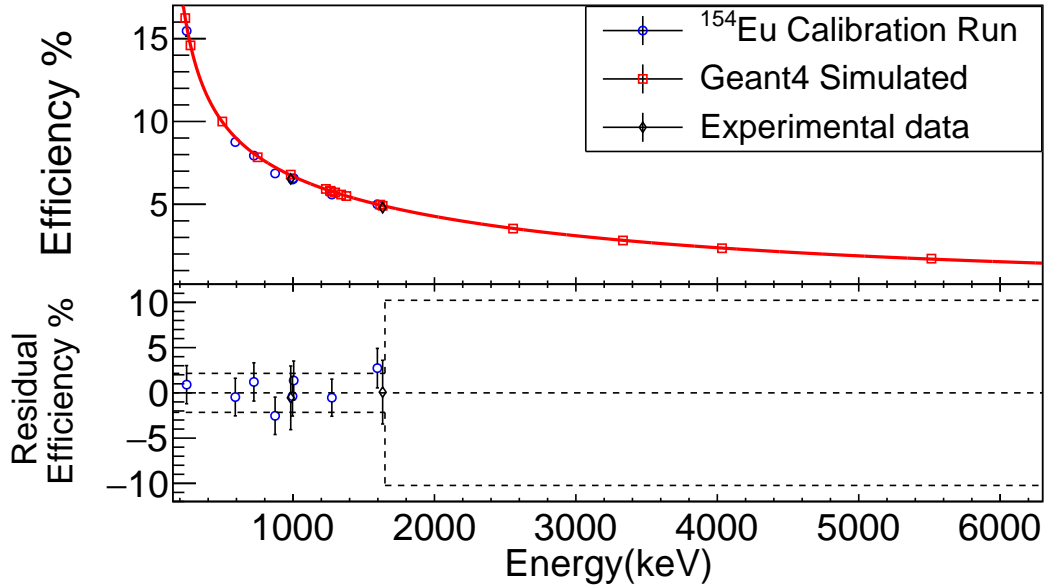
Figure 4.4: Upper panel: Photopeak efficiency of SeGA as a function of energy. Circles correspond to efficiencies from the Eu calibration source. Squares correspond to efficiencies from a GEANT4 simulation of the experimental setup. Fit function (4.1) was used to model the GEANT4 simulation efficiency. The fit was then scaled by a constant factor to line up with the source calibration efficiency (red line). Lower panel: The residual efficiency is the relative difference between the calibration source data and the scaled fit of GEANT4 simulation efficiencies.

quadrature to determine a total efficiency uncertainty for each γ-ray line from the source.

4.2.1   Analysis

In order to measure the feeding of the 2647-keV ^{20}Na state, we searched for γ-ray lines in the SeGA spectra corresponding to all possible primary branches by applying exponentially modified Gaussian fits of the form

$$f(x; N, \mu, \sigma, \lambda) \quad = \quad \frac{N\sigma}{\lambda}\sqrt{\frac{\pi}{2}}exp\left(\frac{1}{2}\left(\frac{\sigma}{\lambda}\right)^2 \ + \ \frac{x-\mu}{\lambda}\right)erfc\left(\frac{1}{\sqrt{2}}\left(\frac{\sigma}{\lambda} \ + \ \frac{x-\mu}{\sigma}\right)\right) \quad (4.2)$$

to the spectrum and fixing the mean (μ) over a range of energies. Based on well known unbroadened β-delayed γ lines in the spectrum from ^{20}Na and ^{20}Ne [34] we parameterized the line shape using the width of the Gaussian (σ) and exponential decay constant (λ) as a function of energy and interpolated these values to each region of interest. N is defined to be the area below the curve, B is a linear background, and *erfc* is the complementary error function.

We determined the intensity of each ^{20}Na γ-ray branch in ^{20}Mg β-decay, using the number of counts in the photopeak N_E at γ-ray energy E, the photopeak efficiency of SeGA at energy E, $\mathcal{E}_E$, and the number of ^{20}Mg ions implanted into the plastic scintillator, $N_{20_{Mg}}$, as input to the following equation:

$$I_{\beta\gamma}^E = \frac{N_E}{\mathcal{E}_E N_{20_{Mg}}} \tag{4.3}$$

4.2.2   Results

No significant γ-ray peaks were observed to correspond with the eleven possible transition energies deexciting the 2647-keV state of ^{20}Na. The upper limit on $I_{\beta\gamma}$ for all but three branches was determined by a single exponentially modified Gaussian (Eq. 4.2) with linear background fit over a range of energies (Fig. 4.5). For two of the other three branches a Gaussian + linear function was used to represent the background (Fig. 4.6) because of a narrow background peak near the search region. Searching for the peak at 1298 keV was complicated by the fact that it lies at nearly the same energy as a Doppler-broadened ^{19}Ne peak [29]. In this special case a Monte Carlo method was used (see section 5.2.2) to fit the Doppler-broadened ^{19}Ne peak using known proton intensities and energies [42, 44]. In
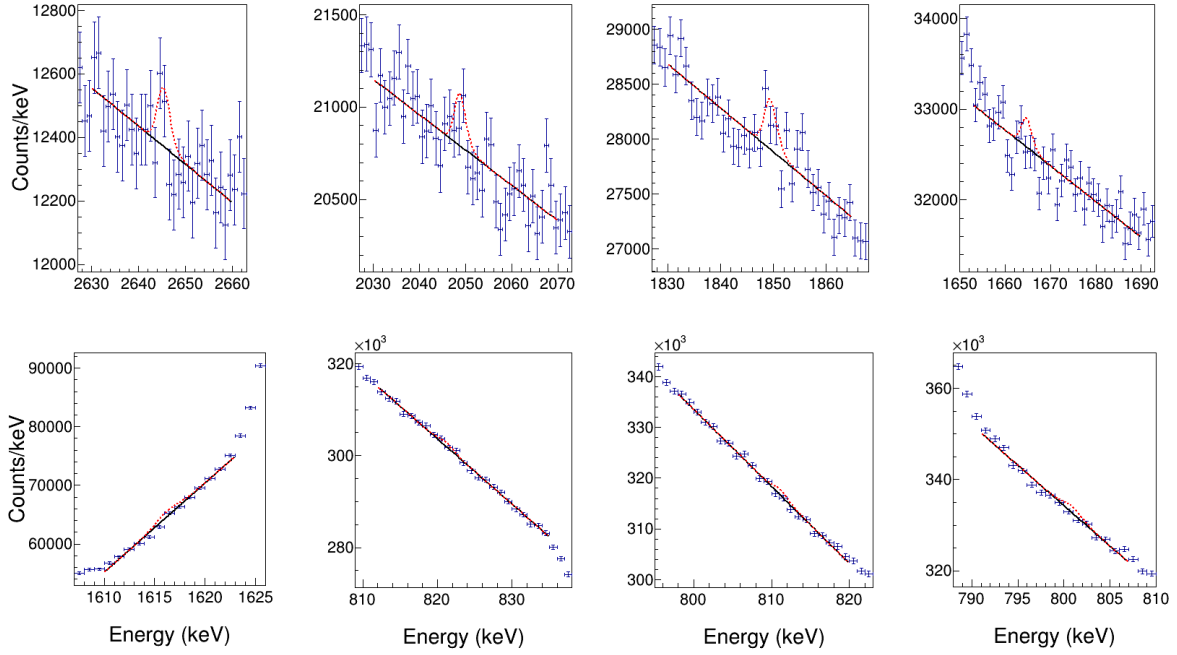
Figure 4.5: Each panel shows a magnified region of the spectrum of ^{20}Mg β-delayed γ-rays acquired by SeGA, in coincidence with β-decay events in the plastic scintillator (Fig. 4.2). The regions of interest are determined by the possible transition energies from the 2647-keV state in ^{20}Na (Table 4.1). The blue points represent the data with statistical error bars and the black lines a linear fit of the background. The red dotted lines represent the background fit plus the 90% confidence upper limits for each possible transition energy. For each transition the fit shown corresponds to the energy within the ± 6 keV search range that yielded the maximum upper limit.

70
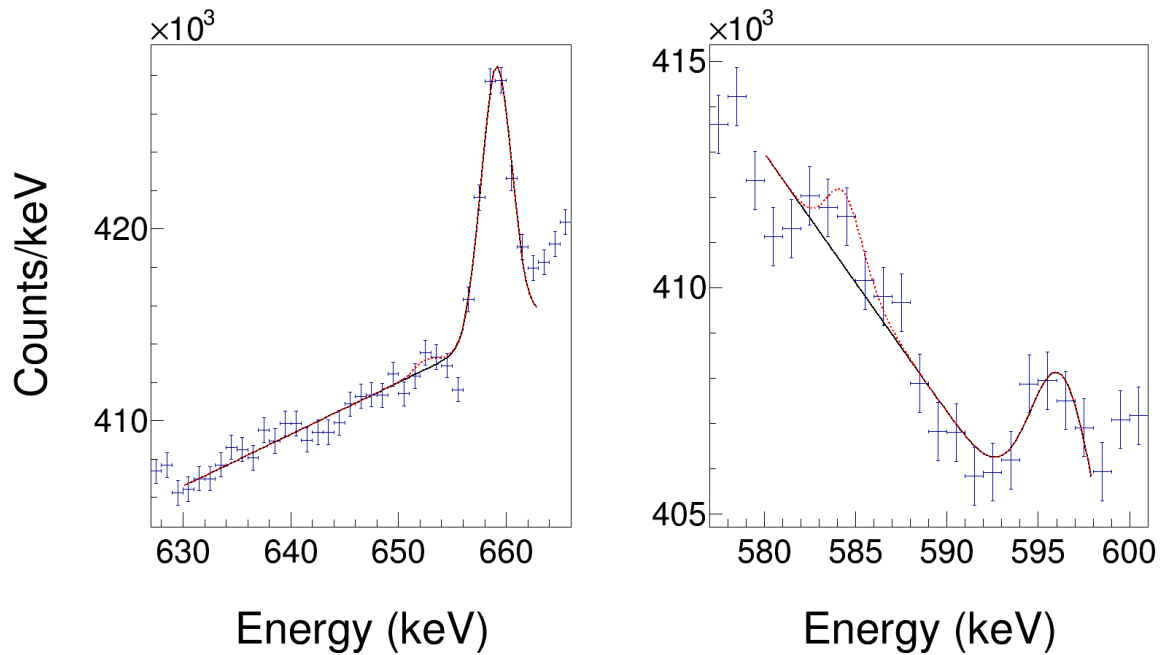
Figure 4.6: Each panel shows a magnified region of the spectrum of ^{20}Mg β-delayed γ-rays acquired by SeGA, in coincidence with β-decay events in the plastic scintillator (Fig. 4.2). The regions of interest are determined by the possible transition energies from the 2647-keV state in ^{20}Na (Table 4.1). The blue points represent the data with statistical error bars and the black lines a linear plus Gaussian fit for the background. The red dotted lines represent the background fit plus the 90% confidence upper limits for each possible transition energy. For each transition the fit shown corresponds to the energy within the ± 6 keV search range that yielded the maximum upper limit.
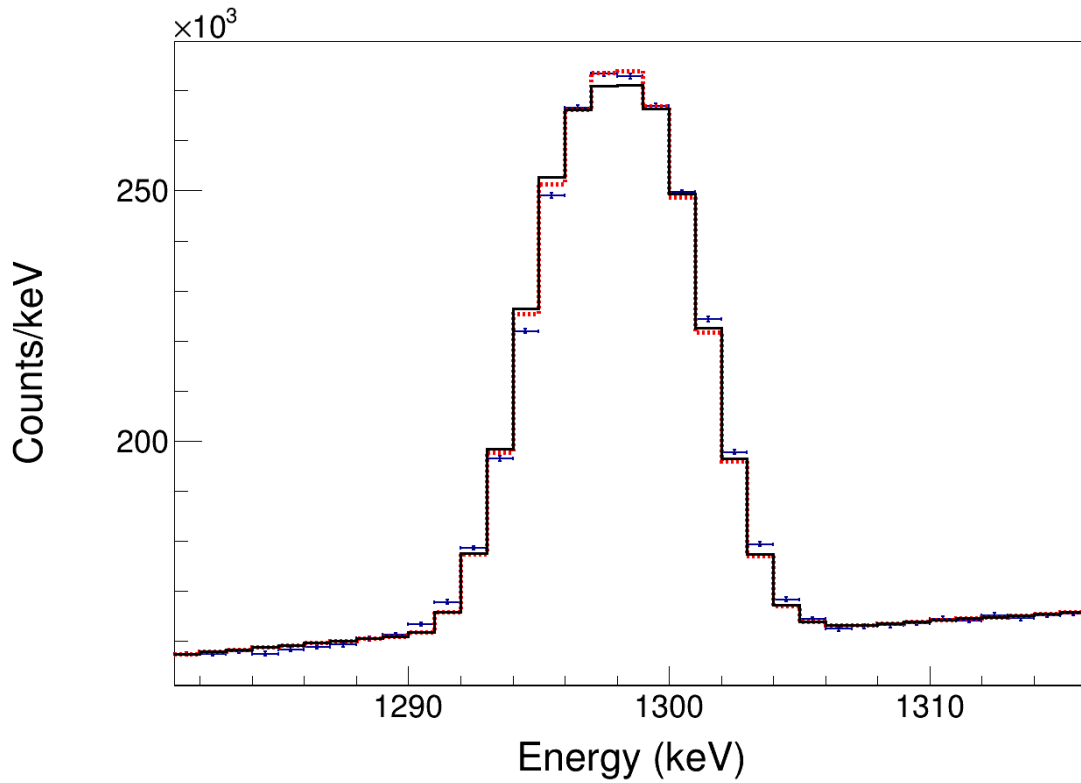
Figure 4.7: A magnified region of the spectrum of ^{20}Mg β-delayed γ-rays acquired by SeGA, in coincidence with β-decay events in the plastic scintillator (Fig. 4.2). The blue points represent the data with statistical error bars. The black line represents the background Monte Carlo plus continuum background model described in the text. The red dotted line represents the background Monte Carlo fit plus the 90% confidence upper limits for the 1298 keV transition energy. The fit shown corresponds to the energy within the ± 6 keV search range that yielded the maximum upper limit.

Table 4.1: Upper limits on the intensities of ^{20}Mg β-delayed γ-ray transitions through the 2647-keV ^{20}Na state with 90% confidence. Final energy level values were adopted from Seweryniak *et al.* [52]. The search for each γ-ray encompassed a range of $\pm$ 6 keV.

^{20}Na γ-ray Transistion (keV)	Transition Energy (keV)	$I_{\beta\gamma}$
$2647 \rightarrow 0$	2647	$< 2.5 \times 10^{-5}$
$2647 \rightarrow 600$	2047	$< 3.7 \times 10^{-5}$
$2647 \rightarrow 799$	1848	$< 5.5 \times 10^{-5}$
$2647 \rightarrow 984$	1663	$< 3.5 \times 10^{-5}$
$2647 \rightarrow 1032$	1615	$< 1.0 \times 10^{-4}$
$2647 \rightarrow 1349$	1298	$< 5.3 \times 10^{-4}$
$2647 \rightarrow 1829$	818	$< 5.6 \times 10^{-5}$
$2647 \rightarrow 1837$	810	$< 6.7 \times 10^{-5}$
$2647 \rightarrow 1848$	799	$< 8.9 \times 10^{-5}$
$2647 \rightarrow 1992$	655	$< 2.7 \times 10^{-5}$
$2647 \rightarrow 2060$	587	$< 8.2 \times 10^{-5}$

the simulation, protons were emitted isotropically from the center of the plastic scintillator and the stopping power was determined by SRIM [59]. The relative proton intensities and energies were fixed, which determined the peak shape, and the overall normalization was left as a free parameter. Due to incomplete charge collection associated with the large peak, we couldn't model the continuum with a simple linear function. Instead we connected two linear functions (to represent the distinct backgrounds on either side of the peak) using a continuous step underneath the Doppler-broadened peak. The Doppler-broadened peak was added to this function and used to model the total background. An unbroadened ^{20}Na peak was searched for on top of the background (Fig. 4.7).

Each individual transition was searched for over a ± 6 keV range about its nominal value to cover any potential inaccuracies in the literature energy of the 2647-keV state. The fitting procedure output the number of counts in the peak and a corresponding uncertainty represented together by a Gaussian probability density function (PDF). The 90% C.L. upper limit on the number of counts was determined by integrating the PDF from zero to 90% of
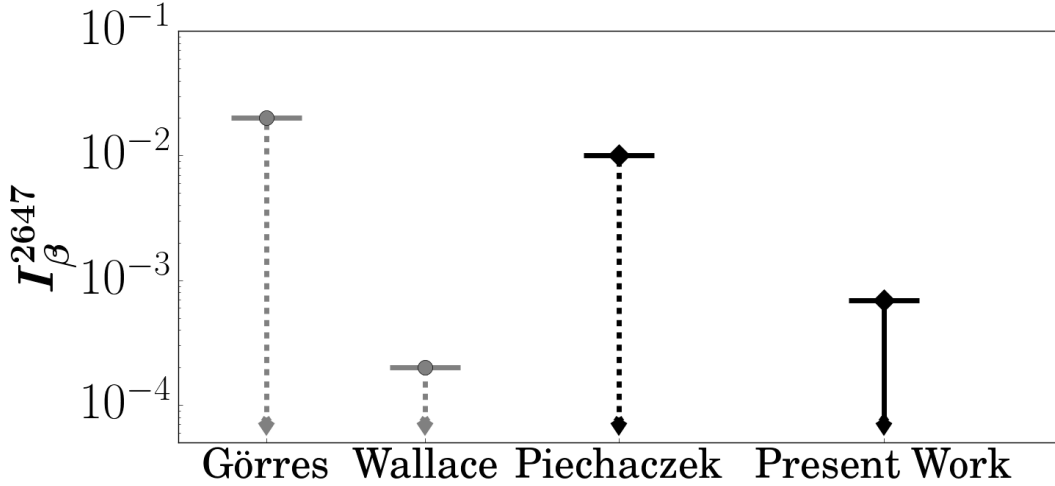
Figure 4.8: Upper limits on the intensity of the ^{20}Mg β-decay transition to the 2647 keV state of ^{20}Na compiled from different sources [41, 42, 35]. All of the upper limits from previous work (dashed lines) are incomplete. The upper limits in grey include only the proton branch to the ground state of ^{19}Ne. The upper limit by Piechaczek includes the proton branch to the ground state and selected γ-ray branches. The present work includes proton branches to the g.s. and 1$^{\text{st}}$ excited state in ^{19}Ne [35, 40] as well as all energetically possible γ branches in ^{20}Na, making it the only complete limit.

the integral from zero to infinity. By applying Equation (2), the most conservative upper limit on the intensity in the search range was determined for each transition (Table 4.1). For example, Fig. 4.3 shows the intensity upper limits in the search range for the 2647-keV γ-ray.

To find the total upper limit on $I_{\beta\gamma}$, the intensity for each transition was calculated from the central value of the number of counts using Equation (2). The intensities were summed and the uncertainties were added in quadrature to produce a Gaussian PDF representing $I_{\beta\gamma}$. The 90% C.L. upper limit on $I_{\beta\gamma}$ was determined by integrating the PDF from zero to 90% of the integral from zero to infinity. In this procedure, a single value of the excitation energy of the 2647-keV state was used for all transitions. By repeating this procedure over the ± 6 keV search range, the maximum value of the upper limit was found to be $I_{\beta\gamma} < 5.7 \times 10^{-4}$.

The 984 keV peak is the only γ-ray transition from ^{20}Na that is present in the cumulative

spectrum, and we can search for coincident γ-rays in a γ-gated spectrum for transitions from the 2647 keV state. By looking at the γ-gated spectrum we find that there is no evidence for transitions from the 2647 keV state.

Additionally gates were placed on γ-ray energies in search for γ-γ coincident peaks form the 2647 keV state, however no peaks were present in these gated spectra above upper limits determined from the cumulative spectrum.

4.3   Discussion

Wallace *et al.* determined the proton intensity from the 2647 keV state to be $I_{\beta p} < 2 \times 10^{-4}$ [35]. However, this limit did not include the recently detected proton emission to the 1st excited state of ^{19}Ne at 238 keV, which Belarge *et al.* measured to have approximately the same branching ratio as emission to the ground state [40]. The inclusion of this new path leads to $I_{\beta p} < 4 \times 10^{-4}$. The underlying PDF representing $I_{\beta p}$ was not documented in Wallace *et al.* so we assume that their uncertainties were also dominated by statistics and that they followed a procedure similar to ours. Adding their limit on $I_{\beta p}$ with our limit on $I_{\beta\gamma}$ in quadrature has yielded the first complete experimental limit of $I_\beta < 6.9 \times 10^{-4}$ and log $ft > 6.4$ for the ^{20}Mg β^+ decay transition to the 2647-keV ^{20}Na state.

Table 4.2:   Gamow-Teller strengths B(GT) and associated log ft values calculated for ^{20}Mg β-decay to 1st and 2nd excited 1^+ states in ^{20}Na using the sd shell model with various interactions described in the text.

Interaction	B(GT) 1_1^+	log ft 1_1^+	B(GT) 1_2^+	log ft 1_2^+
USD	0.366	4.03	0.994	3.59
USDA	0.431	3.96	0.494	3.89
USDB	0.460	3.93	0.621	3.80
USDB-EDF	0.446	3.94	0.587	3.82
IMSRG	0.828	3.67	0.377	4.01

For comparison to the experimental limit, we calculated theoretical values of log ft for the transition to the unbound 2nd 1^+ state of interest as well as the bound 984 keV 1^+ state utilizing the sd shell model with harmonic oscillator radial wave functions and a quenching of 0.6 [60] (Tab. 4.2). In order to assess the uncertainty in this calculation, a variety of interactions were used including USD [61], USDA [62], USDB [62], USDB-EDF, and IMSRG [63, 64, 65]. The USDB-EDF calculation was used to assess the uncertainties associated with the radial wave functions for the loosely-bound states involved and the EDF part was obtained with the Skx Skyrme functional [66]. All calculated log ft values for the bound 984 keV state were in the range $3.67 - 4.03$. This agrees with the measured values of 3.87 [67] and 3.83 ± 0.02 [42]. Similarly, the range of values we expect for the transition to the 2nd excited 1^+ state in ^{20}Na is $3.59 - 4.01$, much lower than the lower limit placed on the log ft. Therefore, the 2647-keV state does not correspond to the 1^+ state from the shell model. In fact, the 2647 keV state is likely not any 1^+ state because configuration mixing should result in smaller log ft values than observed even for an intruder 1^+ state.

Considering a 3^+ assignment, the log ft values of second forbidden $\Delta J = 3$ β-decay transitions in the mass region $9 < A < 27$ are all greater than 14 [68]. Our limit of log $ft > 6.4$ for the transition from $J^\pi = 0^+$ ^{20}Mg to the 2647 keV state is, therefore, consistent with a 3^+ assignment; however, this does not exclude other possibilities for the J^π assignment.

The 2987 keV ^{20}Na state is most likely the analog of the 1^+ ^{20}F state at 3488 keV [33, 53]. log ft values of 4.08(6) and 4.07(3) were measured in the previous work for the feeding of this ^{20}Na state [42, 44], which is essentially consistent with the range $3.59 - 4.01$ predicted by our shell model calculations for the 2nd 1^+ state.

4.4   Conclusion

An intense source of ^{20}Mg and a γ-ray spectrometer with high resolution and efficiency were used to search for population of the 2647 keV state in ^{20}Na via β-decay. For the first time, all possible γ-ray branches from this state were limited in order to complement previous searches for the proton branch. An upper limit on the β delayed γ decay intensity was measured completing the limit on the log ft value. The combined results from the present ^{20}Mg($\beta\gamma$) experiment and past ^{20}Mg(βp) [35] and ^{19}Ne(d, n)^{20}Na experiments [40] make an assignment of 1^+ highly unlikely, in agreement with recent work. This result is consistent with the concurrent direct measurement [47].

Chapter 5

Toward the $^{15}\text{O}(\alpha, \gamma)^{19}\text{Ne}$ Reaction Rate using Doppler Broadening in $^{20}\text{Mg}(\beta p \gamma)^{19}\text{Ne}$

5.1 Doppler Broadening Line Shape Analysis Technique

The analysis of β-delayed nucleon emission has traditionally relied on the direct detection of the emitted nucleons to measure important nuclear properties such as excited state lifetimes, excited state transition energies, feeding intensities, and excited state spin-parity. However, a technique measuring just the line-shape of γ-rays following nucleon emission can provide information on all of these quantities.

Doppler shifts occur when a γ-ray is emitted from a recoiling nucleus following particle emission from a nucleus initially at rest. One such example is β-delayed proton emission to an excited state daughter (Equation 5.1) where Q, R, and S represent different isotopes, A represents the number of nucleons, and Z the number of protons in a nucleus.

$$Q_Z^A \to R_{Z-1}^{*A} \to S_{Z-2}^{*A-1} \tag{5.1}$$

Due to conservation of momentum (Eq. 5.2) the daughter nucleus, S, will recoil with

equal and opposite momentum from the emitted nucleon. The center of mass energy, determined by the conservation of momentum, is calculated using (Eq. 5.3). This implies the daughter, S, carries m_p/m_S of the center of mass energy. The recoiling daughter nucleus will, therefore, preserve information about the energy of the emitted nucleon which can be used to determine which excited state the parent nucleus, R^*, was in.

$$m_S v_S = -m_p v_p \tag{5.2}$$

$$E_{CM} = \frac{1}{2} m_S v_S^2 + \frac{1}{2} m_p v_p^2 \tag{5.3}$$

An ensemble of such events will give rise to a broadened peak shape. The Doppler Broadening technique utilizes the information about the shape of the γ peak to reconstruct information about the daughter and parent nucleus. The recoil from nucleon emission and the resulting Doppler-shifted γ-rays will contain information about the energy of the emitted nucleon. The emitted nucleon can also cause the γ-ray to be emitted in a preferential direction from the direction of recoil. This can give us information of the excited state spin-parity of the parent and daughter nucleus. Each of these features cause the shape of the resulting peak to be modified from an un-broadened line shape, and a reconstruction of the peak from simulations can be used to extract these quantities.

5.1.1 Monte Carlo Simulation of broadened ^{19}Ne γ lines

The Monte Carlo simulation of a γ peak should take into account the information from the parent nuclei in addition to information about the experimental setup. Inputs of the

simulation for this particular experiment include the Center of Mass (CoM) energy between the emitted proton and ^{19}Ne* state (denoting the ^{19}Ne in an excited state), the lifetime and excitation energy of the ^{19}Ne* state, the stopping power of the implantation material (Polyvinyltoluene), and the response function of each SeGA detector.

5.1.1.1   Treatment of Center of Mass Energy

The recoiling ^{19}Ne* is given an initial kinetic energy based on the CoM energy of the proton emission from an excited ^{20}Na state which is, to a good approximation, at rest in the plastic scintillator following β decay. The Monte Carlo simulation works by first assuming a lifetime for a ^{19}Ne* state and randomly sampling the exponential decay curve distribution.

A state can be fed by multiple excited states and, with enough sensitivity, can allow for the measurement of multiple proton feeding intensities. Alternatively, if there is no information about excited states in the proton emitter an excited state energy can be reproduced in the simulation by iterating the proton energy.

5.1.1.2   Treatment of Excited State Lifetime (τ) and Stopping Power

The excited state lifetime of ^{19}Ne* is invariably linked to how much the nucleus slows down inside the implantation material. The longer the lifetime (τ), the more time the recoiling nucleus has to slow down in the medium.

The uncertainties in lifetime and stopping power are treated as a systematic uncertainties in the simulation for the quantity that is being measured. The lifetime tends to be the less well known quantity of the two in the literature since simulations of stopping power tend to be accurate to within a few %, however it would be possible to measure the stopping power of a material given sufficiently precise measurements of all other inputs into the simulation.

The daughter nucleus, ^{19}Ne, will emit Doppler shifted γ rays at an energy determined from Equation 5.4, where θ is characterized by the angle between the γ-ray and recoiling ^{19}Ne $\vec{v}$.

$$E_\gamma = E_{\gamma o}\sqrt{\frac{1+\beta}{1-\beta}}, \quad \beta = \frac{v \cdot cos(\theta)}{c} \tag{5.4}$$

In a vacuum the daughter nucleus emits a Doppler shifted γ ray with energy dependent on its initial kinetic energy and $cos(\theta)$. However, in order to analyze γ rays from rest in ^{20}Mg$(\beta p\gamma)^{19}$Ne decay with significant intensity, the ^{20}Mg beam must be stopped in a material. The recoiling ^{19}Ne nucleus will slow down in the material due to electronic and nuclear stopping powers.

The stopping power of the material is determined as a function of the speed of the recoil nucleus as well as the properties of the implantation material and can be simulated using SRIM [59] (Fig. 5.1) or LISE++ [69]. We therefore, apply the energy loss recursively over many small time-steps in order to mimic a continuous energy loss.

$$\frac{dE}{dx} = -f_e(v) - f_n(v) \tag{5.5}$$

This is implemented by applying equation 5.5 over many small time-steps, where $\frac{dE}{dx}$ is the energy lost by the recoiling nucleus in the medium and $f_e(v)$ and $f_n(v)$ are the electric and nuclear stopping power terms derived from the material of the medium and the velocity v recoiling nucleus.

The Doppler broadened line shape is most apparent in cases where the excited state of the daughter nucleus B is short lived.
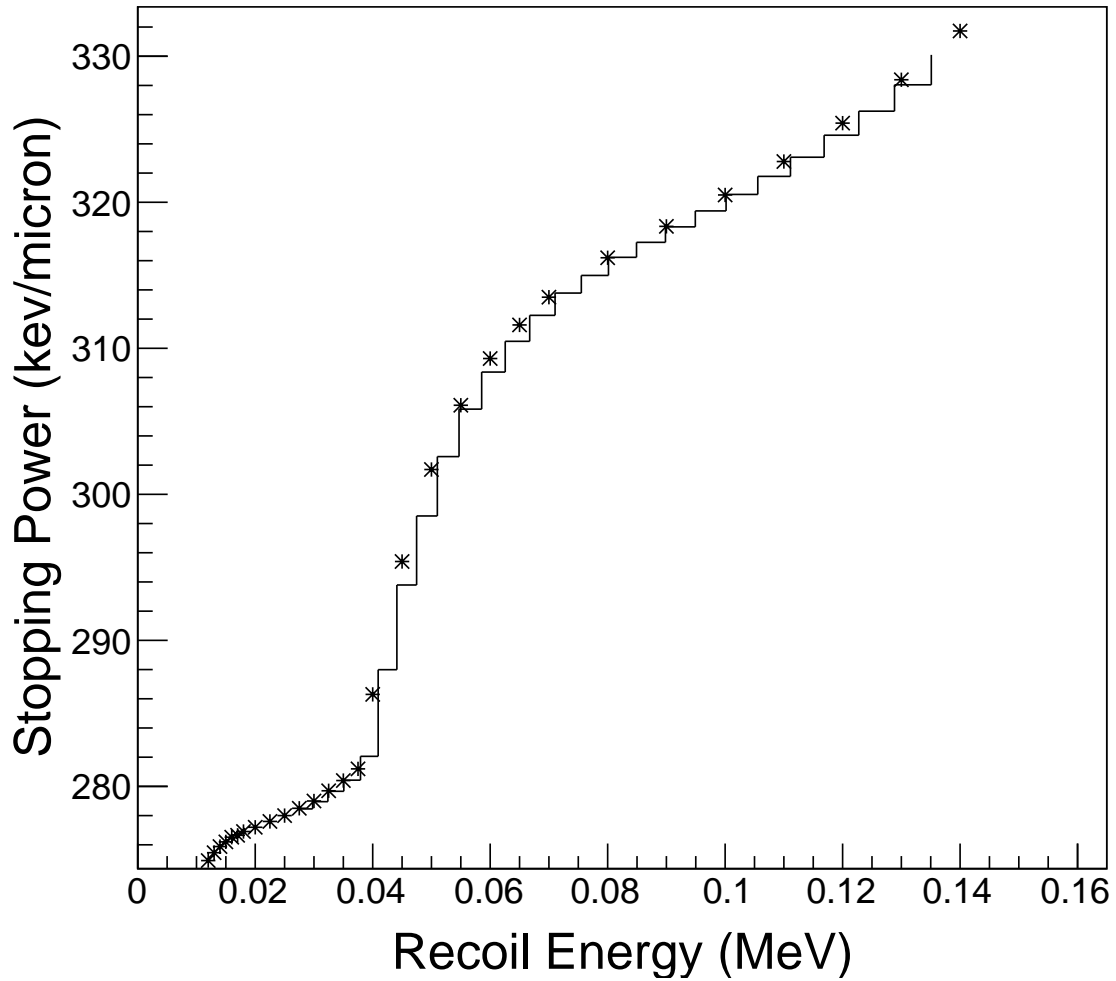
Figure 5.1: The stopping power is treated iteratively over many time steps which are determined by the lifetime of the ^{19}Ne excited state. The stars represent the sum of the electric and nuclear stopping powers of the scintillator at different recoil energies and the line represents each time-step traversed by the algorithm, updating the recoil energy and stopping power continuously.

5.1.1.3 SeGA Detector Response

A γ ray that is detected by a SeGA detector will deposit energy dependent on a response function which is well characterized by an exponentially modified Gaussian (EMG) Eq. 4.2.

Each detector can have different resolution which has the largest effect on the σ parameter in Eq. 4.2. Therefore, we need to characterize this quantity as a function of energy for each SeGA detector in order to properly simulate the ensemble of Doppler-Broadened γ-rays entering our setup.

In order to do this unbroadened β-delayed γ ray peaks were fit over a range of energies to parameterize σ as a function of energy for each detector. β-delayed γ ray peaks were fit using Eq. 4.2 at energies 238 (^{19}Ne), 984 (^{20}Mg), 1634 (^{20}Ne), 2312 (^{14}N), 3332 (^{20}Ne), and 6129 (^{16}O) keV (Eq. 4.2). The exponential parameter (λ) was fixed to 0.7 as this fit the left side tail of the peak well at all energies in all detectors. All other parameters were left free.

The value of σ was plotted as a function of energy and fit using a linear function (Figs. 5.2,5.3,5.4). Each detector has a different contribution to the total number of counts in the peak depending on efficiency and the simulation reflects this by normalizing the number of counts simulated in each detector.
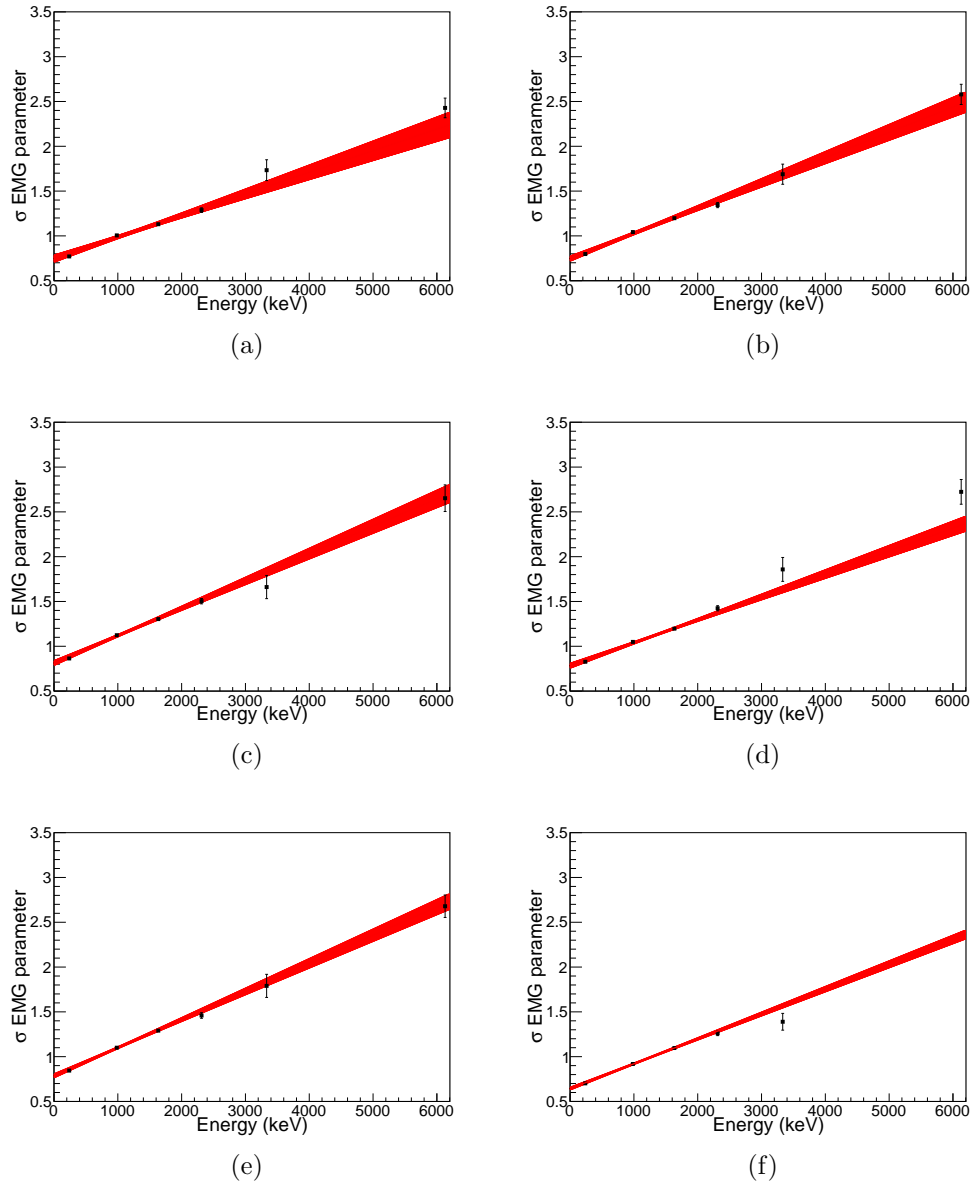
Figure 5.2: The σ parameter energy dependence for input to the exponentially-modified-gaussian response function for each SeGA detector. Each data point corresponds to the value of the σ parameter for a particular calibration peak. The σ parameter is fit using a line and the confidence band [red online] shows 1 standard deviation uncertainty:(a) Detector 1; (b) Detector 2; (c) Detector 3; (d) Detector 4; (c) Detector 5; and (d) Detector 6;

Rather than sampling the γ-ray's final energy from the EMG probability distribution, it is much faster to sample the energy from the normalized cumulative distribution function Eq. 5.6. From Fig. 5.5 we can generate a random number between 0 and 1 to sample the
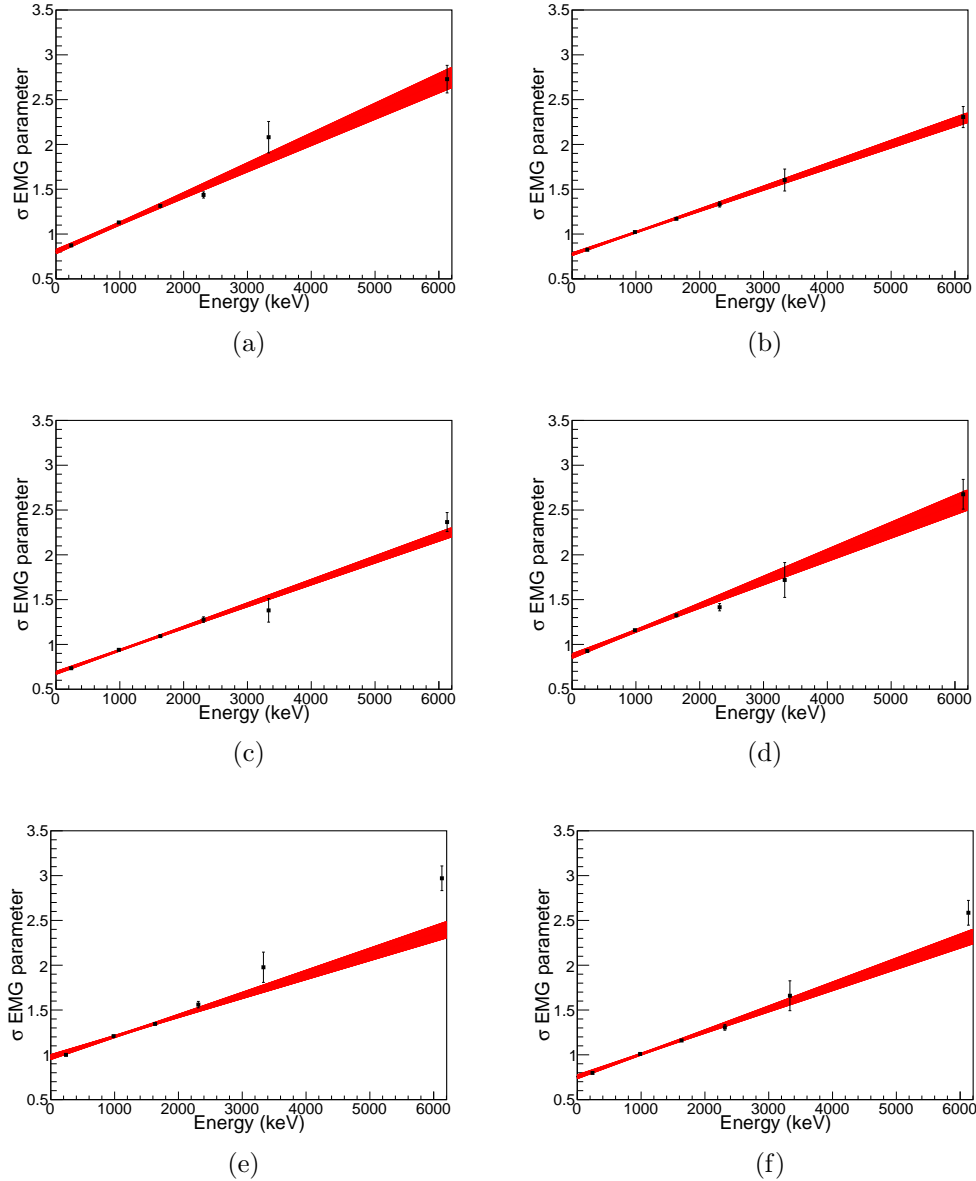
Figure 5.3: The σ parameter energy dependence for input to the exponentially-modified-Gaussian response function for each SeGA detector. Each data point corresponds to the value of the σ parameter for a particular calibration peak. The σ parameter is fit using a line and the confidence band (red online) shows 1 standard deviation uncertainty:(a) Detector 7; (b) Detector 8; (c) Detector 9; (d) Detector 10; (c) Detector 11; and (d) Detector 12;
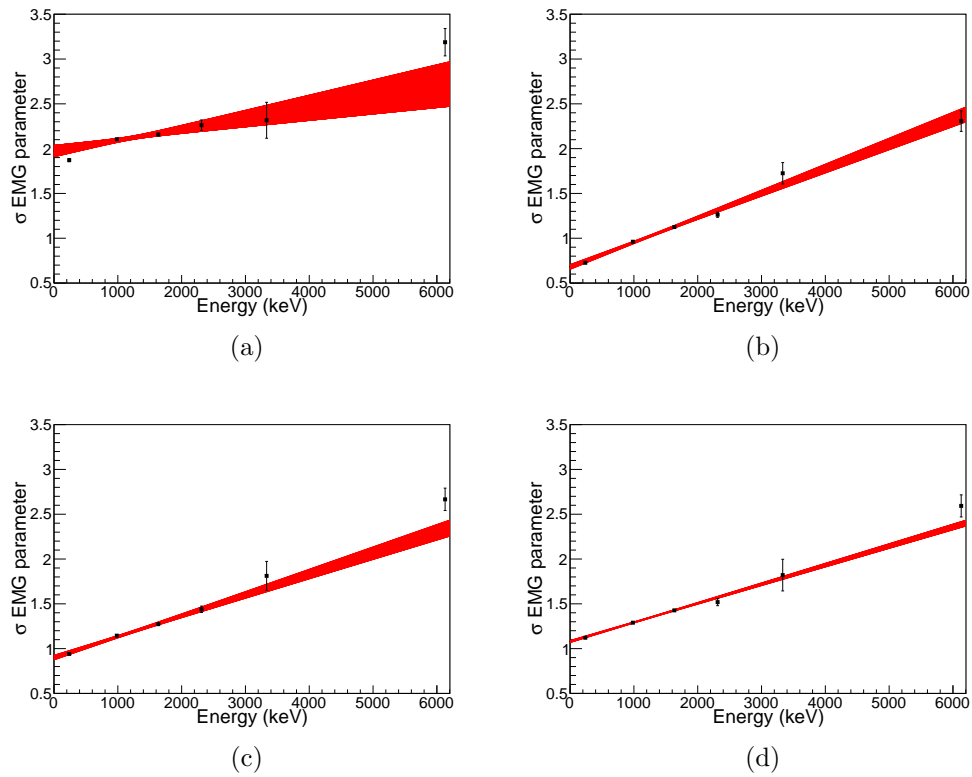
Figure 5.4: The σ parameter energy dependence for input to the exponentially-modified-Gaussian response function for each SeGA detector. Each data point corresponds to the value of the σ parameter for a particular calibration peak. The σ parameter is fit using a line and the confidence band [red online] shows 1 standard deviation uncertainty:(a) Detector 13; (b) Detector 14; (c) Detector 15; and (d) Detector 16;
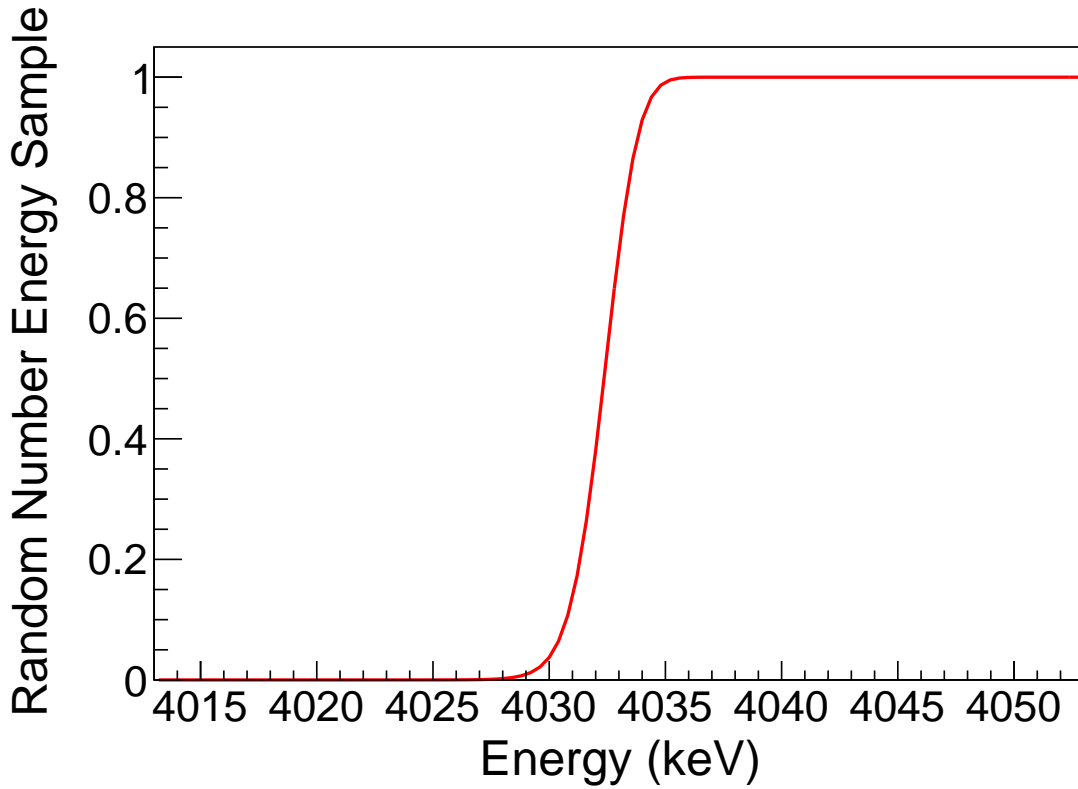
Figure 5.5: Example Cumulative Distribution Function for a 1232 keV γ.

output energy of a SeGA detector.

$$F(x; N, \mu, \sigma_{det}, \lambda = 0.7) = \frac{N}{2}\left(exp\left(\frac{1}{2}\left(\frac{\sigma}{\lambda}\right)^2 + \frac{x - \mu}{\lambda}\right)erfc\left(\frac{1}{\sqrt{2}}\left(\frac{\sigma}{\lambda} + \frac{x - \mu}{\sigma}\right)\right)\right.$$
$$\left. - erfc\left(\frac{x - \mu}{\sqrt{2}\sigma}\right)\right) + 1 \quad (5.6)$$

5.1.1.4 Angular Correlations

Angular correlations between protons and γ rays can have an effect on the overall line-shape [70]. Generally speaking, the direction of the proton may produce a γ-ray angular

distribution described by a linear combination of even Legendre polynomials [71] in the center of mass frame (Eq. 5.7).

$$W(\theta_{cm}) = \sum_{2\kappa} A_\kappa P_\kappa(cos(\theta_{cm})) \tag{5.7}$$

The highest order Legendre polynomial for each γ ray transition is determined by the spin of the proton-emitting ^{20}Na state, multipolarity of the γ ray transition, angular momentum of emitted proton, and spin of ^{19}Ne* [72, 73] such that

$$2\kappa_{max} \leq min[(2j_{20_{Na}}), (2L)_{max}, (2l)_{max}, (2j_{19_{Ne*}} - 1)_{max}]$$

The spin of ^{20}Na states is constrained to be 0^+ and 1^+ in allowed ^{20}Mg β decay, restricting the angular correlation function to the $P_0(cos(\theta_{cm}))$ and $P_2(cos(\theta_{cm}))$ terms. A first order assumption is made that the isotropic term (P_0) dominates and a P_2 term will be added if a good fit can not be achieved with this assumption.

An angle, dependent on the angular distribution function 5.7, is randomly chosen between the recoiling ^{19}Ne atom and emitted γ ray, to calculate the Doppler shift at the observation point. This γ ray enters a random detector and the known response function of that detector is treated as a probability density function which outputs a final observed energy. An ensemble of such events can be used to construct a simulated peak shape for comparison to the actual data.

5.1.1.5 Summary of Monte Carlo Procedure

1. The lifetime τ and the proton energies which feed the excited state γ transition are fixed. In principle these may not be known quantities and multiple simulations are

done over a set of these quantities. The γ-ray energy is also fixed to the mean value of the Doppler Broadened line.

2. The stopping power is determined over a large range of energies so that interpolation can be done to model a continuous energy loss by the recoiling particle. The stopping power of a number of materials can be obtained using SRIM or LISE++.

3. The decay time of each simulated nucleus is sampled from a distribution determined by the fixed statistical lifetime.

4. An initial velocity is prescribed to the recoil nucleus depending on the energy imparted via the emitted proton.

5. The stopping power is continuously sampled over 50 time-steps where the small distance dx the nucleus traveled is calculated from the current velocity of the nucleus and multiplied by the current stopping power ($\frac{dE}{dx}(E)$) to get the energy loss for each $\tau/50$ time-step.

6. After the final velocity is calculated from the previous step, a random projection of the angle $[\cos(\theta)]$ between the emitted photon and direction of the nucleus is chosen to apply a Doppler shift correction to. Because the recoil nucleus is initially at rest there is no preferential direction for the initial velocity in our case. In principle the recoil nucleus can polarize the direction of the emitted γ-ray and this should be taken into account at this step rather than assuming a random $\cos(\theta)$.

7. Finally, a treatment of the SeGA response function is applied to the γ-ray energy.

8. Repeat steps 3-7 to compare an ensemble of events to the data and to reduce statistical noise from the simulation.

5.1.1.6 Treatment of Background

In the case of a γ ray peak with low statistics, it is sufficient to use a linear function to model the background.

The treatment of background from high statistics peaks requires a more complex model. In some cases it is possible to use an error function where the slope on the left side of the peak is similar to the slope on the right side of the peak, but this is not always the case. Instead a more general model is used to fit the background where the slope on the left and right side of the peak do not match.

The background on the left side of the peak is fit with a linear function as well as the right side, $f_l(x) = m_1 x + b_1$ and $f_r(x) = m_2 x + b_2$. A symmetric range around the centroid of the peak is chosen such that the fit spans $[\mu - a \,,\, \mu + a]$.

$$c_1(x) = (2a - x)/2a$$

$$c_2(x) = x/2a$$

$$N = c_1(x)^3 + c_2(x)^3$$

$$\mathrm{BG}(x) = (f_l(x)c_1(x)^3 + f_r(x)c_2(x)^3)/N$$

This creates a smooth tanh-like background and can generalize for cases where $f_l \neq f_r$. The cubic exponents in the background function can be changed to different values to assess the systematic uncertainties in the centroid and area of the peak. In this work systematic uncertainties introduced by the treatment of the background were much smaller than other sources of uncertainty when used to fit high-statistics peaks.

5.1.2 Doppler Broadening Systematic Uncertainties

In order to extract accurate information from the Doppler broadening of each peak it is important to first quantify how well we know the inputs and how sensitive the simulation will be to slight changes in each quantity.

The stopping power, which is determined by SRIM, is expected to be accurate to within 10% [59]. The uncertainty in the stopping power is directly related to the uncertainty in the lifetime and will have a greater systematic effect when the lifetime of the excited state is not well known or unknown.

The exponentially modified gaussian response function is well known for all ^{19}Ne γ ray energies. The σ parameter in the response function has <0.7% uncertainty for each detector below 1600 keV, however, this uncertainty is larger in the case of the 4.03 MeV γ ray which lies far away from many of the β-delayed γ rays used to model σ.

The final two inputs of the Doppler broadening simulation, ^{19}Ne excited state lifetimes and the feeding intensities and energies from ^{20}Na excited states, have large literature uncertainties, and in some cases, are unknown. The absolute ^{20}Mg$(\beta p)^{19}$Ne* feeding intensities are obtained from the direct proton measurements of Piechaczek *et al.* and Lund *et al.* [42, 44] and used when available. The uncertainty in the better known quantity between the lifetime and proton feeding energy is used to determine a systematic uncertainty in measurements of the lesser known quantity, or will be considered a free parameter for χ^2 minimization if there are no prior measurements. In the subsequent subsections this is delineated for each case.

The systematic uncertainties determined from these quantities are combined in quadrature with statistical uncertainties.

In all fits described below, we are able to achieve a minimum in the χ^2_ν distribution close to 1, using an isotropic distribution of γ-rays with respect to proton distribution indicating that we are not sensitive to angular correlations.

5.2 Results and Discussion

The decay scheme presented in Figure 5.6 is deduced from the γ ray spectrum obtained in this experiment. Only the ^{19}Ne levels which are populated by ^{20}Mg(βp) are displayed. The measured ^{20}Mg(βp) intensities and γ ray energies are reported in Table 5.1. The γ ray intensities per ^{20}Mg β decay ($I_{\beta p \gamma}$) are determined from the integral of each fit. These values are corrected for the SeGA efficiency and normalized to the number of ^{20}Mg β decays.

We proceed to discuss the individual ^{19}Ne states.
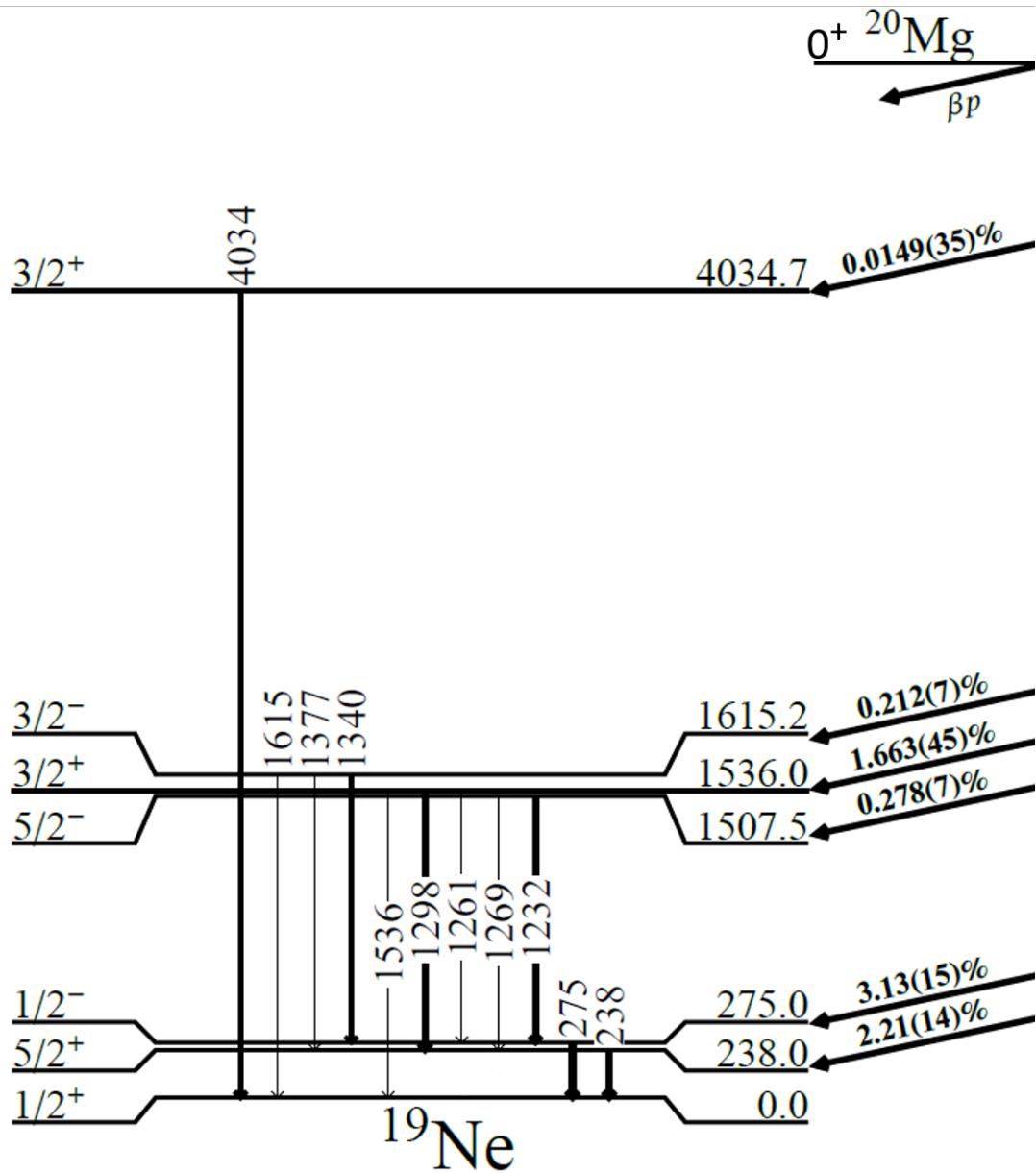
Figure 5.6: ^{19}Ne level scheme from ^{20}Mg$(\beta p\gamma)^{19}$Ne decay deduced from the present work. The γ ray transition intensities are denoted by the thicknesses of the arrows, which are proportional to their intensities. The ^{20}Mg(βp) feeding intensities are denoted by the arrows on the right.

Table 5.1: Column one reports the ^{19}Ne excited-state energies populated by ^{20}Mg(βp), and were determined by applying recoil corrections to the measured γ ray energies in the lab-frame (column-four). Column two reports the measured lifetimes of ^{19}Ne excited states. Column three reports the intensity of ^{20}Mg(βp) feedings to each excited state, where each feeding is determined by adding all γ ray decays originating from each state and subtracting feeding from higher lying states. Column four reports the measured lab frame energies of each γ ray branch. Column five reports the total intensity of each γ-ray transition per ^{20}Mg decay. Column six reports the γ ray branching ratios for each ^{19}Ne excited-state. Column seven reports the measured CoM proton energies feeding ^{19}Ne excited states.

$E_x(^{19}\text{Ne})$ (keV)	τ (ps)	$I_{^{20}\text{Mg}(\beta p)}$	E_γ (keV)	$I_{\beta p \gamma}$	Branch (%)	E_{CoM} (MeV)
238.04(10)		0.0221(14)	238.04(10)	$(3.80 \pm 0.07_{stat} \pm 0.08_{sys}) \times 10^{-2}$	100	
274.96(10)		0.0313(15)	274.96(10)	$(3.59 \pm 0.06_{stat} \pm 0.08_{sys}) \times 10^{-2}$	100	
1507.52(25)	$4.3^{+1.3}_{-1.1}$	0.00278(7)	1232.49(22)	$(2.36 \pm 0.04_{stat} \pm 0.05_{sys}) \times 10^{-3}$	84.9(4)	
			1269.47(24)	$(4.18 \pm 0.12_{stat} \pm 0.09_{sys}) \times 10^{-4}$	15.1(4)	
1535.95(24)		0.01663(45)	1260.87(24)	$(6.75 \pm 0.15_{stat} \pm 0.15_{sys}) \times 10^{-4}$	4.05(16)	
			1297.94(22)	$(1.539 \pm 0.027_{stat} \pm 0.033_{sys}) \times 10^{-2}$	92.53(35)	
			1535.90(24)	$(5.68 \pm 0.44_{stat} \pm 0.17_{sys}) \times 10^{-4}$	3.42(29)	
1615.24(30)		0.00212(7)	1340.27(25)	$(1.57 \pm 0.03_{stat} \pm 0.03_{sys}) \times 10^{-3}$	74.0(17)	2.70(23)
			1377.1(3)[a]	$(1.82 \pm 0.41_{stat} \pm 0.04_{sys}) \times 10^{-4}$	8.6(18)	
			1615.16(30)[b]	$(3.68 \pm 0.18_{stat} \pm 0.08_{sys}) \times 10^{-4}$	17.4(9)	
4034.7(16)		0.000149(35)	4034.2(16)	$(1.19 \pm 0.12_{stat} \pm 0.12_{sys}) \times 10^{-4}$	80(15)[c]	$1.21^{+0.25}_{-0.22}$

[a] Value derived from 238, 275, and 1340 keV γ ray peak energies
[b] Value derived from addition of 275 and 1340 keV γ ray peak energies
[c] Value adopted from [17]

5.2.1 ^{19}Ne 1507 keV $5/2^-$ state

There are two γ rays which are emitted from this state at 1232.5 keV and 1269.3 keV and they are expected to have branching ratios of 88(3)% and 12(3)% respectively [74]. The 1507 keV excited state lifetime has been previously measured to be $1.4^{+0.5}_{-0.6}$ ps [75], 1.7(3) ps [19], and $4.1^{+3.5}_{-1.4}$ ps [74]. Since there is significant tension between the various lifetime measurements, the lifetime was treated as a free paramater for χ^2 minimization.

It is important to note that there is very little broadening in the 1232 keV peak due to a long lifetime and therefore any ^{20}Na states assumed to feed this ^{19}Ne level yield almost exactly the same peak shape. Therefore, even though the feedings in Lund and Piechaczek differ substantially, they will both fit the data equally well. The lack of sensitivity to the proton branches adopted makes it relatively simple to measure the lifetime of the state. The χ^2 is minimized by taking a value of the lifetime long enough that nearly all the recoiling ^{19}Ne ions in this state are stopped before emitting a gamma ray (Fig. 5.7). By minimizing the χ^2 as a function of the lifetime, a value of $4.3^{+1.3}_{-1.1}$ ps is measured for the lifetime of the 1507 keV state (Fig. 5.8). The uncertainty is determined from the χ^2 minimization as well as a systematic uncertainty associated with the σ parameter and stopping power. This measurement is in agreement with [74] and more precise, but does not agree within 1 standard deviation with the measurements in [75] or [19].

The peak at 1269.3 keV is fit using the lifetime of 4.3 ps, determined by the 1232.5 keV peak, since the former peak had much higher statistics. This peak sits next to a Doppler broadened peak from the 1536 keV state of ^{19}Ne that will be addressed in the next section.

The γ ray intensities per ^{20}Mg β decay of the 1232 keV and 1269 keV γ rays are shown in Table 5.1. We can use these intensities to determine a γ-decay branching ratio from the 1507
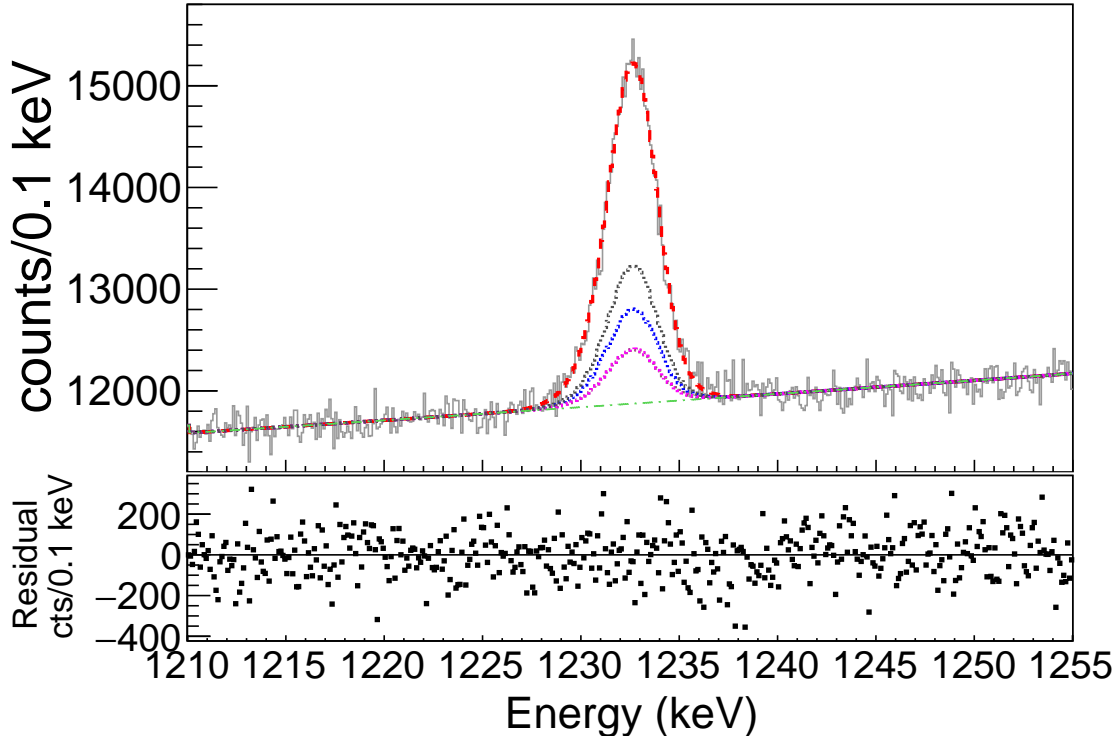
Figure 5.7: (color online) Upper panel: The fit of the 1232 keV γ ray peak is produced by using 4.3 ps lifetime as well as proton feeding intensities from Piechaczek *et al.* [42]. The solid gray line represents the data, the dot-dashed green line denotes the background, the dotted lines denote the different contributions of each proton feeding, and the dashed red line denotes the total fit. The fit has a χ^2_ν=1.07. Lower panel: The Residual plot shows the data subtracted from the fit function.
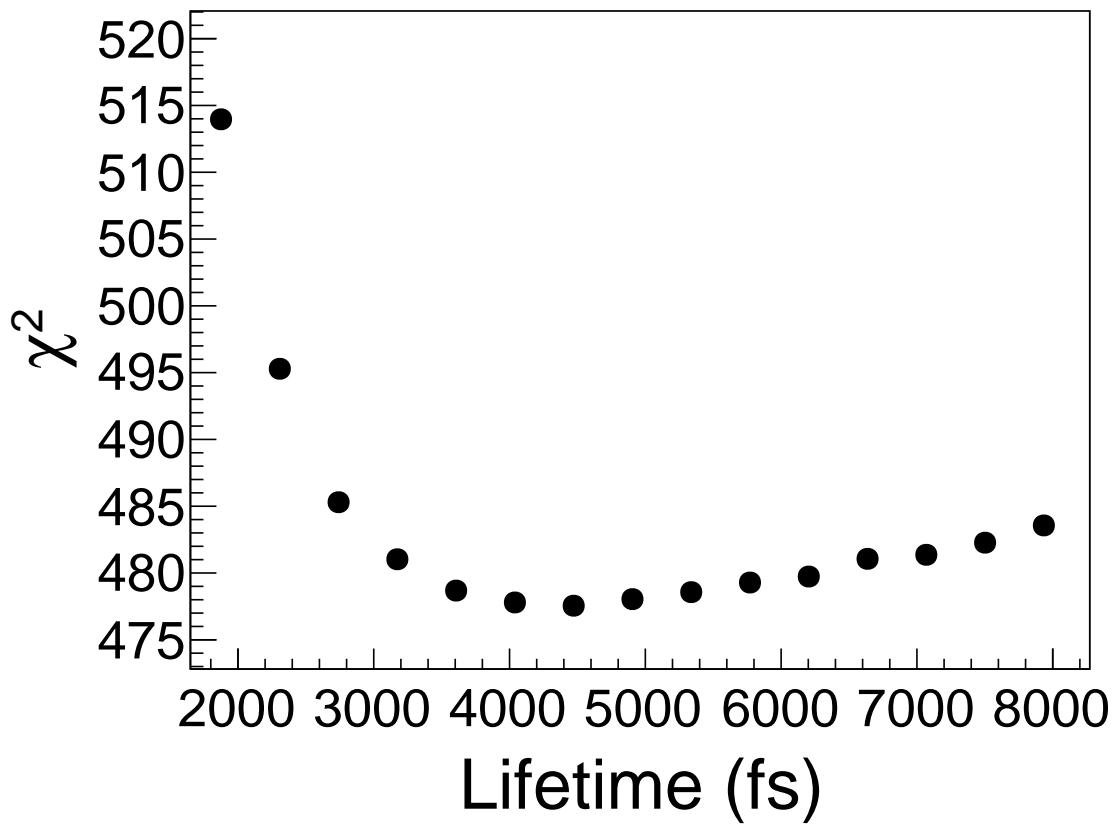
Figure 5.8: χ^2 values determined by simulating the lifetime of the 1507 keV ^{19}Ne state for many values and comparing the simulation to the data over 447 degrees of freedom. The minimum is found at 4.3 ps.
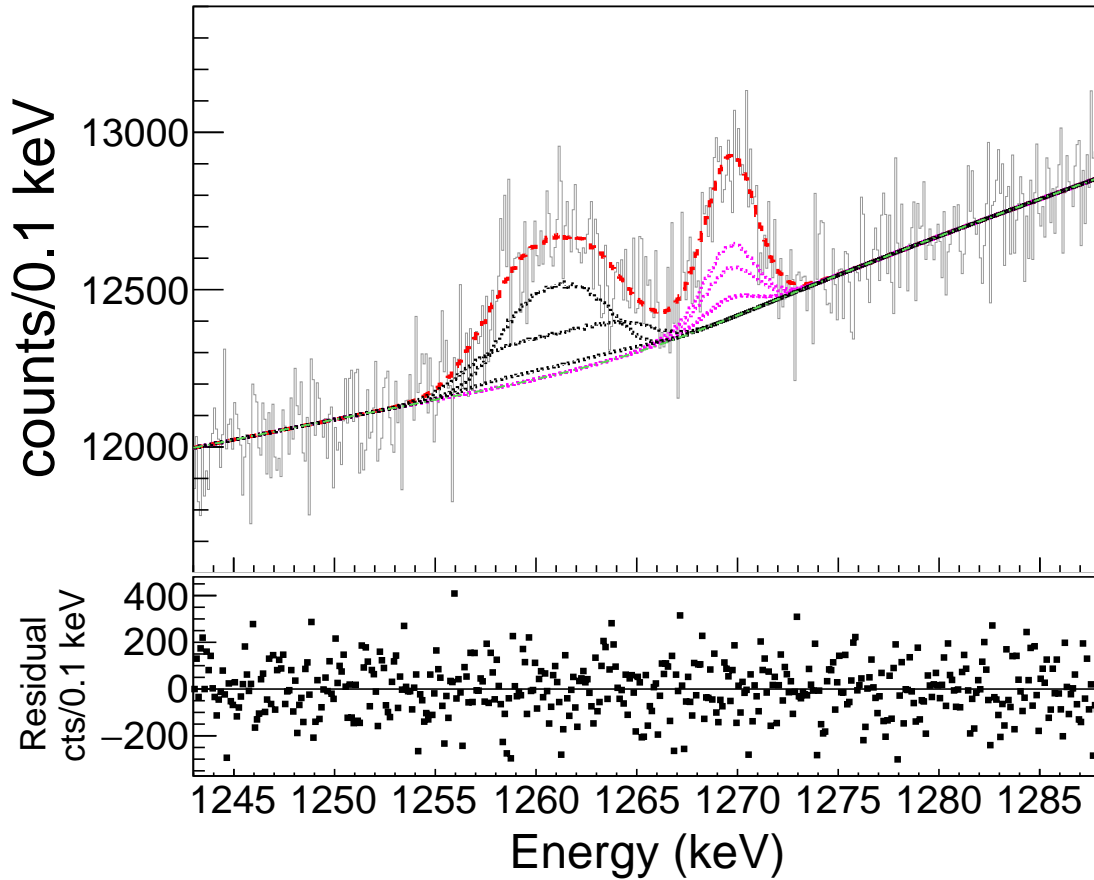
Figure 5.9: (color online) Upper panel: The γ ray spectrum above contains two ^{20}Mg(βpγ) peaks from different excited states in ^{19}Ne. The data are represented by the solid black line and, the dot-dashed green line denotes the background, the dotted pink lines denote the different contributions of proton feedings to the 1507 keV state, the dotted black lines denote the different contributions of proton feedings to the 1536 keV state, and the dashed red line denotes the total fit which has a $\chi^2_\nu = 1.11$. Lower panel: The Residual plot shows the data subtracted from the fit function.

Table 5.2: Piechaczek [42] and Lund [44] absolute % proton feeding intensities to 1536 keV state per ^{20}Mg β-decay. The quoted relative uncertainty for all intensities measured by Piechaczek is 12%.

Piechaczek		Lund	
$E_x(^{20}\text{Na})$ MeV	$I_{\beta p}$	$E_x(^{20}\text{Na})$ MeV	$I_{\beta p}$
4.7-5.2	0.7		
		5.604(5)	0.03(4)
6.266(30)	0.1	6.273(7)	0.33(9)
6.521(30)	0.51	6.496(3)	0.47(7)
$\approx$6.92	0.02		
$\approx$7.44	0.01		

keV state. The uncertainties in efficiency cancel out and we are only concerned with the statistical uncertainty for calculating the branching ratio, which is measured to be 84.9(4)% decay to the 275 keV state and 15.1(4)% decay to the 238 keV state, in agreement with previous measurement [74].

The total β-delayed proton feeding of the 1507 keV state $I_{\beta p-1507} = 2.78(7) \times 10^{-3}$ is consistent with the value from Piechaczek *et al.* of $I_{\beta p-1507} = 2.5(3) \times 10^{-3}$ and more precise but is a factor of 2.7 lower than the value measured by Lund *et al.* $I_{\beta p-1507} = 7.4(21) \times 10^{-3}$, which has a large uncertainty.

5.2.2 ^{19}Ne 1536 keV state

There are two γ rays which have been measured from this state at 1261 keV and 1298 keV and are expected to have branching ratios of 5(3)% and 95(3)% respectively [74]. In this work we measure an additional branch decaying to the ground state at 1536 keV for the first time. The lifetime of the state has a recently measured value of 16(4) fs [19] and is in agreement with the previous evaluation of 28(11) fs [17] so a value of 16 fs is adopted for the simulation. Clear broadening is apparent for all three of the γ rays emitted and the

different proton energies and intensities that feed the 1536 keV state become much more important. For the simulation of each recoil energy, the relatively precise values of $E_x(^{20}\text{Na})$ from Lund *et al.* were adopted. The relative branches from both Piechaczek and Lund were used to separately fit the data and the total number of counts in the peak was left as a free parameter.

It is easy to see that the relative branches from Lund do not fit the 1298 keV peak accurately with a $\chi_\nu^2 = 30.8$ (Fig. 5.10). An additional lower-energy proton feeding is required to fit the data. The relative branches from Piechaczek fit the data much better and return a $\chi_\nu^2 = 1.14$. From the fit of the 1298 keV peak a value of $I_{\beta p\gamma-1298} = (1.54 \pm 0.03_{stat} \pm 0.03_{sys}) \times 10^{-2}$ is measured.

A fit of the 1261 keV peak is shown in Fig. 5.9. The simulation for this peak used the relative proton feedings from Piechaczek as well as the 16 fs lifetime of the state, which fit the 1298 keV peak well. The feeding of the 1261 keV peak is measured to be $I_{\beta p\gamma-1261} = (6.75 \pm 0.15_{stat} \pm 0.15_{sys}) \times 10^{-4}$.

The 1536 keV state has three γ decay paths to the ground state of ^{19}Ne. The two cascades that do not directly decay to the ground state will yield a small portion of counts in the 1536 keV peak due to summing in a single γ ray detector. The number of counts in the 1536 keV peak due to the summing effect is calculated from the number of counts in the 1298 keV peak and SeGA efficiency for a 238 keV γ ray as well as the number of counts in the 1261 keV peak and SeGA efficiency for a 275 keV γ ray. After subtracting the summing counts from the 1536 keV peak integral we measure an intensity of $I_{\beta p\gamma-1536} = (5.68 \pm 0.44_{stat} \pm 0.17_{sys}) \times 10^{-4}$.

From $I_{\beta p\gamma-1261}$, $I_{\beta p\gamma-1298}$, and the newly measured $I_{\beta p\gamma-1536}$ we measure the γ ray branching ratio from the ^{19}Ne 1536 keV state to be a 4.05(16)% branch to the 275 keV
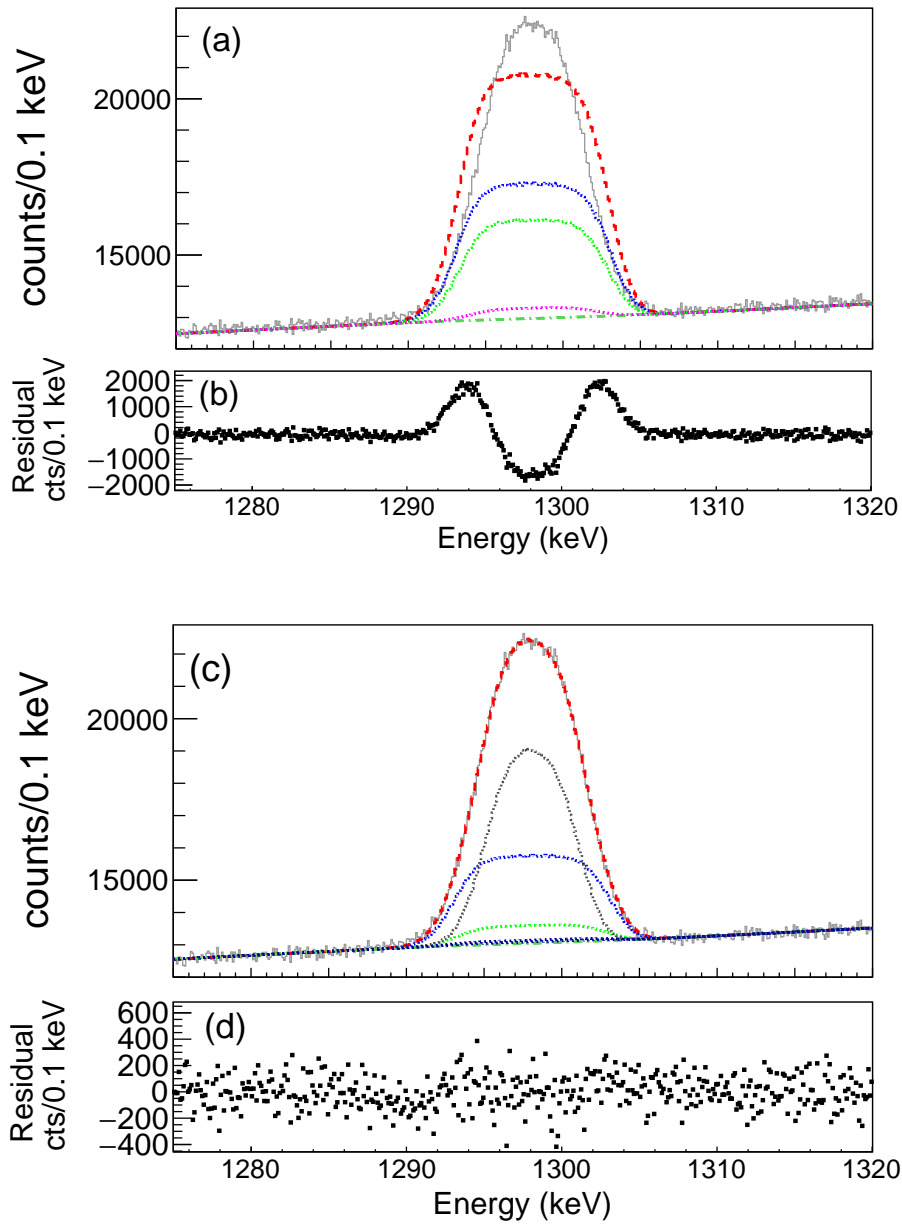
Figure 5.10: (color online) Fits of the 1298 keV γ ray peak above are produced using a 16 fs lifetime. (a) The fit is produced using the relative proton feeding intensities, measured by Lund [44], from Table 5.2. The data are represented by the solid gray line, the dot-dashed green line denotes the background, the dotted lines denote the different contributions of each proton feeding, and the dashed red line denotes the best total fit. (b) The Residual plot shows the data subtracted from the fit function in (a). (c) The fit is produced using the relative proton feeding intensities, measured by Piechaczek [42], from Table 5.2. Similarly to panel (a) the data are represented by the solid line, the dot-dashed line denotes the background, the dotted lines denote the different contributions of each proton feeding, and the dashed line denotes the best total fit. (d) The Residual plot shows the data subtracted from the fit function in (c).

state, a 92.53(35)% branch to the 238 keV state, and a 3.42(29)% branch to the ground state.

5.2.3 ^{19}Ne 1615 keV state

There are three γ rays which are emitted from this state with energies of 1340, 1377, and 1615 keV and they are expected to have branching ratios of 70(4)%, 10(3)%, and 20(3)% respectively [74]. This state has never been observed in ^{20}Mg β-decay before the present work, so there is no available proton feeding data. It is possible that multiple ^{20}Na states contribute to the feeding, however, the simplest procedure is to begin by assuming one proton energy to fit the peak and this CoM energy will be considered a free parameter. A lifetime of 143(31) fs was determined in a data evaluation [17] by combining measurements from [74, 76], however a more recent value of 80(15) fs was reported in Ref. [19] so we have re-evaluated the lifetime to be 93(20) fs by taking a weighted average with inflated uncertainty.

Using the adopted lifetime of 93(20) fs and interpolated σ parameter to simulate the broadening of the 1340 keV peak, a CoM energy of 2.7 MeV minimizes the χ^2 (Fig. 5.11). From the χ^2 distribution we get an uncertainty in the CoM energy of 100 keV. An additional systematic uncertainty in the CoM energy of 200 keV from the uncertainty in the lifetime as well as an uncertainty of 50 keV for the uncertainty in the σ parameter yields a value of 2.70(23) MeV for the CoM energy. From this we determine an excitation energy $E_x(^{20}$Na$)=$ 6.51(23) MeV for the proton-emitting state. This is consistent with proton emission from the ^{20}Na isobaric analog state at 6498.4(5) keV [56].

The 1377 and 1615 keV lines both have low statistics and do not provide significant information about the energies of protons feeding the state. We apply the peak shape corresponding to the proton energies that best fit the higher statistics 1340 keV peak to

these two peaks to determine the total intensity of protons feeding the 1615 keV state.

For a fit of the 1377 keV peak a simple linear background was used for this relatively low statistics case and a broad peak was fit on top of it. In the case of the 1615 keV peak a linear plus exponential function was used to model the background since the peak sits on the tail of a very high statistics 1634 keV peak from ^{20}Na$(\beta\gamma)$ decay.

Since the 1615 keV state also has two cascades that do not directly decay to the ground state, a small portion of counts in the 1615 keV peak are due to summing in a single γ ray detector and must be subtracted. The number of counts in the 1615 keV peak due to this effect is calculated from the number of counts in the 1340 keV peak and SeGA efficiency for a 275 keV γ ray as well as the number of counts in the 1377 keV peak and SeGA efficiency for a 238 keV γ ray.

The γ ray intensities per ^{20}Mg β decay of the 1340, 1377, and 1615 keV γ rays are shown in Table 5.1. A measurement of the branching ratios from the 1615 keV state using the intensities yields a 74.0(17)% branch to the 275 keV state, a 8.6(18)% branch to the 238 keV state, and a 17.4(9)% branch to the ground state of ^{19}Ne, in agreement with and more precise than previous measurement [74].

5.2.4 ^{19}Ne 4.03 MeV state

There are three γ rays which are emitted from this state at 2497, 3758, and 4034 keV and they are expected to have branching ratios of 15(5)%, 5(5)%, and 80(15)% respectively [17]. In the present experiment, only the 4.03 MeV γ ray is detected above background. For this case all 16 detectors are used to determine the feeding of the 4.03 MeV state and the shape of the Doppler broadened feature in order to reduce the statistical uncertainty.

The lifetime of the 4.03 MeV state has been measured to be 13^{+16}_{-9} fs [19], 11^{+4}_{-3} fs [18],
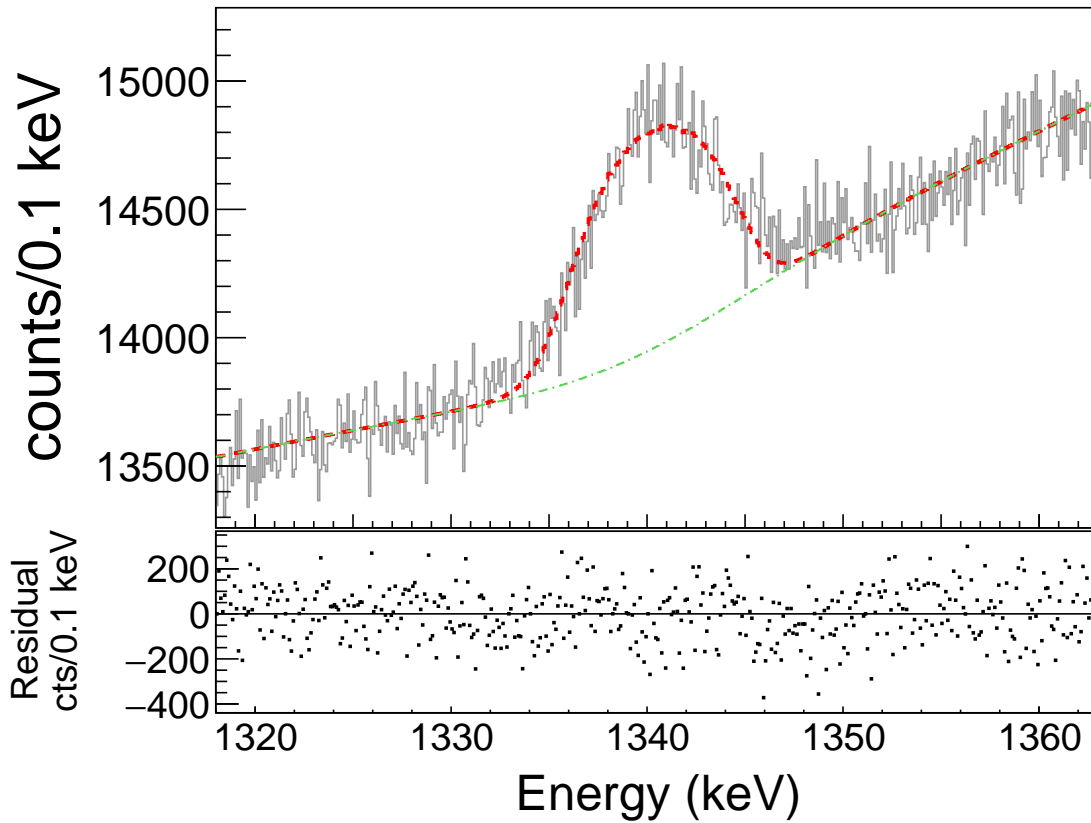
Figure 5.11: (color online) Upper panel: The fit of the 1340 keV γ ray peak is produced by using a 93 fs lifetime and a CoM energy of 2.7 MeV between the proton and recoiling ^{19}Ne. The solid gray line represents the data, the dot-dashed green line denotes the background and the dashed red line denotes the background+simulated peak. The fit has a χ^2_ν=1.00. Lower panel: The Residual plot shows the data subtracted from the fit function.
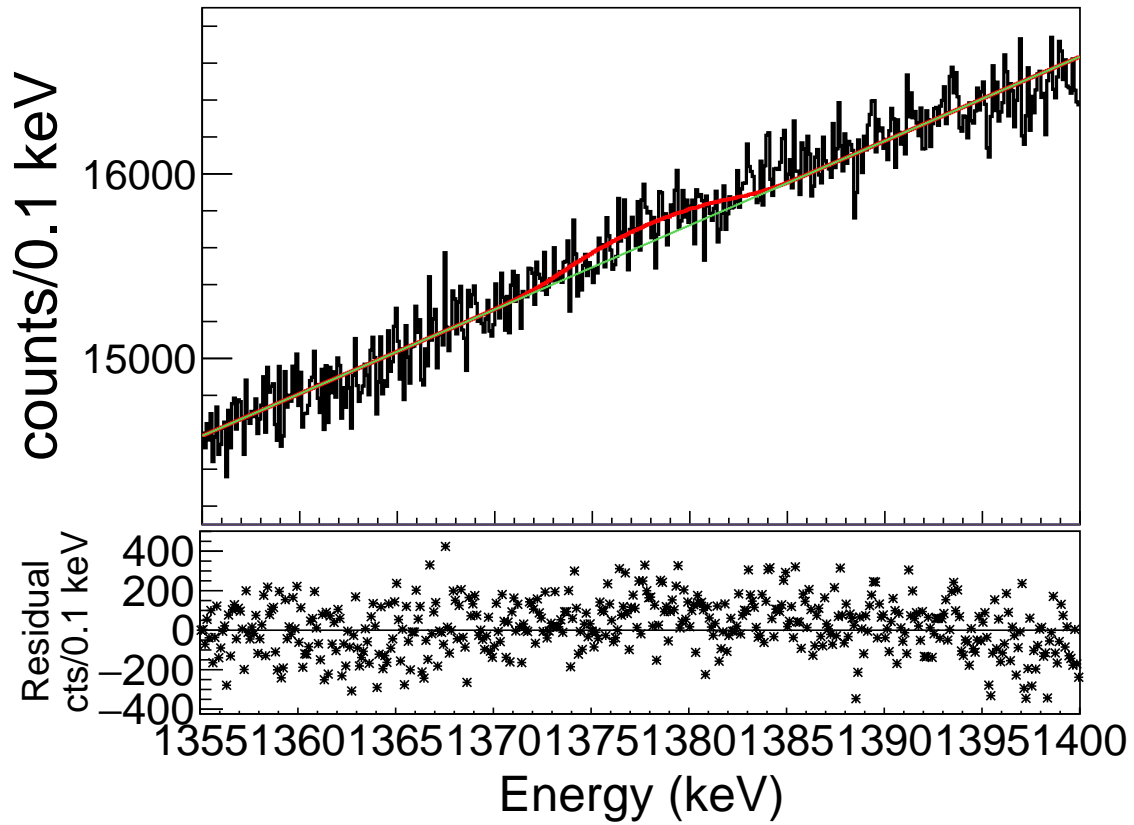
Figure 5.12: The fit of the 1377 keV γ ray peak is produced by using a 93 fs lifetime and a CoM energy of 2.7 MeV between the proton and recoiling ^{19}Ne. The black line represents the data, the green line denotes the linear background and the red line denotes the background+simulated peak. Lower panel: The Residual plot shows the data subtracted from the background.
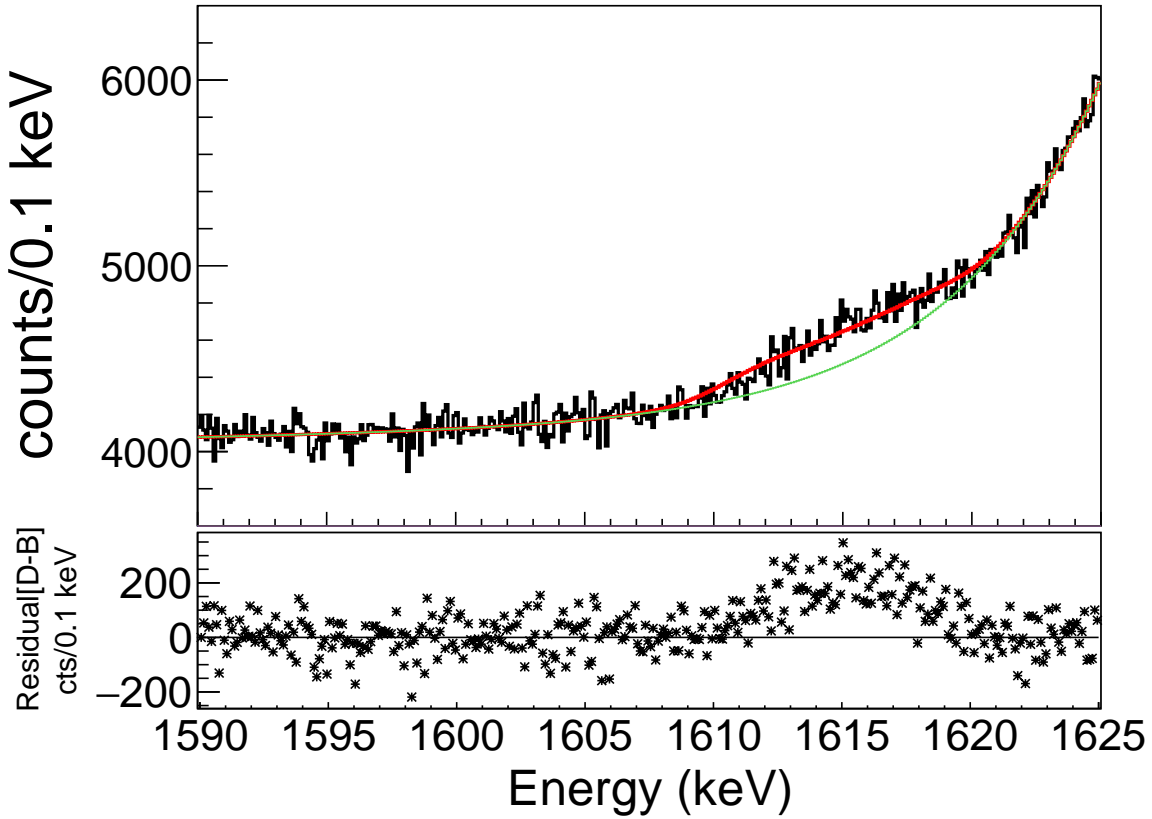
Figure 5.13: The fit of the 1616 keV γ ray peak is produced by using a 93 fs lifetime and a CoM energy of 2.7 MeV between the proton and recoiling ^{19}Ne. The black line represents the data, the green line denotes the exponential background and the red line denotes the background+simulated peak. Lower panel: The Residual plot shows the data subtracted from the background.
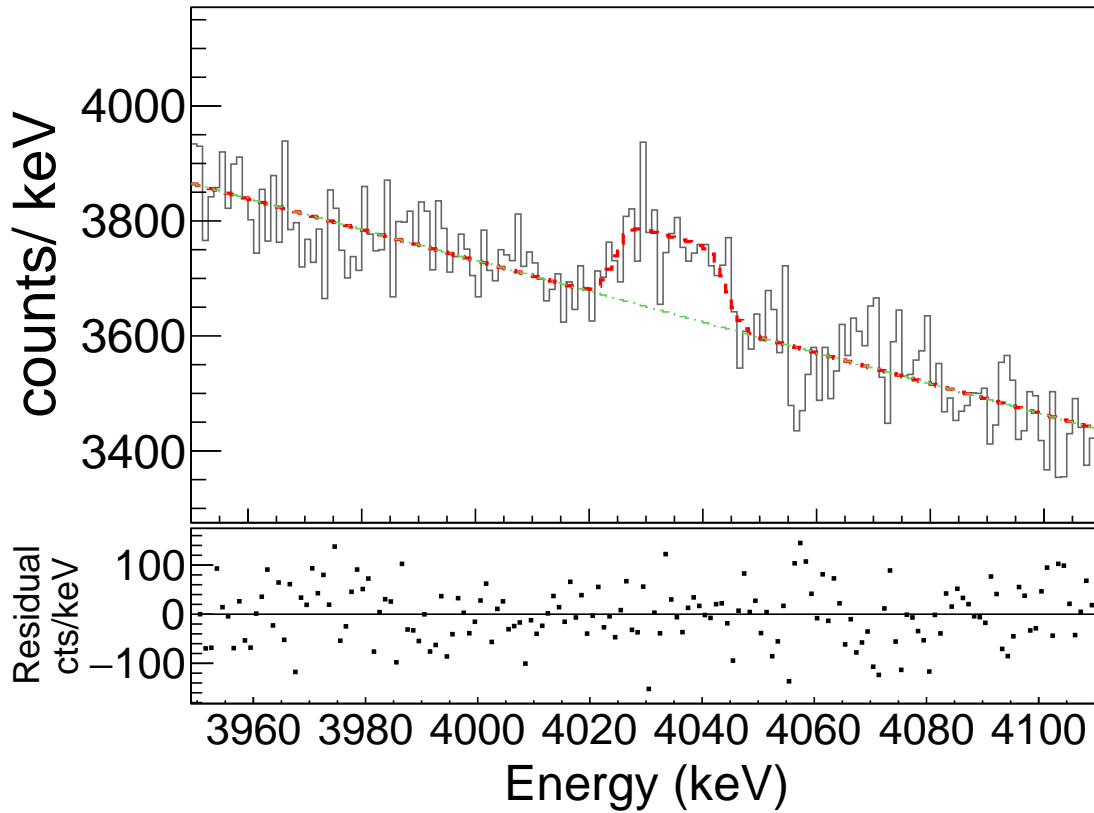
Figure 5.14: (color online) Upper panel: The fit of the 4.03 MeV peak is produced by simulating the broadened peak with an 7 fs lifetime and CoM energy of 1.21 MeV and has a $\chi^2_\nu = 0.94$. All 16 SeGA detectors are used to produce this spectrum. The solid gray line represents the data, the dot-dashed green line denotes a fit of the background and the dashed red line denotes the total fit using the optimal 1.21 MeV CoM energy. A simplified linear background model was applied for this relatively low statistics case. Lower panel: The Residual plot shows the data subtracted from the fit function.

and 6.9±1.7 fs [20]. The most precise lifetime of 6.9 fs was adopted and the uncertainty is used to determine a systematic uncertainty in the CoM energy which was left as a free parameter. In this case, where the statistics are relatively low, a simple linear model was used for the background. Additionally, an assumption is made that only one ^{20}Na excited state feeds the 4.03 MeV level (Fig. 5.14).

Minimizing the χ^2 as a function of CoM energy (Fig. 5.15) yields a CoM energy of $1.21^{+0.25}_{-0.22}$ MeV. An additional 0.025 MeV is incorporated into this uncertainty from the shift in minimum χ^2 introduced by moving the lifetime to the limits of uncertainty. This corresponds to a feeding from an excited state in ^{20}Na at 7.44 $^{+0.25}_{-0.22}$ MeV, consistent with the 7.44(10) MeV state observed to be populated in ^{20}Mg β-decay by its proton emission to lower lying ^{19}Ne states [42].

From this fit the intensity is measured to be $I_{\beta p \gamma - 4034} = (1.19 \pm 0.12_{stat} \pm 0.12_{sys}) \times 10^{-4}$. The γ branch from the 4.03 MeV state is expected to be 80(15)% [17]. Therefore, $I_{\beta p - 4034}$ $= (1.49 \pm 0.15_{stat} \pm 0.32_{sys}) \times 10^{-4}$. This value is consistent with the one reported in our initial publication [30] but slightly different because the fitting procedure is different and a different literature intensity was adopted for the 984-keV ^{20}Na line for normalization.

5.2.5 ^{19}Ne 238 and 275 keV states

Both of these lower lying ^{19}Ne states have long lifetimes, and the corresponding ^{19}Ne atoms are completely stopped in the scintillator before emitting γ rays. Therefore, we do not gain any information from Doppler broadening analysis. However, the direct feeding of the 238 and 275 keV states from ^{20}Mg(βp) decay can be determined by measuring the intensity of the γ decays and subtracting the feeding contribution to each of these states from γ decays of higher lying states in ^{19}Ne. Both of these states are fed by the 1507, 1536, 1615 and
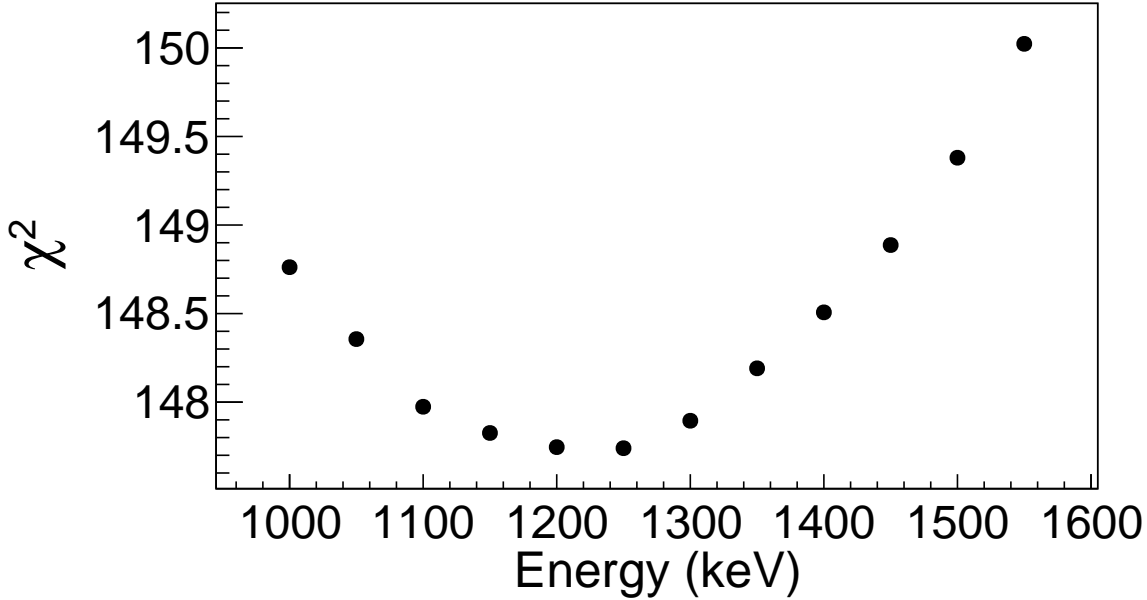
Figure 5.15: Each χ^2 value is determined by simulating a different CoM proton energy feeding the 4.03 MeV excited state in ^{19}Ne and comparing each simulation to the peak at 4034 keV. χ^2 values are determined from fits with 157 degrees of freedom. The minimum determines the most likely CoM energy.

4034 keV states and these contributions are subtracted to obtain the intensities reported in Table 5.1. These values are consistent with the previously measured values of $I_{\beta p-238} = (2.29\pm0.27)\times10^{-2}$ and $I_{\beta p-275} = (3.12\pm0.37)\times10^{-2}$ [42] and $I_{\beta p-238} = (2.23\pm0.34)\times10^{-2}$ and $I_{\beta p-275} = (3.69\pm0.52)\times10^{-2}$ [44] and more precise.

5.3 Conclusion

We have measured the ^{20}Mg$(\beta p)^{19}$Ne feedings and γ ray branches of 6 excited states in ^{19}Ne. We have developed a Monte Carlo simulation to analyze 9 Doppler broadened ^{19}Ne peaks. We have measured the energy of the proton transition which feeds the astrophysically important 4.03 MeV state, facilitating future measurements of the α-branch from this state.

Additionally we have measured the energy of the proton transition which feeds the 1615 keV state as well as the lifetime of the 1507 keV state and found a new γ decay branch from the 1536 keV state.

This is the first time Doppler broadening analysis has been applied to such high statistics β-delayed proton-γ peaks, enabling a substantial improvement in sensitivity over [29]. We have shown this method can be a useful tool to measure excited state lifetimes, proton branches, and proton energies and can distinguish between conflicting decay schemes. The method is therefore complementary to direct measurements of β-delayed protons and should prove to be even more useful when applied to β-delayed neutron emission.

Chapter 6

Outlook

6.1 The ^{15}O$(\alpha, \gamma)^{19}$Ne Reaction

Experiment E14066 has ultimately provided a road-map for future experiments to utilize ^{20}Mg β-decay in the search for α-emission from the 4.03 MeV state in ^{19}Ne. This alternative method to transfer reactions, which have thus far only provided upper limits of Γ_α, has the potential to provide a finite value for the α-branch.

Both particles in the $p - \alpha$ emission following ^{20}Mg β-decay have well-measured center of mass energies. The center of mass energy of the proton, measured in this work, is $1.21^{+0.25}_{-0.22}$ MeV and the α particle CoM energy has been measured at 505.8 ± 1.0 keV [17, 24, 19], providing a unique signal for charged particle detectors to search for. A detector system, such as GADGET [77], devoted to measuring low energy charged particles, may be an ideal setup for measuring this unique signal.

6.2 Doppler Broadening in β-delayed particle emission

The Doppler Broadening line shape analysis has been incredibly useful in determining many unknown quantities in β-delayed $p\gamma$ emission. With the high statistics in our experiment we have been able to determine branching ratios, excited state lifetimes, proton energies and can differentiate between competing decay schemes. While this method has been useful

on the proton-rich side, it may be even more useful to implement in β-delayed neutron emission. The detection of neutrons is generally much more difficult and relies on a kinematic interaction to directly detect the particle whereas it is much easier to detect charged particles directly. Since information about the neutron is preserved in β-delayed particle emission, where excited state lifetimes are short, Doppler Broadening line shape analysis may be an alternative to directly measuring these particles.

BIBLIOGRAPHY

BIBLIOGRAPHY

[1] Klaus Hentschel. Atomic models, j.j. thomson's "plum pudding" model. In *Compendium of Quantum Physics*, pages 18–21. Springer Berlin Heidelberg, 2009.

[2] E. Rutherford. The scattering of alpha and beta particles by matter and the structure of the atom. *Philosophical Magazine*, 21:669–688, 1911.

[3] J. Chadwick. Possible existence of a neutron. *Nature*, 129:312, 1932.

[4] Alejandro Sonzogni. NNDC chart of nuclides. In *ND2007*. EDP Sciences, 2007.

[5] E. Margaret Burbidge, G. R. Burbidge, William A. Fowler, and F. Hoyle. Synthesis of the elements in stars. *Rev. Mod. Phys.*, 29(4):547–650, October 1957.

[6] Kenneth S Krane. *Introductory nuclear physics, 3rd Edition*. Wiley, New York, NY, 1988.

[7] B. Alex Brown and W. A. Richter. New "USD" hamiltonians for thesdshell. *Physical Review C*, 74(3), September 2006.

[8] Ray Mackintosh, Jim Al-Khalili, Bjrn Jonson, and Teresa Pea. *Nucleus: A Trip into the Heart of Matter*. The Johns Hopkins University Press, 2001.

[9] W. Heisenberg. Nuclear forces. *Zeitschr. f. Phys.*, 77(1), 1932.

[10] P. W. Merrill. NATIONAL ACADEMY OF SCIENCES: Abstracts of papers presented at the annual meeting april 28-30, 1952, washington, d. c. *Science*, 115(2992):479–489, May 1952.

[11] C. Iliadis. *Nuclear Physics of Stars, 3rd Edition*. John Wiley and Sons, New York, NY, 2015.

[12] Robert D. Gehrz, James W. Truran, Robert E. Williams, and Sumner Starrfield. Nucleosynthesis in classical novae and its contribution to the interstellar medium. *Publications of the Astronomical Society of the Pacific*, 110(743):3–26, January 1998.

[13] H. Schatz and K.E. Rehm. X-ray binaries. *Nucl. Phys. A*, 777:601–622, oct 2006.

[14] Walter H. G. Lewin, Jan Van Paradijs, and Ronald E. Taam. X-ray bursts. *Space Sci. Rev.*, 62(3-4):223–389, sep 1993.

[15] R. K. Wallace and S. E. Woosley. Explosive hydrogen burning. *Astrophys. J. Suppl. Ser.*, 45:389, feb 1981.

[16] R. H. Cyburt, A. M. Amthor, A. Heger, E. Johnson, L. Keek, Z. Meisel, H. Schatz, and K. Smith. DEPENDENCE OF x-RAY BURST MODELS ON Nucl. REACTION RATES. *Astrophys. J.*, 830(2):55–x, oct 2016.

[17] D.R. Tilley, H.R. Weller, C.M. Cheves, and R.M. Chasteler. Energy levels of light nuclei a = 18-19. *Nucl. Phys. A*, 595(1):1–170, dec 1995.

[18] R. Kanungo, T. K. Alexander, A. N. Andreyev, G. C. Ball, R. S. Chakrawarthy, M. Chicoine, R. Churchman, B. Davids, J. S. Forster, S. Gujrathi, G. Hackman, D. Howell, J. R. Leslie, A. C. Morton, S. Mythili, C. J. Pearson, J. J. Ressler, C. Ruiz, H. Savajols, M. A. Schumaker, I. Tanihata, P. Walden, and S. Yen. Lifetime of19ne(4.03 MeV). *Phys. Rev. C*, 74(4):045803, oct 2006.

[19] W. P. Tan, J. Görres, J. Daly, M. Couder, A. Couture, H. Y. Lee, E. Stech, E. Strandberg, C. Ugalde, and M. Wiescher. Lifetime of the astrophysically important 4.03-MeV state inNe19. *Phys. Rev. C*, 72(4):041302, oct 2005.

[20] S. Mythili, B. Davids, T. K. Alexander, G. C. Ball, M. Chicoine, R. S. Chakrawarthy, R. Churchman, J. S. Forster, S. Gujrathi, G. Hackman, D. Howell, R. Kanungo, J. R. Leslie, E. Padilla, C. J. Pearson, C. Ruiz, G. Ruprecht, M. A. Schumaker, I. Tanihata, C. Vockenhuber, P. Walden, and S. Yen. Lifetimes of states inNe19above theO15αbreakup threshold. *Phys. Rev. C*, 77(3):035803, mar 2008.

[21] B. Davids, A. M. van den Berg, P. Dendooven, F. Fleurot, M. Hunyadi, M. A. de Huu, R. H. Siemssen, H. W. Wilschut, H. J. Wörtche, M. Hernanz, J. José, K. E. Rehm, A. H. Wuosmaa, and R. E. Segel. Astrophysical rate of15o(α, γ)19nevia the(p, t)reaction in inverse kinematics. *Phys. Rev. C*, 67(6):065808, jun 2003.

[22] K. E. Rehm, A. H. Wuosmaa, C. L. Jiang, J. Caggiano, J. P. Greene, A. Heinz, D. Henderson, R. V. F. Janssens, E. F. Moore, G. Mukherjee, R. C. Pardo, T. Pennington, J. P. Schiffer, R. H. Siemssen, M. Paul, L. Jisonna, and R. E. Segel. Branching ratio$\gamma\alpha/\gamma\gamma$of the 4.033 MeV3/2state in19ne. *Phys. Rev. C*, 67(6):065809, jun 2003.

[23] W. P. Tan, J. L. Fisker, J. Görres, M. Couder, and M. Wiescher. O15(α, γ)ne19breakout reaction and impact on x-ray bursts. *Phys. Rev. Lett.*, 98(24):242503, jun 2007.

[24] Barry Davids, Richard H. Cyburt, Jordi José, and Subramanian Mythili. THE INFLU-ENCE OF UNCERTAINTIES IN THE15o(α, γ)19ne REACTION RATE ON MODELS OF TYPE i x-RAY BURSTS. *Astrophys. J.*, 735(1):40, jun 2011.

[25] P.V. Magnus, M.S. Smith, A.J. Howard, P.D. Parker, and A.E. Champagne. Measure-ment of 15o(,)19ne resonance strengths. *Nuclear Physics A*, 506(2):332–345, January 1990.

[26] A. M. Laird, S. Cherubini, A. N. Ostrowski, M. Aliotta, T. Davinson, A. Di Pietro, P. Figuera, W. Galster, J. S. Graulich, D. Groombridge, J. Hinnefeld, M. Lattuada, P. Leleux, L. Michel, A. Musumarra, A. Ninane, M. G. Pellegriti, A. C. Shotter, Spi-taleri, A. Tumino, J. Vervier, and P. Woods. Indirect study of the astrophysically important15o(,)19nereaction through2h(18ne, 19ne)1h. *Physical Review C*, 66(4), Oc-tober 2002.

[27] D. W. Visser, J. A. Caggiano, R. Lewis, W. B. Handler, A. Parikh, and P. D. Parker. Particle decay branching ratios for states of astrophysical importance inNe19. *Physical Review C*, 69(4), April 2004.

[28] H.O.U. Fynbo, M.J.G. Borge, J. Cederkäll, S. Courtin, P. Dessagne, B. Jonson, G. Le Scornet, T. Nilsson, G. Nyman, E. Poirier, K. Riisager, O. Tengblad, and K. Wilhelmsen. New information on the β-decay of 11li from doppler broadened γ lines. *Nucl. Phys. A*, 736(1-2):39–54, may 2004.

[29] S. B. Schwartz, C. Wrede, M. B. Bennett, S. N. Liddick, D. Pérez-Loureiro, A. Bowe, A. A. Chen, K. A. Chipps, N. Cooper, D. Irvine, E. McNeice, F. Montes, F. Naqvi, R. Ortez, S. D. Pain, J. Pereira, C. Prokop, J. Quaglia, S. J. Quinn, J. Sakstrup, M. Santia, S. Shanab, A. Simon, A. Spyrou, and E. Thiagalingam. Observation of doppler broadening inβ-delayed proton-γdecay. *Phys. Rev. C*, 92(3):031302, sep 2015.

[30] C. Wrede, B. E. Glassman, D. Pérez-Loureiro, J. M. Allen, D. W. Bardayan, M. B. Bennett, B. A. Brown, K. A. Chipps, M. Febbraro, C. Fry, M. R. Hall, O. Hall, S. N. Liddick, P. O'Malley, W. J. Ong, S. D. Pain, S. B. Schwartz, P. Shidling, H. Sims, P. Thompson, and H. Zhang. New portal to the o15(α, γ)ne19 resonance triggering CNO-cycle breakout. *Phys. Rev. C*, 96(3):032801(R), sep 2017.

[31] G. Audi, F. G. Kondev, Meng Wang, W.J. Huang, and S. Naimi. The NUBASE2016 evaluation of nuclear properties. *Chi. Phys. C*, 41(3):030001, March 2017.

[32] C. Wrede, J. A. Clark, C. M. Deibel, T. Faestermann, R. Hertenberger, A. Parikh, H.-F. Wirth, S. Bishop, A. A. Chen, K. Eppinger, A. García, R. Krücken, O. Lepyoshkina, G. Rugel, and K. Setoodehnia. Toward preciseQECvalues for the superallowed0→0decays ofT=2nuclides: The masses ofNa20, al24, p28, andCl32. *Phys. Rev. C*, 81(5):055503, May 2010.

[33] B. A. Brown, A. E. Champagne, H. T. Fortune, and R. Sherr. Nature of theNa202646-keV level and the stellar reaction rate forNe19(p,)20na. *Phys. Rev. C*, 48(3):1456–1459, September 1993.

[34] D.R. Tilley, C.M. Cheves, J.H. Kelley, S. Raman, and H.R. Weller. Energy levels of light nuclei, a = 20. *Nucl. Phys. A*, 636(3):249–364, June 1998.

[35] J.P. Wallace, P.J. Woods, G. Lotay, A. Alharbi, A. Banu, H.M. David, T. Davinson, M. McCleskey, B.T. Roeder, E. Simmons, A. Spiridon, L. Trache, and R.E. Tribble. breakout reaction in x-ray bursts. *Phys. Lett. B*, 712(1-2):59–62, May 2012.

[36] S. Kubono, N. Ikeda, M. Yasue, T. Nomura, Y. Fuchi, H. Kawashima, S. Kato, H. Orihara, T. Shinozuka, H. Ohnuma, H. Miyatake, and T. Shimoda. TheP 19nes- wave resonant state in20na at stellar energies. *Zeit. Phys. A*, 331(3):359–360, September 1988.

[37] L.O. Lamm, C.P. Browne, J. Görres, S.M. Graff, M. Wiescher, A.A. Rollefson, and B.A. Brown. The level structure of 20na and the impact upon the stellar reaction rate for 19ne(p,)20na. *Nucl. Phys. A*, 510(3):503–517, April 1990.

[38] M.S. Smith, P.V. Magnus, K.I. Hahn, A.J. Howard, P.D. Parker, A.E. Champagne, and Z.Q. Mao. A high-resolution study of the 20ne(3he, t)20na reaction and the 19ne(p,)20na reaction rate. *Nucl. Phys. A*, 536(2):333–348, January 1992.

[39] B. D. Anderson, B. Wetmore, A. R. Baldwin, L. A. C. Garcia, D. M. Manley, R. Madey, J. W. Watson, W. M. Zhang, B. A. Brown, C. C. Foster, and Y. Wang. Excitation of the 2.65 MeV state in theNe20(p, n)20na reaction at 135 MeV. *Phys. Rev. C*, 52(4):2210–2215, October 1995.

[40] J. Belarge, S. A. Kuvin, L. T. Baby, J. Baker, I. Wiedenhöver, P. Höflich, A. Volya, J. C. Blackmon, C. M. Deibel, H. E. Gardiner, J. Lai, L. E. Linhardt, K. T. Macon, E. Need, B. C. Rasco, N. Quails, K. Colbert, D. L. Gay, and N. Keeley. Experimental investigation of the ne19(p,)20na reaction rate and implications for breakout from the hot CNO cycle. *Phys. Rev. Lett.*, 117(18):182701, October 2016.

[41] J. Görres, M. Wiescher, K. Scheller, D. J. Morrissey, B. M. Sherrill, D. Bazin, and J. A. Winger. -delayed proton decay ofMg20and its astrophysical implications. *Phys. Rev. C*, 46(3):R833–R837, September 1992.

[42] A. Piechaczek, M.F. Mohar, R. Anne, V. Borrel, B.A. Brown, J.M. Corre, D. Guillemaud-Mueller, R. Hue, H. Keller, S. Kubono, V. Kunze, M. Lewitowicz, P. Magnus, A.C. Mueller, T. Nakamura, M. Pfützner, E. Roeckl, K. Rykaczewski, M.G. Saint-Laurent, W.-D. Schmidt-Ott, and O. Sorlin. Beta-decay of 20mg. *Nucl. Phys. A*, 584(3):509–531, feb 1995.

[43] L. J. Sun, X. X. Xu, D. Q. Fang, C. J. Lin, J. S. Wang, Z. H. Li, Y. T. Wang, J. Li, L. Yang, N. R. Ma, K. Wang, H. L. Zang, H. W. Wang, C. Li, C. Z. Shi, M. W. Nie, X. F. Li, H. Li, J. B. Ma, P. Ma, S. L. Jin, M. R. Huang, Z. Bai, J. G. Wang, F. Yang, H. M. Jia, H. Q. Zhang, Z. H. Liu, P. F. Bao, D. X. Wang, Y. Y. Yang, Y. J. Zhou, W. H. Ma, J. Chen, Y. G. Ma, Y. H. Zhang, X. H. Zhou, H. S. Xu, G. Q. Xiao, and W. L. Zhan. β -decay study of the tz=-2 proton-rich nucleus mg20. *Phys. Rev. C*, 95(1):014314, jan 2017.

[44] M. V. Lund, , A. Andreyev, M. J. G. Borge, J. Cederkäll, H. De Witte, L. M. Fraile, H. O. U. Fynbo, P. T. Greenlees, L. J. Harkness-Brennan, A. M. Howard, M. Huyse, B. Jonson, D. S. Judson, O. S. Kirsebom, J. Konki, J. Kurcewicz, I. Lazarus, R. Lica, S. Lindberg, M. Madurga, N. Marginean, R. Marginean, I. Marroquin, C. Mihai, M. Munch, E. Nacher, A. Negret, T. Nilsson, R. D. Page, S. Pascu, A. Perea, V. Pucknell, P. Rahkila, E. Rapisarda, K. Riisager, F. Rotaru, C. Sotty, M. Stanoiu, O. Tengblad, A. Turturica, P. Van Duppen, V. Vedia, R. Wadsworth, and N. Warr. Beta-delayed proton emission from 20mg. *Eur. Phys. J. A*, 52(10):304, October 2016.

[45] G. Vancraeynest, P. Decrock, M. Gaelens, M. Huyse, P. Van Duppen, C. R. Bain, T. Davinson, R. D. Page, A. C. Shotter, P. J. Woods, F. Binon, P. Duhamel, J. Vanhorenbeeck, R. Coszach, Th. Delbar, W. Galster, J. S. Graulich, P. Leleux, E. Liénard, P. Lipnik, C. Michotte, A. Ninane, J. Vervier, H. Herndl, H. Oberhummer, Cs. Sükösd, and M. Wiescher. 19ne(p,)20naand19ne(d, n)20nareactions and its astrophysical implications for the transition of the hot CNO cycle to therpprocess. *Phys. Rev. C*, 57(5):2711–2723, May 1998.

[46] M. Couder, C. Angulo, E. Casarejos, P. Demaret, P. Leleux, and F. Vanderbist. New direct study of theNe19(p,)na20reaction cross section. *Phys. Rev. C*, 69(2):022801(R), February 2004.

[47] R. Wilkinson, G. Lotay, A. Lennarz, C. Ruiz, G. Christian, C. Akers, W. N. Catford, A. A. Chen, D. Connolly, B. Davids, D. A. Hutcheon, D. Jedrejcic, A. M. Laird, L. Martin, E. McNeice, J. Riley, and M. Williams. Direct measurement of the key ec.m.=456 keV

resonance in the astrophysical ne19(p,)na20 reaction and its relevance for explosive binary systems. *Physical Review Letters*, 119(24), December 2017.

[48] Glenn F Knoll. *Radiation Detection and Measurement; 3rd ed.* Wiley, New York, NY, 2000.

[49] M. Febbraro. Private Communication, 2015. MCNP Simulation.

[50] X-5 Monte Carlo Team. LA-UR-03-1987, 2003. MCNP - Version 5, Vol. I: Overview and Theory.

[51] C.J. Prokop, S.N. Liddick, B.L. Abromeit, A.T. Chemey, N.R. Larson, S. Suchyta, and J.R. Tompkins. Digital data acquisition system implementation at the national superconducting cyclotron laboratory. *Nucl. Instrum. Methods in Phys. Res., Sect. A*, 741:163–168, mar 2014.

[52] D. Seweryniak, P.J. Woods, B. Blank, M.P. Carpenter, T. Davinson, S.J. Freeman, J. Görres, A. Heinz, R.V.F. Janssens, H. Mahmud, T.L. Khoo, Z. Liu, G. Mukherjee, E. Rehm, F. Sarazin, J. Shergur, M. Shawcross, S. Sinha, and A. Woehr. Complete structure determination of the astrophysically important nucleus 20na below the proton threshold. *Phys. Lett. B*, 590(3-4):170–175, June 2004.

[53] J. P. Wallace and P. J. Woods. Level structure above the proton threshold of20na. *Phys. Rev. C*, 86(6):068801, December 2012.

[54] Jun Chen. Nuclear data sheets for a=40. *Nucl. Data Sheets*, 140:1–376, February 2017.

[55] M.J. Martin. Nuclear data sheets for a = 208. *Nucl. Data Sheets*, 108(8):1583–1806, August 2007.

[56] B. E. Glassman, D. Pérez-Loureiro, C. Wrede, J. Allen, D. W. Bardayan, M. B. Bennett, B. A. Brown, K. A. Chipps, M. Febbraro, C. Fry, M. R. Hall, O. Hall, S. N. Liddick, P. O'Malley, W. Ong, S. D. Pain, S. B. Schwartz, P. Shidling, H. Sims, P. Thompson, and H. Zhang. Revalidation of the isobaric multiplet mass equation for theA=20quintet. *Phys. Rev. C*, 92(4):042501, oct 2015.

[57] J. Allison, K. Amako, J. Apostolakis, P. Arce, M. Asai, T. Aso, E. Bagli, A. Bagulya, S. Banerjee, G. Barrand, B.R. Beck, A.G. Bogdanov, D. Brandt, J.M.C. Brown, H. Burkhardt, Ph. Canal, D. Cano-Ott, S. Chauvie, K. Cho, G.A.P. Cirrone, G. Cooperman, M.A. Cortés-Giraldo, G. Cosmo, G. Cuttone, G. Depaola, L. Desorgher, X. Dong, A. Dotti, V.D. Elvira, G. Folger, Z. Francis, A. Galoyan, L. Garnier, M. Gayer,

K.L. Genser, V.M. Grichine, S. Guatelli, P. Guèye, P. Gumplinger, A.S. Howard, I. Hřivnáčová, S. Hwang, S. Incerti, A. Ivanchenko, V.N. Ivanchenko, F.W. Jones, S.Y. Jun, P. Kaitaniemi, N. Karakatsanis, M. Karamitros, M. Kelsey, A. Kimura, T. Koi, H. Kurashige, A. Lechner, S.B. Lee, F. Longo, M. Maire, D. Mancusi, A. Mantero, E. Mendoza, B. Morgan, K. Murakami, T. Nikitina, L. Pandola, P. Paprocki, J. Perl, I. Petrović, M.G. Pia, W. Pokorski, J.M. Quesada, M. Raine, M.A. Reis, A. Ribon, A. Ristić Fira, F. Romano, G. Russo, G. Santin, T. Sasaki, D. Sawkey, J.I. Shin, I.I. Strakovsky, A. Taborda, S. Tanaka, B. Tomé, T. Toshito, H.N. Tran, P.R. Truscott, L. Urban, V. Uzhinsky, J.M. Verbeke, M. Verderi, B.L. Wendt, H. Wenzel, D.H. Wright, D.M. Wright, T. Yamashita, J. Yarba, and H. Yoshida. Recent developments in geant4. *Nuclear Instruments and Methods in Physics Research Section A: Accelerators, Spectrometers, Detectors and Associated Equipment*, 835:186–225, November 2016.

[58] D. Pérez-Loureiro, C. Wrede, M. B. Bennett, S. N. Liddick, A. Bowe, B. A. Brown, A. A. Chen, K. A. Chipps, N. Cooper, D. Irvine, E. McNeice, F. Montes, F. Naqvi, R. Ortez, S. D. Pain, J. Pereira, C. J. Prokop, J. Quaglia, S. J. Quinn, J. Sakstrup, M. Santia, S. B. Schwartz, S. Shanab, A. Simon, A. Spyrou, and E. Thiagalingam. β-delayedγdecay of$P26$: Possible evidence of a proton halo. *Phys. Rev. C*, 93(6):064320, jun 2016.

[59] James F. Ziegler, M.D. Ziegler, and J.P. Biersack. SRIM the stopping and range of ions in matter (2010). *Nucl. Instrum. Methods in Phys. Res., Sect. B*, 268(11-12):1818–1823, jun 2010.

[60] B. A. Brown. Private Communication, 2016. sd-Shell Model Calculations.

[61] H. T. Fortune and B. H. Wildenthal. Level densities in$F20$: Experimental, shell model, and weak coupling results. *Phys. Rev. C*, 30(3):1063–1065, September 1984.

[62] W. A. Richter, S. Mkhize, and B. Alex Brown. sd-shell observables for the USDA and USDB hamiltonians. *Physical Review C*, 78(6):064302, December 2008.

[63] S. R. Stroberg, H. Hergert, J. D. Holt, S. K. Bogner, and A. Schwenk. Ground and excited states of doubly open-shell nuclei fromab $initio$valence-space hamiltonians. *Phys. Rev. C*, 93(5):051301(R), May 2016.

[64] J. Simonis, S. R. Stroberg, K. Hebeler, J. D. Holt, and A. Schwenk. Saturation with chiral interactions and consequences for finite nuclei. *Phys. Rev. C*, 96(1):014303, July 2017.

[65] S. R. Stroberg. Private Communication, 2017. IMSRG Calculations.

[66] B. Alex Brown. New skyrme interaction for normal and exotic nuclei. *Phys. Rev. C*, 58(1):220–231, July 1998.

[67] S. Kubono, N. Ikeda, Y. Funatsu, M. H. Tanaka, T. Nomura, H. Orihara, S. Kato, M. Ohura, T. Kubo, N. Inabe, A. Yoshida, T. Ichihara, M. Ishihara, I. Tanihata, H. Okuno, T. Nakamura, S. Shimoura, H. Toyokawa, C. C. Yun, H. Ohnuma, K. Asahi, A. Chakrabarti, T. Mukhopadhyay, and T. Kajino. Decay property ofNa20for the onset mechanism of the rapid-proton process. *Phys. Rev. C*, 46(1):361–365, July 1992.

[68] E. K. Warburton. Second-forbidden unique decays ofBe10, na22, andAl26. *Phys. Rev. C*, 45(1):463–466, January 1992.

[69] O.B. Tarasov and D. Bazin. Lise++: Exotic beam production with fragment separators and their design. *Nuclear Instruments and Methods in Physics Research Section B: Beam Interactions with Materials and Atoms*, 376:185 – 187, 2016.

[70] H FYNBO. Doppler broadened γ-lines from exotic nuclei. *Nucl. Instrum. Methods B*, 207(3):275–282, jul 2003.

[71] A.J. Ferguson. Angular correlation methods. In *Pure and Applied Physics*, pages 277–306. Elsevier, 1974.

[72] L.J.B. Goldfarb and R.G. Seyler. The determination of spins of resonance states. *Phys. Lett. B*, 28(1):15–17, oct 1968.

[73] J. R. Duray, H. J. Hausman, N. L. Gearhart, J. W. D. Sinclair, and W. S. Steiner. Spectroscopy ofAl25by means of the ReactionMg24(p, p1ɩ)mg24. *Phys. Rev. C*, 6(3):792–800, sep 1972.

[74] R.D. Gill, K. Bharuth-Ram, K.P. Jackson, R.A.I. Bell, B.C. Robertson, J. L'Ecuyer, N.G. Chapman, and H.J. Rose. Electromagnetic transitions in 19ne. *Nucl. Phys. A*, 152(2):369–386, aug 1970.

[75] Takahisa Itahashi, Tokushi Shibata, and Tetsuo Wakatsuki. Lifetime measurements of the excited states in19ne and23mg. *JPSJ*, 31(4):961–966, oct 1971.

[76] C. Lebrun, F. Guilbault, P. Avignon, and Y. Deschamps. Mean lifetimes of levels inNe19. *Phys. Rev. C*, 15(3):1174–1177, mar 1977.

[77] M. Friedman, D. Pérez-Loureiro, T. Budner, E. Pollacco, C. Wrede, M. Cortesi, C. Fry, B. Glassman, M. Harris, J. Heideman, M. Janasik, B.T. Roeder, M. Roosa, A. Saastamoinen, J. Stomps, J. Surbrook, P. Tiwari, and J. Yurkon. GADGET: a gaseous detector

with germanium tagging. *Nuclear Instruments and Methods in Physics Research Section A: Accelerators, Spectrometers, Detectors and Associated Equipment*, 940:93–102, October 2019.